Chemical Science

ROYAL SOCIETY OF CHEMISTRY

REVIEW

View Article Online
View Journal

Check for updates

Cite this: DOI: 10.1039/d6sc03328h

Received 21st April 2026
Accepted 4th June 2026

DOI: 10.1039/d6sc03328h

rsc.li/chemical-science

Modulation strategies for acidic oxygen evolution catalysts

Feifei Teng, Zhenlu Wang * and Jingqi Guan *

Proton exchange membrane water electrolysis (PEMWE) is a highly efficient, eco-friendly hydrogen generation technology. With advantages such as fast response and superior energy efficiency, it is a crucial pathway for the clean energy transition. However, the anodic oxygen evolution reaction (OER) suffers from sluggish kinetics. Moreover, the acidic environment leads to insufficient stability of most catalysts, restricting the efficiency and lifespan of PEMWE. Thus, the design of acidic OER catalysts that combine high activity with long-term durability remains a key bottleneck for its large-scale application. This paper systematically elucidates the basic reaction mechanism of acidic OER, reviews the research progress of catalysts based on noble metals and those based on non-noble metals, and analyzes performance enhancement strategies from electronic and geometric structural perspectives. Furthermore, it discusses the application performance in high current density electrolytic devices, analyzes the main technical bottlenecks in the industrialization process, and proposes future development directions for this field.

1. Introduction

During the critical period of global energy transition, developing green and eco-friendly energy to substitute traditional fossil fuels has emerged as a common goal.[1–3] Traditional carbon-based fuels are not only limited in reserves but also emit large amounts of greenhouse gases and pollutants during combustion, exacerbating climate change and environmental pollution.[4–7] Although renewable energy sources such as wind and solar power have been widely used, their inherent intermittency and instability limit their continuous power supply capabilities. In this context, hydrogen energy has gained significant traction as a promising energy carrier, primarily owing to its high energy density and inherently green, clean characteristics.[8–10] Among them, water electrolysis technology for hydrogen production can convert intermittent electrical energy into storable hydrogen, building an important bridge between renewable energy and stable energy supply.[11,12]

Proton exchange membrane water electrolysis (PEMWE) is particularly notable among the various water electrolysis methods, owing to its distinct advantages. Compared with traditional alkaline water electrolysis technology, PEMWE offers distinct advantages including a compact system structure, high operating current density, and high hydrogen purity.[13–16] This technology is built upon two key electrochemical processes: the oxygen evolution reaction (OER) at the anode and the hydrogen evolution reaction (HER) at the cathode.[17,18] Yet the OER involves a four-electron transfer process, resulting in sluggish reaction kinetics and a significantly higher overpotential compared to the HER, which only requires two-electron transfer.[19–21] More importantly, the strongly acidic conditions during OER detrimentally impact catalyst robustness, readily causing the dissolution of active components and structural reconstruction, which seriously affects operational stability of the electrochemical system.[22–25]

As the hydrogen energy industry advances towards large-scale development, the stable operation of PEMWE technology at high densities (exceeding 1 A cm^{-2}) is a research focus.[26] Increasing the operating current density can improve hydrogen production efficiency and reduce industrial hydrogen production costs. However, high current density conditions further exacerbate the corrosion and degradation of anode catalysts.[27,28] Therefore, developing acidic OER catalysts that combine high activity with superior stability, deeply understanding their reaction mechanisms, and revealing the inherent link between material structure and performance have become the core of breaking through the technical bottleneck of PEMWE.[29–33] This research direction not only has important academic value but also represents a strategic need for promoting renewable energy development and achieving energy structure transformation (Fig. 1).

This paper systematically reviews the research progress on acidic OER mechanisms. Based on this, it comprehensively summarizes the latest research achievements of different types of catalysts, including catalysts based on noble metals and non-noble metals, with the analysis of the key roles of electronic structure modulation and geometric structure design strategies in enhancing catalytic performance. Meanwhile, we

---

Institute of Physical Chemistry, College of Chemistry, Jilin University, 2519 Jiefang Road, Changchun 130021, P. R. China. E-mail: wzl@jlu.edu.cn; guanjq@jlu.edu.cn

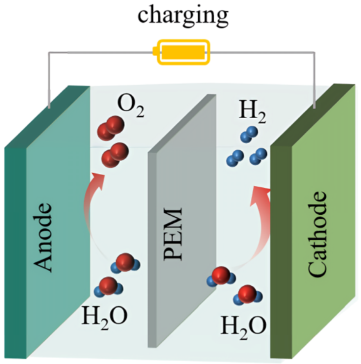

Fig. 1 Schematic diagram of water electrolysis in an acidic medium.

comprehensively review the practical application of OER catalysts in high-current-density electrolysis devices. Finally, it conducts an in-depth analysis of the main challenges currently faced in this research field, such as the trade-off between catalytic activity and structural durability, decreasing noble metal consumption, and provides forward-looking prospects for future development directions (Fig. 2).

2. OER mechanisms

The multi-electron transfer nature of OER leads to a high reaction energy barrier, and thus understanding its underlying mechanisms is a prerequisite for the design of efficient and robust catalysts.[34] Currently, adsorbate evolution mechanism (AEM, not to be confused with anion exchange membrane), lattice oxygen oxidation mechanism (LOM), and oxide pathway mechanism (OPM) are three widely considered mechanisms.[35–37] Importantly, the design and composition of the catalysts direct the reaction along different mechanistic pathways, which can have a decisive impact on their performance.[38,39] Therefore, it is crucial to study the OER mechanisms, and each of them will be described in detail below (Fig. 3).

2.1. AEM

AEM, as the earliest proposed OER mechanism, has a well-established research system. The AEM pathway proceeds through four consecutive steps, each involving the coupled transfer of an electron and a proton. First, H_2O undergoes chemisorption at the metal site (M), where the applied voltage drives dissociation to release an H^+ and an electron, concurrently forming the adsorbed M–OH intermediate. Then OH* adsorbed on the M site is oxidized to O*, while releasing a second H^+ and an electron. Then, another H_2O interacts with the reaction intermediate O*, releasing H^+ and an electron and forming OOH*. The cycle concludes as the OOH* intermediate dissociates in a concerted step, regenerating the active site and releasing O_2, H^+, and an electron.[40,41]

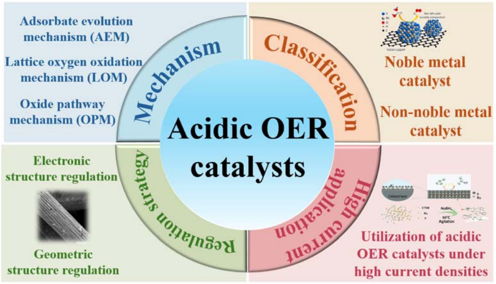

Fig. 2 Reaction mechanisms, classification, regulation strategies, and high-current-density applications of acidic oxygen evolution reaction catalysts.

Fundamentally, AEM involves the adsorption and release of intermediates on the active center. Each of the four reaction steps can affect the OER overpotential. The total Gibbs free energy change (ΔG) of the reaction, theoretically calculated to be 4.92 eV under standard conditions, is the sum of the ΔG values of the four individual steps. The ideal catalytic state is achieved only when the ΔG of each step equals 1.23 eV.[42–44] However, this ideal state is unattainable due to the scaling relation between the adsorption free energies of the intermediates OH*, O*, and OOH*.[45] Rossmeisl *et al.* demonstrated a linear proportionality between the binding energies of OOH* and OH* in OER: $\Delta G_{OOH^*} - \Delta G_{OH^*} = 3.2 \pm 0.2$ eV, which indicates a strong association between OH* and OOH*, which makes this step the rate-determining step of the reaction.[46] If $\Delta G_{OH^* \to O^*}$ decreases on the catalyst, $\Delta G_{O^* \to OOH^*}$ increases and *vice versa*. Therefore, only ΔG_{OH^*} and ΔG_{O^*} can affect the catalyst activity, and $\Delta G_{O^*} - \Delta G_{OH^*}$ is a key descriptor for the OER activity.[47] According to Sabatier's principle, the optimal catalytic performance requires the interaction strength between active sites and oxygen intermediates to fall within an appropriate range.[48] The OER activity shows a volcano type trend with $\Delta G_{O^*} - \Delta G_{OH^*}$, and the catalyst activity is highest when the binding sites of the catalyst are positioned near the summit of the volcano curve, where an overpotential of 370 mV is the theoretical minimum (25 °C, pH = 0).[49] Therefore, single-atom catalysts following the AEM pathway cannot achieve an overpotential lower than 0.37 V during the OER process.

At the experimental level, the AEM pathway can be unambiguously identified through various *in situ* spectroscopic and isotopic labeling techniques. The most definitive evidence comes from differential electrochemical mass spectrometry (DEMS) coupled with isotopic labeling. For instance, in their study on an F-doped $NiCo_2O_4$ catalytic system, Li *et al.* analyzed isotope-labeled DEMS measurements and found that the mass signal ratios of $^{32}O_2 : {}^{34}O_2 : {}^{36}O_2$ for ^{18}O-labeled $NiCo_2O_4$-F_1 and $NiCo_2O_4$ were 1804 : 27 : 1 and 3645 : 27 : 0, respectively.[50] This clearly demonstrates that both $NiCo_2O_4$ and $NiCo_2O_4$-F_1 follow the AEM for OER. The F-doping did not alter the reaction mechanism, yet it enhanced 14-fold intrinsic activity. Additionally, attenuated total reflection surface-enhanced infrared spectroscopy (ATR-SEIRAS) allows us to probe the signal intensity of reaction intermediates, thereby elucidating the underlying OER mechanism. Lu *et al.* prepared a grain boundary-rich V-doped RuO_2 catalyst using a rapid thermal-driven cation exchange strategy and collected *in situ* ATR-SEIRAS spectra at various stepped voltages.[51] As the potential increased, distinct absorption peaks at 1019, 1200, and 3300 cm^{-1} were clearly resolved in the spectra. The peak at

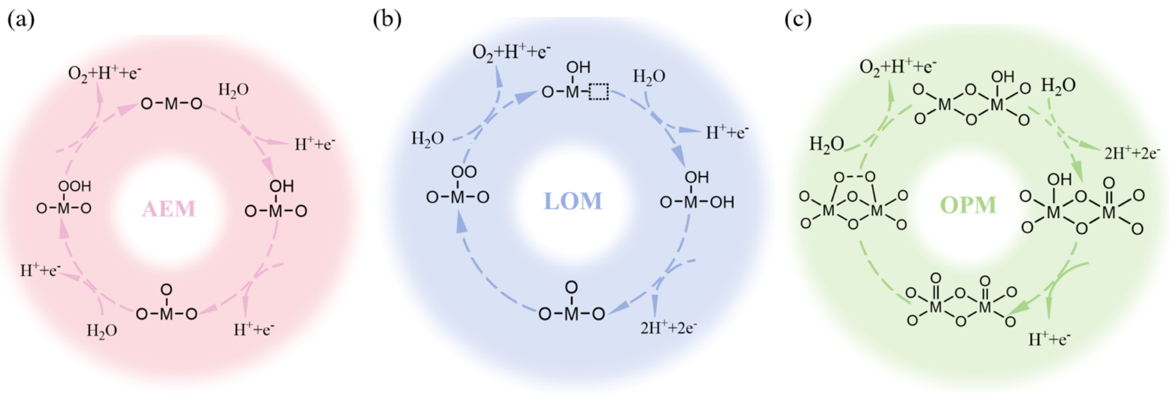

Fig. 3 Schematic of (a) AEM, (b) LOM, and (c) OPM in the acidic OER.

1200 cm^{-1} was assigned to the O–O stretching vibration of the *OOH intermediate, while the peak at 3300 cm^{-1} was attributed to the O–H stretching vibration of the *OH intermediate, providing direct *in situ* spectroscopic evidence that the reaction follows the AEM.

2.2. LOM

Traditional AEM has limitations in explaining some experimental phenomena. For example, at the reversible hydrogen electrode scale, the pH-dependent shift in OER activity onset potential for many catalysts is observed to be less than 0.37 V, contradicting the theoretical thermodynamic requirement.[52–54] Based on this, researchers proposed a new mechanism, namely LOM, which provides a novel pathway for elucidating the OER catalytic process. A key mechanistic distinction from AEM lies in the oxygen source: in the LOM pathway, the oxygen atoms in the evolved O_2 molecule originate in part or in whole from the catalyst's lattice oxygen, rather than all from the adsorbed water molecules.[55–57] This fundamental difference makes it possible for LOM to overcome the constraint posed by the adsorption-energy scaling relations inherent to AEM, so as to theoretically achieve ultra-low overpotential beyond the traditional theoretical limit.[58–60] Liu's team found that introducing F anions into the oxygen vacancies of spinel $ZnCo_2O_4$ allows the high electronegativity of F to balance residual protonation, thereby stabilizing the catalyst structure.[61] More importantly, theoretical calculations demonstrate that F incorporation shifts the O 2p center upward, activating the redox capability of lattice oxygen and subsequently triggering the LOM pathway.

In terms of the reaction path, LOM closely resembles AEM in its initial steps, both of which involve the dissociative adsorption and deprotonation of water to form O* and OH* species. However, in the subsequent reaction steps, the two show significant differences. In essence, under applied potential, the LOM pathway bypasses OOH* formation and proceeds *via* O–O coupling between adsorbed oxygen and catalyst lattice oxygen to generate O_2, which will leave oxygen vacancies in the catalyst lattice.[62–64] Meanwhile, OH$^-$ in the electrolyte will fill and repair these oxygen vacancies to complete the entire catalytic cycle. By successfully circumventing the traditional rate-determining step of OOH*, the LOM pathway can theoretically significantly reduce the overpotential of the reaction.[65,66] Extensive experimental evidence demonstrates that catalysts following the LOM pathway partially or fully usually exhibit superior OER activity to those that follow only the AEM pathway, which provides a new theoretical basis and design ideas for designing high-performance electrocatalysts. For example, Huang *et al.* achieved precise modulation of the electronic structure by doping Zr into the octahedral interstitials of Co_3O_4, which significantly enhanced the hybridization between Co and O orbitals.[67] This process not only optimizes the conventional AEM pathway, but more importantly, successfully activates the LOM pathway. Owing to the synergy between the dual reaction pathways, the prepared $Zr_xCo_{3-x}O_4$ catalyst exhibits excellent overall electrocatalytic performance in acidic media, capable of operating for 60 h when held at 100 mA cm^{-2}. This fully demonstrates that LOM significantly contributes to enhancing OER activity.

Although the LOM pathway can effectively improve the OER performance, the continuous depletion and regeneration of lattice oxygen during the reaction have a serious adverse impact on the catalytic stability. During electrochemical cycling, unrecovered oxygen vacancies ultimately trigger local structural collapse, phase transitions, or irreversible lattice reconstruction.[25,68] In addition, the lack of lattice oxygen often exposes unstable metal sites, promoting metal ion dissolution and resulting in catalyst deactivation.[69] As a result, LOM-based catalysts exhibit poorer stability in long-term operation compared to those that follow AEM.

Mu's team provided multi-dimensional experimental evidence for the LOM pathway in their study of the R-NiFeOOH@SO_4 catalytic system.[70] Using $NiMoO_4$ hydrate as a pre-catalyst, they induced abundant structural defects through Fe- and S-mediated synergistic chemical etching, which promoted the complete catalyst reconstruction during electrochemical activation. PH-dependent current density measurements revealed that the activity of R-NiFeOOH@SO_4 decayed sharply with decreasing pH, directly pointing to the participation of lattice oxygen in the OER. More importantly, *in situ* ^{18}O isotope-labeled DEMS demonstrated significantly enhanced lattice oxygen activity for this catalyst, confirming the dominant contribution of the LOM pathway to its high performance. Meanwhile, *in situ* attenuated total reflection Fourier transform infrared spectroscopy (ATR-FTIR) spectra exhibited a set of characteristic absorption peaks in the 1207–1212 cm^{-1} range, which can be assigned to the O–O coupling intermediates in the LOM pathway. These peaks are distinctly different from the characteristic peaks of the OOH* intermediate in the AEM pathway (around 1095 cm^{-1}). This disparity in spectroscopic fingerprints provides a direct vibrational spectroscopic criterion for distinguishing the two mechanisms, further corroborating the involvement of the LOM pathway.

It is crucial to emphasize, however, that despite the qualitative alignment of the aforementioned experimental evidence with the expected characteristics of the LOM pathway, this mechanism remains a subject of significant controversy in the academic community. The core debates center on three main aspects: first, the extent of lattice oxygen participation is difficult to quantify precisely. The $^{34}O_2$ signals detected in some experiments may originate from exchangeable oxygen in the catalyst's surface reconstruction layer rather than from the direct involvement of bulk lattice oxygen. This ambiguity makes the boundary between LOM and surface-reconstruction-enhanced AEM quite blurred.

Second, catalysts that strictly follow a single LOM pathway under operating conditions are extremely rare. Most highly active systems tend to exhibit a hybrid of AEM and LOM pathways to varying degrees, and the spatial heterogeneity of the catalyst surface further complicates this picture. For instance, Dai *et al.* precisely engineered high-density grain boundaries in RuO_2 *via* Ni–B co-doping.[71] Combined X-ray absorption near edge structure (XANES) and extended X-ray absorption fine structure (EXAFS) analyses revealed that the unique electronic structure at the grain boundaries preferentially activates the LOM pathway (with a 3.2-fold increase in the ^{18}O isotope exchange rate). Meanwhile, *in situ* ATR-FTIR simultaneously captured characteristic vibrational peaks of the *OOH intermediate at 1036 cm^{-1} and 1211 cm^{-1}, whereas the ordered regions away from the grain boundaries maintained the traditional AEM pathway. After selectively blocking the LOM active sites at grain boundaries using TMA^+ probes, the catalyst retained approximately 40% of its OER activity, directly confirming the spatial coexistence of grain boundary LOM and bulk AEM mechanisms on the same catalyst.

Third, the continuous consumption of lattice oxygen poses a severe threat to catalyst stability. Once the accumulation of oxygen vacancies exceeds the structural tolerance threshold of the material, it triggers irreversible cation leaching, surface amorphization, and bulk structural collapse, leading to rapid catalyst deactivation. Therefore, LOM can be viewed as a strategy that trades partial stability for a breakthrough in activity, and its long-term application in practical electrolysis devices requires extreme caution.

2.3. OPM

OPM is an innovative reaction model that has emerged in recent years to break through the inherent kinetic limitations of OER processes. The core breakthrough of this mechanism is the utilization of a specific arrangement of binuclear active sites to achieve the coupling of O*, bypassing the OOH* intermediate step required in the conventional AEM pathway.[72]

In the OPM pathway, two adjacent metal sites each adsorb an OH* and undergo deprotonation to form O*. Subsequently, the two proximate oxygen radicals recombine, liberating an oxygen molecule.[73,74] This pathway has two significant advantages. First, it breaks the linear constraint linking the OH* and OOH* adsorption energies in AEM, creating conditions for breaking through the theoretical minimum overpotential. Second, since this mechanism does not involve the participation of catalyst lattice oxygen at all, it fundamentally avoids the problems of lattice collapse and structural destabilization caused by LOM, and is expected to achieve a simultaneous improvement in both catalytic activity and long-term stability.[75] However, the conditions for triggering OPM are extremely demanding on the geometry and electronic configuration of the materials. At the geometrical level, the two metal sites must have appropriate symmetry and spacing. Too large spacing would hinder effective O*–O* coupling and return the reaction to the AEM pathway, whereas too small spacing might enhance the degree of metal–oxygen orbital hybridization and activate the LOM pathway unexpectedly.[76–78] At the electronic structure level, it is necessary to precisely regulate the degree of d–p hybridization, so that the M–O antibonding state is positioned close to the Fermi level, thereby enabling precise modulation of O* adsorption, and at the same time, to avoid the excessive oxidation of the lattice oxygen to ensure that the reaction center is kept on the metal ions.[35,79] Cui *et al.* shifted the redox center of amorphous ruthenium oxide (a-RuO_x) from O to Ru by precisely regulating the local coordination environment of amorphous ruthenium oxide, effecting a mechanistic shift from the LOM to the OPM pathway.[80] This ingenious electronic structure reconstruction strategy enables the optimized a-RuO_x catalyst to exhibit superior comprehensive performance in acidic OER. It requires only 215 mV overpotential at 10 mA cm^{-2} and maintains stability for over 300 hours (unless otherwise noted, all overpotential values mentioned in this work are measured in 0.5 M H_2SO_4 solution at a current density of 10 mA cm^{-2}), demonstrating the unique advantage of the OPM pathway in balancing catalytic activity and durability. Moreover, Li's team designed a low-ruthenium-content solid-solution oxide ($Ru_{0.32}Ta_{0.66}Mn_{0.02}O_2$).[81] In this system, the lattice expansion induced by the TaO_2 matrix effectively elongates the Ru–O bonds, thereby suppressing the LOM and significantly enhancing structural stability. Meanwhile, Mn doping optimizes the distance between dual-metal sites, which greatly increases surface *OH coverage and successfully triggers the OPM, breaking the linear scaling relationship of the AEM. Consequently, the catalyst requires an overpotential of only 175 mV for the acidic OER and demonstrates stable operation in a PEMWE at 0.5 A cm^{-2} for over 1000 hours. By introducing suitable elements into RuO_2, the OPM can be activated. For example, Liu and colleagues utilized the 4f-electron metal Gd to modulate the covalency of Ru–O bonds in RuO_2, successfully activating the dual-site OPM for acidic OER.[82] Both experimental results and theoretical calculations demonstrated that moderate Ru–O covalency stabilizes the Ru active sites and suppresses their over-oxidation. The optimized

Gd-RuO_2 catalyst requires an overpotential of only 196 mV in 0.1 M $HClO_4$ and operates stably in a PEMWE at 1 A cm^{-2} for 300 hours.

A series of *in situ* characterization techniques can demonstrate the OPM mechanism during the OER. Zhong *et al.* synthesized bifunctional IMO@p-ATO catalyst by growing IrMnO (IMO) nanoclusters on plasma-treated antimony-doped tin dioxide (p-ATO) supports *via* a hydrothermal method.[83] DEMS isotope labeling tests revealed that the dominant product in the $H_2{}^{18}O$ electrolyte was $^{36}O_2$, accompanied by only extremely weak $^{32}O_2$ and $^{34}O_2$ signals. This distribution pattern is distinctly different from the spectra of AEM and LOM pathways, indicating that the O_2 generated during the OER originates from the direct O–O coupling of water molecules *via* the OPM. In the TMA^+ probe experiment, TMA^+ is highly sensitive to the $O_2{}^{2-}$ species generated *via* the LOM pathway, yet its addition to the electrolyte resulted in no significant change in the linear sweep voltammetry (LSV) curve of IMO@p-ATO, directly ruling out the possibility of the LOM pathway. Furthermore, *in situ* ATR-SEIRAS demonstrated the emergence of a peroxo species peak at 1207 cm^{-1} (attributed to bridged side-on adsorption) at 1.30 V, which is formed through the direct coupling of surface intermediates. This stands in sharp contrast to IrO_2, which only exhibits a single *OOH peak, thereby highlighting the critical role of Mn incorporation. These two *in situ* techniques corroborate each other, definitively confirming that the OER over IMO@p-ATO follows the OPM. Yan *et al.* used RuO_2 as a model catalyst and introduced Mn atoms to construct a $Mn^{4-\delta}$–O–$Ru^{4+\delta}$ dual active site featuring local structural symmetry but asymmetric oxidation states, successfully switching the conventional AEM of RuO_2 to the OPM.[84] Using *operando* synchrotron radiation Fourier transform infrared spectroscopy (SR-FTIR), they directly captured the key O–O intermediate bridged over the bimetallic sites on $Mn_{0.2}RuO_2$ (1069 and 1113 cm^{-1}). Furthermore, *operando* DEMS with isotopic labeling detected the $^{32}O_2$ signal, providing direct experimental evidence for the OPM pathway. The resulting $Mn_{0.2}RuO_2$ catalyst exhibits outstanding activity (188 mV overpotential) and ultra-long stability (>150 h) for acidic OER.

To synergistically overcome the scaling relationship limitations of conventional AEM and the stability bottleneck of LOM, the oxygen spillover mechanism (OSM) has garnered significant attention as an emerging multi-site synergistic catalytic pathway. The essential feature of this mechanism lies in the migration of oxygen-containing intermediates from primary sites (such as metal sites) to adjacent secondary carrier or functionalized surfaces, thereby achieving spatial decoupling of the intermediate adsorption, deprotonation, and O–O coupling steps. This spillover process effectively distributes the adsorption energies of *OH and *OOH across distinct surface sites. It fundamentally weakens the linear scaling relationship between the two on a single site, making it theoretically possible to break through the 0.37 V overpotential limit. Meanwhile, since O–O bond formation no longer relies on the direct participation of lattice oxygen, OSM avoids the structural collapse and cation dissolution induced by oxygen vacancy accumulation in LOM, theoretically offering both high activity and high stability. On the experimental front, Qu *et al.* provided a typical paradigm for OSM by constructing a RuO_2/MoO_3 catalyst featuring abundant and intimate interfaces.[85] Both experimental evidence and theoretical calculations consistently demonstrated that during the acidic OER process, the active *O intermediates generated on RuO_2 can effectively spill over onto the MoO_3 carrier surface. Subsequently, the lattice oxygen of MoO_3 participates in oxygen release and the generation of oxygen vacancies, while the lattice oxygen of RuO_2 itself is preserved. This fundamentally suppresses the over-oxidation of RuO_2 and the dissolution of active sites. Benefiting from this oxygen-spillover-mediated self-protection mechanism, the RuO_2/MoO_3 catalyst exhibited a low overpotential of only 167 mV and negligible performance decay over 300 hours of operation, achieving a unification of high activity and superior stability. This work clearly indicates that the precise construction of interfacial oxygen spillover channels can effectively decouple catalytic activity from structural stability, opening a new avenue for designing durable acidic OER electrocatalysts. However, the triggering conditions for OSM are equally stringent, requiring matched orbital energy levels and appropriate interfacial spacing between the primary and secondary sites to maintain a sufficiently low spillover energy barrier. Poor interfacial charge transfer or excessive site spacing can both lead to the interruption of spillover, causing the reaction to revert to the conventional AEM pathway.

In summary, techniques such as *in situ* ATR-FTIR and isotope-labeled DEMS have enabled preliminary identification of OER mechanisms. However, experimental studies in the existing literature that can comprehensively and rigorously discriminate between reaction pathways remain extremely scarce. Future research urgently requires breakthroughs in *operando* spectroscopic techniques that combine both temporal and spatial resolution. This will allow for the precise capture of the dynamic evolution of short-lived intermediates (*e.g.*, *OOH) and transient oxygen vacancies at the real reaction interface, thereby providing direct and quantitative experimental evidence for mechanism discrimination and the rational design of catalysts.

3. Acidic OER material system

In the face of harsh acidic conditions and high-current-density requirements, noble metal-based catalysts remain the benchmark, with systems based on Ir and Ru being the primary choices, due to their excellent overall performance. Our review starts with a systematic examination of the latest advances in noble metal catalysts, followed by a brief discussion of the current development of non-noble metal catalysts.

3.1. Noble metal-based catalysts

3.1.1. Ir-based catalysts. Due to the central role of Ir in acidic OER, researchers are committed to improving its atomic utilization efficiency and catalytic performance through various methods. Among them, particular interest has been focused on Ir-based systems, notably single-atom Ir catalysts and Ir oxides, due to their unique properties. Single-atom Ir catalysts represent a promising direction for achieving efficient catalysis at low Ir loadings. Their core advantage lies in maximizing atomic economy, while enabling optimization of catalytic performance through precise tuning of the coordination environment.[86–88] By precisely designing the coordination structure around Ir, it is possible to effectively regulate its electronic density and distribution, thus altering the binding energy of reaction intermediates.[89] This provides a pathway to engineer catalyst performance and tackle the persistent bottlenecks in activity and stability.[90–92] For example, Cui *et al.* successfully achieved precise doping of 7.98 wt% Ir into a $NiCo_2O_4$ matrix *via* an ion-exchange-thermal decomposition strategy, constructing a high-performance Ir_H-$NiCo_2O_4$ catalyst.[93] Theoretical calculations revealed that Ir doping effectively tuned the binding energy landscape of key intermediates, markedly improving reaction kinetics (Fig. 4a). Therefore, this catalyst showed a 240 mV overpotential in acidic medium (Fig. 4b), and demonstrated stable operation over 282 h. It also exhibited a mass activity of 377.05 mA mg^{-1} (Fig. 4c), outperforming commercial IrO_2 in both performance and long-term durability. Peng and colleagues successfully prepared an Ir single-atom catalyst supported on Co_3O_4 (Ir_{SA}-Co_3O_4) by synchronously constructing Co defects and anchoring Ir single atoms during the precursor pyrolysis process.[94] The atomically dispersed Ir atoms were stabilized at octahedral Co defect sites, forming a unique configuration of single atoms confined within the spinel lattice. Benefiting from the electronic coupling effect of the Ir–O–Co oxygen bridge, the electronic structure of the Ir sites was optimized. This not only achieved moderate adsorption of reaction intermediates but also effectively suppressed the dissolution of active sites. Experimental results demonstrated that Ir_{SA}-Co_3O_4 exhibited an overpotential of only 199 mV (Fig. 4f) and operated stably in a PEMWE device for 150 hours at 200 mA cm^{-2} (Fig. 4g). Kumar *et al.* prepared short-range ordered Ir single-atom-ensembles on the surface of manganese-substituted spinel Co_3O_4 (Ir_{SAE}-CMO).[95] This catalyst exhibits exceptional mass activity and significantly enhanced durability, far outperforming commercial IrO_2 and conventional Ir single-atom catalysts supported on pristine Co_3O_4. First-principles calculations revealed that, compared with pristine Co_3O_4, manganese substitution in the octahedral sites of Co_3O_4 substantially lowers the migration energy barrier of Ir single atoms on the CMO surface. This facilitates the migration of iridium atoms during pyrolysis, thereby leading to the formation of strongly interacting Ir_{SAE}.

Ir-based oxides enable comprehensively enhance the catalytic performance. Through fine tuning of the crystal structure, their surface electronic states can be optimized to regulate the

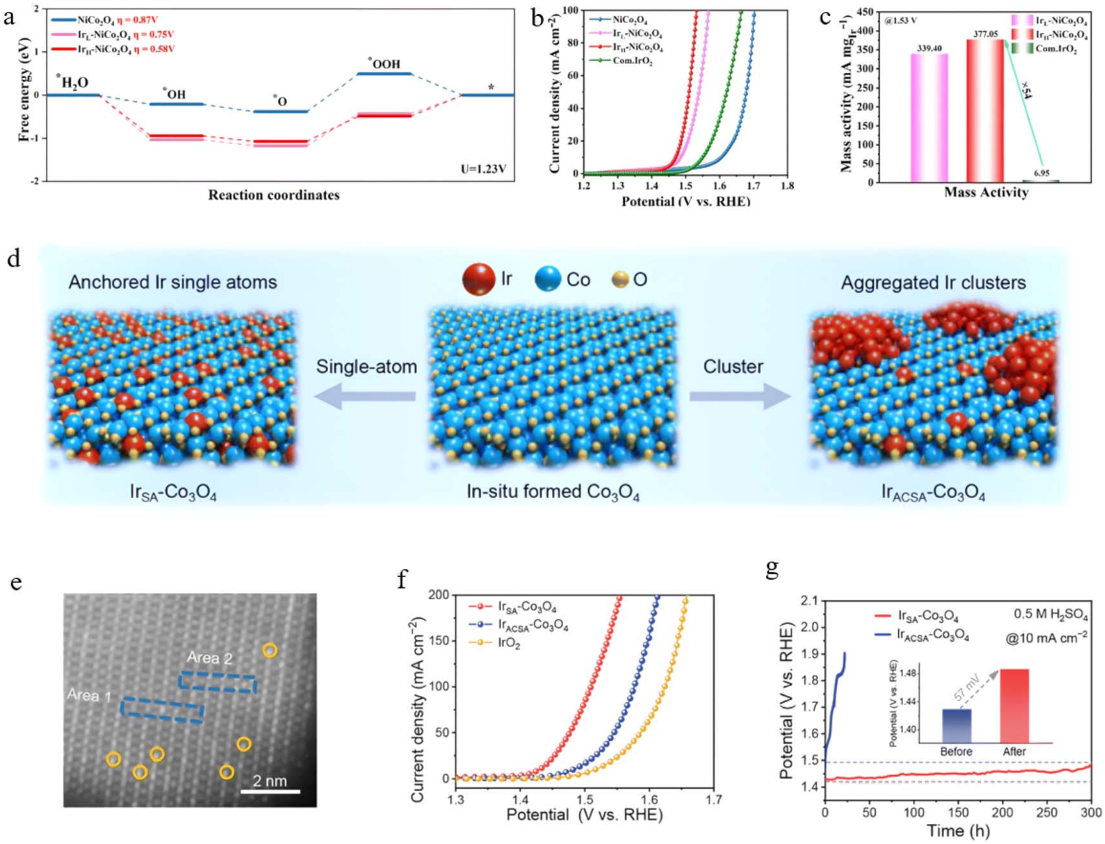

Fig. 4 (a) OER free energy landscape on material Ir_H-$NiCo_2O_4$. (b) LSV curves. (c) Mass activity bar chart.[93] Copyright 2025 Royal Society of Chemistry. (d) Schematic illustration of single-atom loading (Ir_{SA}-Co_3O_4) and cluster-involved loading (Ir_{ACSA}-Co_3O_4) on *in situ* formed Co_3O_4. (e) High-angle annular dark-field scanning transmission electron microscopy (HAADF-STEM) images of Ir_{SA}-Co_3O_4. (f) LSV polarization curves. (g) *I*–*t* curves.[94] Copyright 2026 Royal Society of Chemistry.

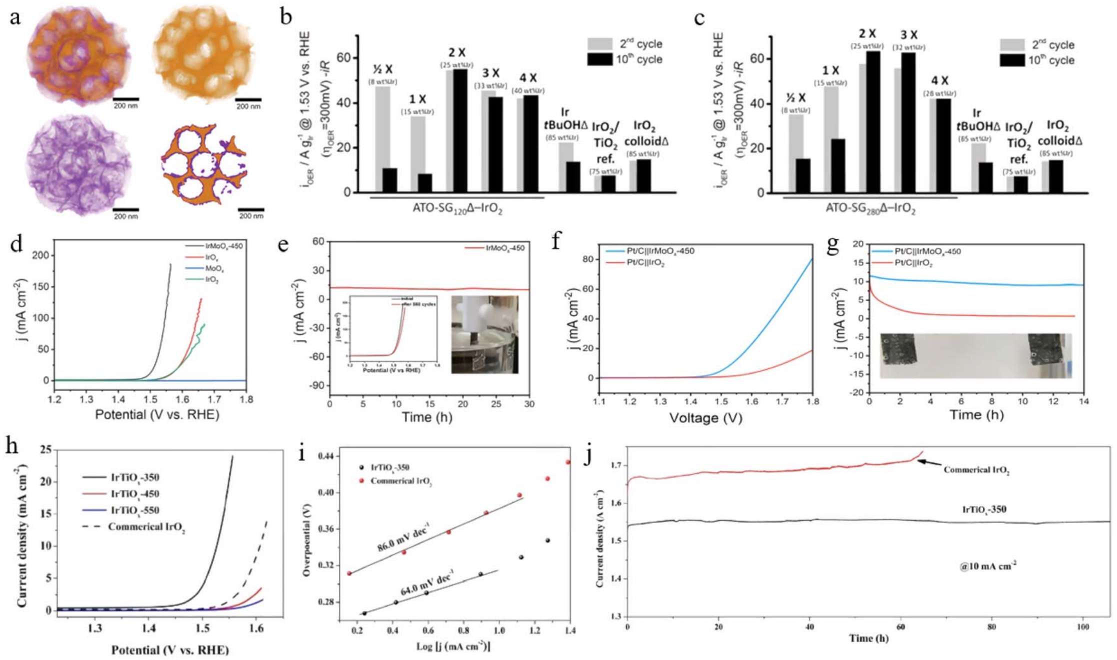

Fig. 5 (a) 3D structural reconstruction of the IrO_2/ATO composite catalyst. The mass-specific activity of IrO_2-loaded ATO on PMMA templates at (b) 120 nm and (c) 280 nm.[97] Copyright 2019 Wiley-VCH Verlag. (d) LSV curves. (e) Stability test of $IrMoO_x$-450. (f) LSV curves of two types of electrolytic cells. (g) Long-term stability test of two electrolyzers.[98] Copyright 2022 Elsevier. (h) LSV curves of $IrTiO_x$ and commercial IrO_2. (i) Tafel slopes. (j) V–t curves.[99] Copyright 2023 Elsevier Ltd.

binding energy of intermediates, which provides a reliable approach for constructing catalytic systems with both high performance and practicality.[96] For instance, Böhm and colleagues developed highly dispersed IrO_2 catalysts by using porous antimony-doped tin oxide inverse opal carriers through solvothermal reduction and thermal oxidation steps.[97] This catalyst exhibited a high pore rate of approximately 89% and an extremely low Ir mass density, enabling it to deliver a mass activity of 63 A g^{-1} (Fig. 5b and c), surpassing commercial catalysts by a considerable margin. Using an electrospinning–calcination approach, the team of Lu produced low-crystallinity $IrMoO_x$ nanofibers.[98] This catalyst demonstrated an overpotential of 267 mV, markedly superior to pure IrO_x, MoO_x, and commercial IrO_2 (Fig. 5d). Studies revealed pronounced electronic coupling between the IrO_x and MoO_x phases, enabling it to remain stable during 30 hours of operation (Fig. 5e). When configured in a full-cell electrolyzer with Pt/C, it recorded an operating voltage of only 1.54 V (Fig. 5f), which surpasses commercial devices by a wide margin. Chen *et al.* used titanium-based MOFs as precursors to successfully prepare iridium–titanium oxide solid solutions ($IrTiO_x$) through a direct calcination strategy, which yielded the rutile-phase material.[99] Exhibiting excellent integrated performance for acidic OER, this material achieves combined metrics of a 296 mV overpotential and a 64 mV dec^{-1} Tafel slope (Fig. 5h and i). After 100 hours of constant-current testing, no activity decay was observed (Fig. 5j), surpassing the commercial IrO_2 benchmark in terms of both durability and catalytic activity Ir alloys, by introducing other metallic elements and utilizing the electronic synergistic effects between components, modulate the electronic environment of catalytic centers while reducing the consumption of precious metals, thereby jointly enhancing catalytic performance and durability.[100,101] Jiang *et al.* introduced yttrium into the Ir crystal lattice and successfully synthesized an IrY alloy nanocatalyst.[102] This catalyst exhibited 255 mV overpotential for the OER (Fig. 6a). More notably, it stably operates exceeding 500 hours (Fig. 6b), exhibiting significant potential for industrial applications. Tan *et al.* successfully prepared a bifunctional Pd–Ir alloy featuring a nanoporous architecture.[103] The optimized $Pd_{50}Ir_{50}$ alloy achieves a low overpotential of 217 mV, outperforming the commercial Ir/C benchmark (Fig. 6e), and its kinetics is further evidenced by a Tafel slope of 58 mV dec^{-1} (Fig. 6f). Furthermore, it shows great potential in overall water electrolysis devices, which demanded a low voltage of 1.52 V to reach 10 mA cm^{-2} while retaining exceptional stability (Fig. 6g and h). Guo *et al.* developed a nano-dendritic iridium–tungsten alloy catalyst (IrW ND).[104] This material exhibited outstanding catalytic performance for OER. Theoretical calculations predicted that the alloying effect of tungsten not only stabilizes the active oxidized iridium species formed during the reaction but also tailors the binding characteristics of intermediates, enhancing the durability and reaction kinetics of Ir. In 0.1 M $HClO_4$, this catalyst achieved 200 mV overpotential while retaining stably operate after 3000 cycles (Fig. 6i and j). When applied in an acidic full-water electrolytic cells, it achieved operating voltage of 1.48 V for 10 mA cm^{-2} (Fig. 6k and l).

Perovskite (ABX_3) and double perovskite ($A_2BB'X_6$) materials possess unique frameworks, and Ir-based perovskites are an ideal platform for precise control of active site electronic structures.[105] The unique crystal structure allows for systematic

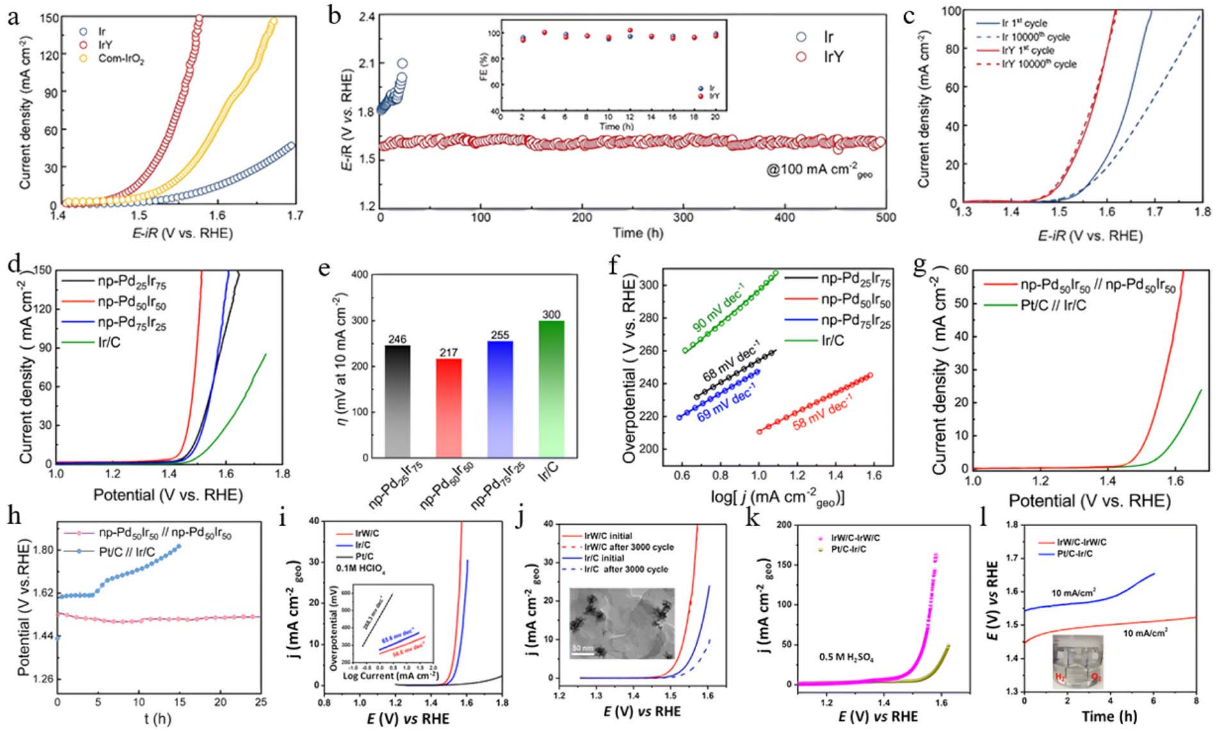

Fig. 6 (a) LSV curves. (b) V–t test of IrY and Ir. (c) LSV curves after accelerated stability test.[102] Copyright 2024 Wiley-VCH Verlag. (d) OER polarization curves. (e) Overpotential plot. (f) Tafel diagram. (g) Complete hydrolysis polarization curves. (h) The complete decomposition V–t curve.[103] Copyright 2023 Royal Society of Chemistry. (i) Polarization curves. (j) Comparison of OER polarization curves after 3000 cycles. (k) The full hydrolysis polarization curves. (l) Durability testing.[104] Copyright 2018 American Chemical Society.

regulation of the covalency of Ir–O bonds through flexible substitution of metal cation sites, which modulates oxygen intermediate adsorption toward optimal values, potentially addressing the longstanding trade-off between catalyst activity and durability.[106] Zou and coworkers introduced a $SrIrO_3$ perovskite material with a 6H-phase crystal structure, characterized by the presence of IrO_6 octahedral dimers connected in a coplanar manner (Fig. 7a and b).[107] This unique structure weakens the Ir–O interaction, significantly enhancing the intrinsic OER performance and durability. Compared to conventional IrO_2, this material features 27.1 wt% reduction in Ir content, yet exhibits seven times higher mass activity. It delivers an overpotential of 248 mV with stable 30 h operation (Fig. 7c and e). By doping Ir elements into the $SrRuO_3$ lattice, Che *et al.* successfully constructed the $SrRu_{0.5}Ir_{0.5}O_3$ double perovskite catalyst.[108] This catalyst shows outstanding performance in acidic OER, exhibiting overpotential of 185 mV combined with stable operation over 50 h (Fig. 7f and h). Studies indicated that the electronic synergy between Ir and Ru effectively boosts the material's intrinsic activity, while the double perovskite structure successfully mitigates lattice oxygen involvement in the reaction pathway, significantly improving the durability of iridium-based catalysts.

3.1.2. Ru-based catalysts.

While offering superior intrinsic activity to their Ir-based counterparts, Ru-based catalysts are hindered by inferior structural stability during prolonged operation. However, the design of atomically dispersed catalysts enables a comprehensive improvement in performance. For example, Peng and coworkers loaded Ru single atoms onto a high-entropy oxide (Fig. 8a), establishing a stable LOM pathway at the Ru sites to simultaneously enhance both activity and structural integrity.[109] The high-entropy effect strengthens Ru 4d-O 2p hybridization and lowers the energy barrier for lattice oxygen oxidation, driving the direct O_{lat}–O_{ad} coupling between lattice oxygen and adsorbed oxygen. Following the disruption of the interfacial hydrogen-bond network, the enriched weakly hydrogen-bonded free water rapidly replenishes lattice oxygen vacancies. This dynamic defect refilling process preserves the coordination environment of the Ru sites and prevents irreversible degradation. Consequently, the catalyst achieved an overpotential of only 204 mV (Fig. 8b) and a mass activity of 5235.42 A g_{Ru}^{-1} at 1.50 V. Furthermore, a PEM electrolysis cell assembled with this catalyst operated stably for over 320 hours at 500 mA cm^{-2} (Fig. 8c). Zhou and colleagues reported the preparation of Ru single-atom sites supported on Co_3O_4 nanorod arrays ($Ru_{8\%}$-Co_3O_4).[110] For the OER, this material achieves superior intrinsic activity with 138 mV overpotential, outperforming both RuO_2 and Pt/C benchmarks (Fig. 8d). When applied in water electrolysis cell, it achieves 1 A cm^{-2} at 2.06 V (Fig. 8f). Chronopotentiometry tests further confirmed its excellent durability (Fig. 8e), showing great practical application potential. Atomically dispersed Ru single-atom sites with a Ru_1–N_4 configuration were engineered on a nitrogen-doped carbon support by the team of Yao.[111] The

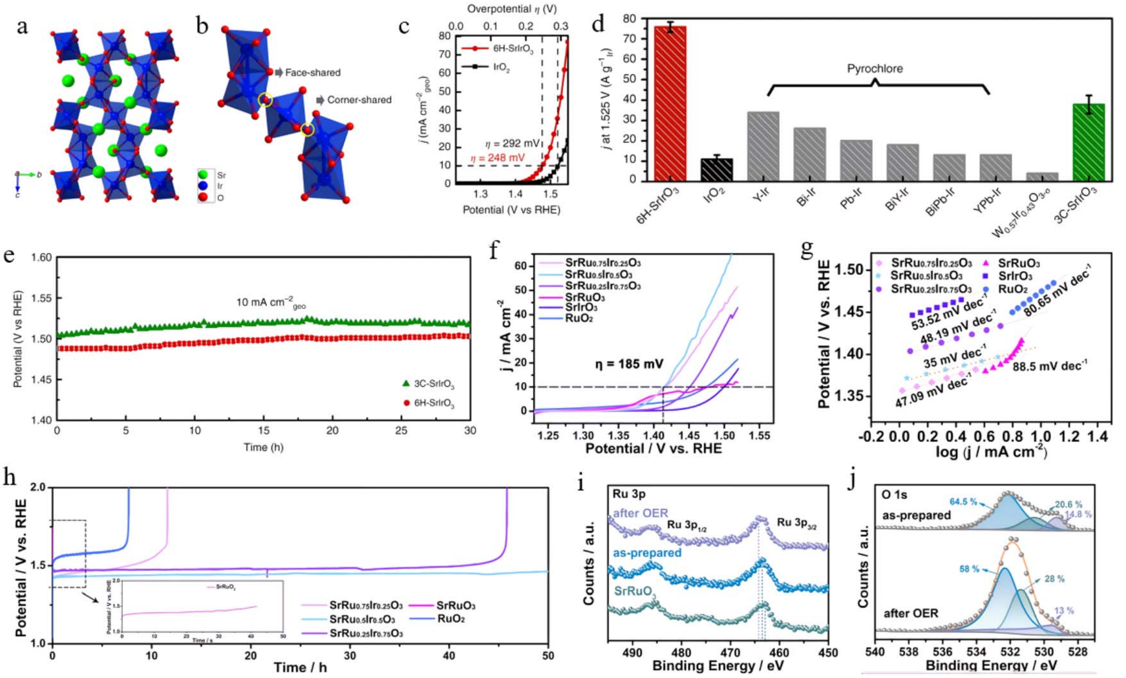

Fig. 7 (a) The crystal structure of 6H-$SrIrO_3$. (b) Local connectivity pattern of IrO_6 octahedra. (c) Polarization curves of 6H-$SrIrO_3$ and IrO_2. (d) Comparison of Ir mass activity with Ir catalysts. (e) V–t curves of 6H-$SrIrO_3$ and 3C-$SrIrO_3$.[107] Copyright 2018 Springer Nature. (f) OER polarization curves of $SrRu_{1-x}Ir_xO_3$ and other catalysts. (g) Tafel plots. (h) V–t stability test. (i) Ru 3p X-ray photoelectron spectroscopy (XPS) spectra. (j) O 1s XPS spectra of $SrRu_{0.5}Ir_{0.5}O_3$.[108] Copyright 2022 Elsevier.

catalyst exhibited an exceptionally high mass activity of 3571 A g^{-1} at 267 mV, showcasing a turnover frequency of 3348 O_2 h^{-1} (Fig. 8i). This catalyst also demonstrated good stability, maintaining its activity without degradation after operation for 30 h in acidic conditions (Fig. 8j).

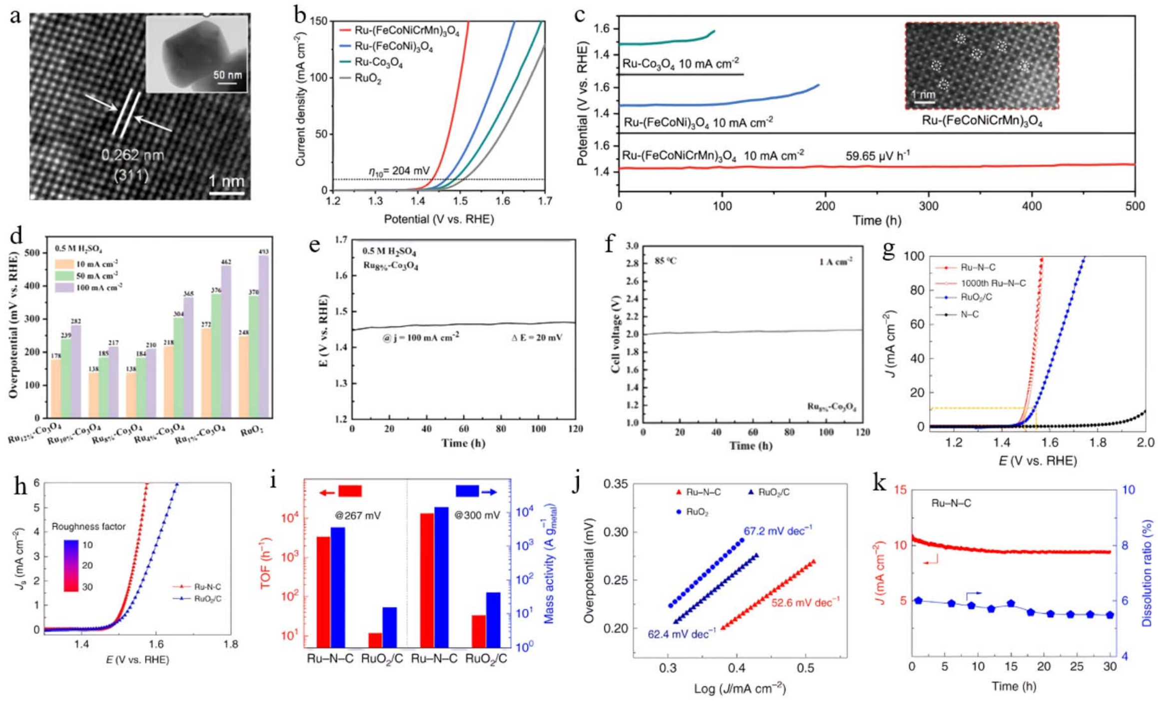

Fig. 8 (a) High-resolution transmission electron microscope (HRTEM) image. (b) LSV curves. (c) V–t stability curves.[109] Copyright 2026 American Chemical Society. (d) Overpotential diagram. (e) V–t stability curve of $Ru_{8\%}$-Co_3O_4. (f) Stability test curve.[110] Copyright 2025 Wiley-VCH Verlag. (g) OER polarization curve. (h) LSV curves. (i) The turnover frequency (TOF) and mass activity plots. (j) Tafel slopes. (k) Current density *versus* Ru dissolution rate over time.[111] Copyright 2019 Springer Nature.

Ru oxides also exhibit high activity and stability in acidic OER. Luo and coworkers constructed a pyridine ligand-based metal–organic framework anchoring strategy, successfully stabilizing atomically dispersed ruthenium oxide on the UiO-67-bpydc carrier (Fig. 9a).[112] Studies showed that the Ru–N bonds formed between the ruthenium oxide and the support promote the participation of lattice oxygen during the OER and stabilize the soluble *Vo-RuO_4^{2-} intermediate. This unique stabilization mechanism significantly enhances OER catalytic performance and endows the catalyst with excellent operational stability over 115 hours (Fig. 9e). Zhao and colleagues successfully constructed a porous RuO_2 electrocatalyst rich in grain boundary structure, which exhibited exceptional performance in acidic OER.[113] The distinctive structural design of the catalyst facilitates exceptional performance, enabling an overpotential of merely 145 mV (Fig. 9f). More importantly, this porous RuO_2 exhibits exceptional long-term stability: in continuous testing lasting up to 50 days, its performance decay rate was only 26 μV h^{-1} (Fig. 9i). The team of Pan prepared a Mn-doped RuO_2 catalyst that achieved a notable activity–stability synergy under acidic OER conditions.[114] Research indicated that Mn incorporation preferentially alters the local coordination of Ru, effectively suppressing Ru overoxidation and dissolution. Moreover, by incorporating Mn, the covalency of Ru–O bonds is increased and the O 2p energy level is elevated (Fig. 9j), thereby promoting the LOM mechanism. The catalyst exhibited an overpotential of 209 mV in acidic OER, and can operate stably for over 180 hours (Fig. 9l), increasing durability by approximately 18 times. In PEM electrolytic cells testing, this catalyst maintains operation for 40 hours at 100 mA cm^{-2} (Fig. 9m), further exhibiting its industrial application potential.

Ru alloys provide a solution to mitigate the stability constraints of pure ruthenium materials through synergistic effects among multiple metals. Yang and colleagues synthesized a coral-like RuCo alloy catalyst supported by a carbon framework on CC surfaces (Fig. 10a).[115] The unique carbon skeleton structure in RuCo@C/CC markedly anchors the RuCo alloy, avoiding its aggregation and separation from CC, while significantly enhancing mass transfer and charge transfer efficiency, which enhances the electrocatalytic performance. Moreover, the electron transfer and redistribution occurring within the RuCo alloy effectively diminishes the reaction barrier required for the OER, thereby enhancing OER performance. In acidic OER, RuCo@C/CC delivers excellent performance, exhibiting 200 mV overpotential (Fig. 10b), significantly outperforming commercial RuO_2. Due to superior OER kinetics, it

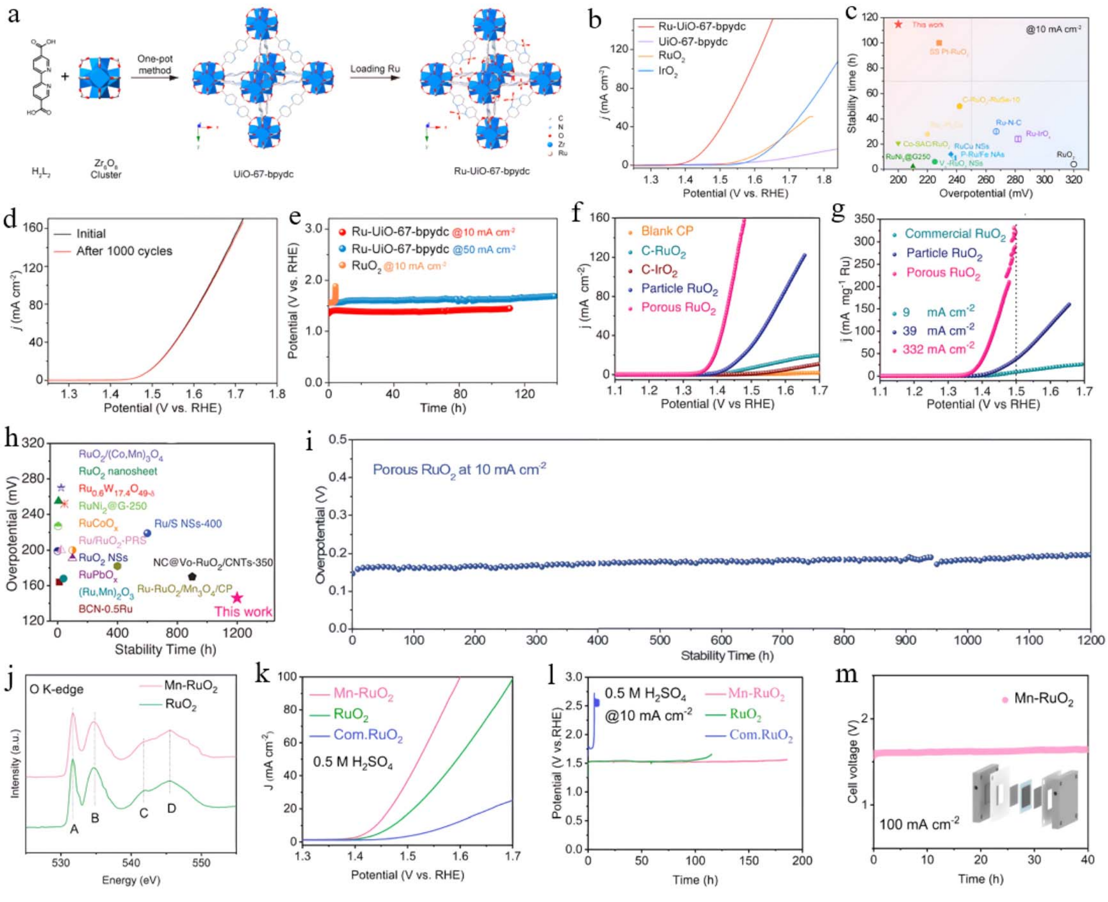

Fig. 9 (a) Preparation process of Ru-UiO-67-bpydc. (b) LSV curves. (c) Comparison of overpotential and stability. (d) LSV curves. (e) *V*–*t* curve.[112] Copyright 2023 Elsevier Inc. (f) LSV curves. (g) Comparison of mass activity. (h) Comparison of overpotentials and stability. (i) *V*–*t* curve of porous RuO_2.[113] Copyright 2024 Wiley-VCH Verlag. (j) X-ray absorption spectroscopy (XAS) spectra of Mn-RuO_2 and RuO_2 at the O K edge. (k) LSV curves. (l) *V*–*t* curve. (m) *V*–*t* curve of PEMWE.[114] Copyright 2025 Elsevier.

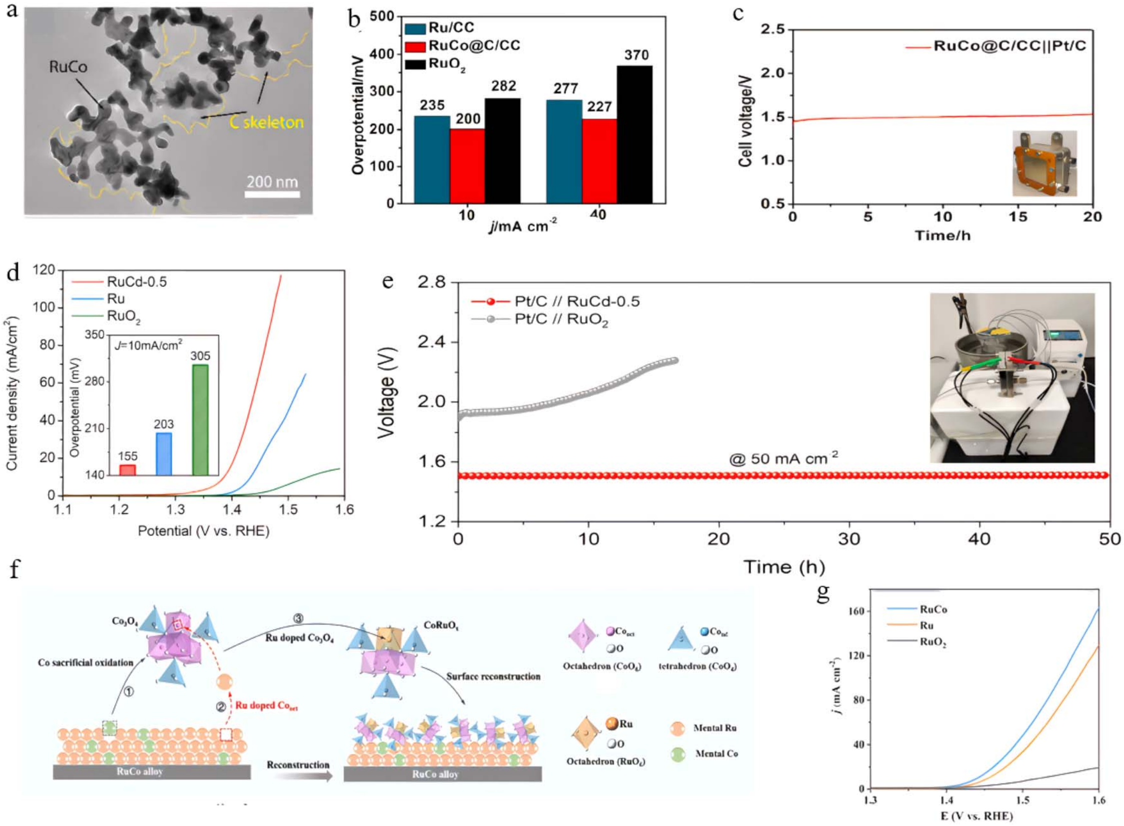

Fig. 10 (a) Transmission electron microscope (TEM) image of RuCo@C/CC. (b) Overpotential comparison. (c) V–t stability test.[115] Copyright 2024 Elsevier Ltd. (d) LSV curves. (e) V–t curves of PEMWE.[116] Copyright 2024 American Chemical Society. (f) Schematic diagram of the reconstruction process of RuCo catalysts. (g) LSV curves.[117] Copyright 2015 Wiley-VCH Verlag.

also demonstrates outstanding stability in practical PEMWE testing (Fig. 10c). Du *et al.* employed pulsed laser ablation technology to successfully prepare RuCd alloy nanocatalysts with special structure.[116] These catalysts exhibited exceptional OER performance, achieving 155 mV overpotential (Fig. 10d), significantly surpassing commercial RuO_2. Analysis indicated that Cd doping effectively lowers the kinetic barrier and simultaneously enhances the catalyst's structural robustness. When applied in PEMWE testing, the RuCd alloy anode can stably operate for over 50 h at 50 mA cm^{-2} (Fig. 10e), demonstrating promising practical application potential. Deng *et al.* designed and synthesized a RuCo alloy catalyst that achieves synergistic improvement in both catalytic performance and structural durability in acidic OER.[117] The Ru-doped Co_3O_4 surface layer formed during the reaction not only prevents Ru leaching but also optimizes the reaction pathway. It exhibits 210 mV overpotential 0.1 M $HClO_4$ (Fig. 10g), with operational stability exceeding 120 hours. Its overall performance far exceeds that of traditional ruthenium-based materials.

Ru-based perovskites have emerged as a crucial system for addressing the stability challenges of ruthenium-based catalysts, due to the distinctive electronic structure and excellent lattice stability. Rojas *et al.* doped Na^+ into $SrRuO_3$ perovskite, achieving a remarkably low overpotential of 120 mV at 0.5 mA cm^{-2} in 0.1 M $HClO_4$ (Fig. 11a).[118] The incorporation of Na^+ not only enhanced the resilience of the perovskite structure against degradation but also effectively suppressed catalyst degradation in acidic media by reducing surface energy and increasing dissolution potential. Retuerto *et al.* investigated a series of double perovskite materials and found that Dy_2NiRuO_6 exhibited outstanding comprehensive performance in acidic OER.[119] Analysis revealed that the reduced Ru–O distance in the lattice strengthened the enhanced d–p hybridization (Fig. 11j and l), elevating the oxidation state of ruthenium and optimizing the adsorption energy of reaction intermediates. This material exhibits an overpotential of 263 mV in 0.1 M $HClO_4$ (Fig. 11g), and remained stable after 300 cycles (Fig. 11k).

Beyond conventional trial-and-error synthesis, high-throughput density functional theory (DFT) and machine learning (ML) have recently emerged as powerful tools to guide the rational discovery of acidic OER catalysts. In practice, ML-driven high-throughput screening has successfully identified promising catalysts that have been experimentally validated. For instance, Yang *et al.* investigated the phase formation, OER performance, and surface reconstruction of $Ru_x(Ir, Fe, Co, Ni)_{1-x}$ multicomponent alloys.[120] At near-equimolar ratios, the alloy exhibits a multiphase structure dominated by a face-centered cubic (fcc) phase with a minor coexisting hexagonal close-packed (hcp) phase. The combination of machine-learned interatomic potentials (MLIP) and molecular dynamics

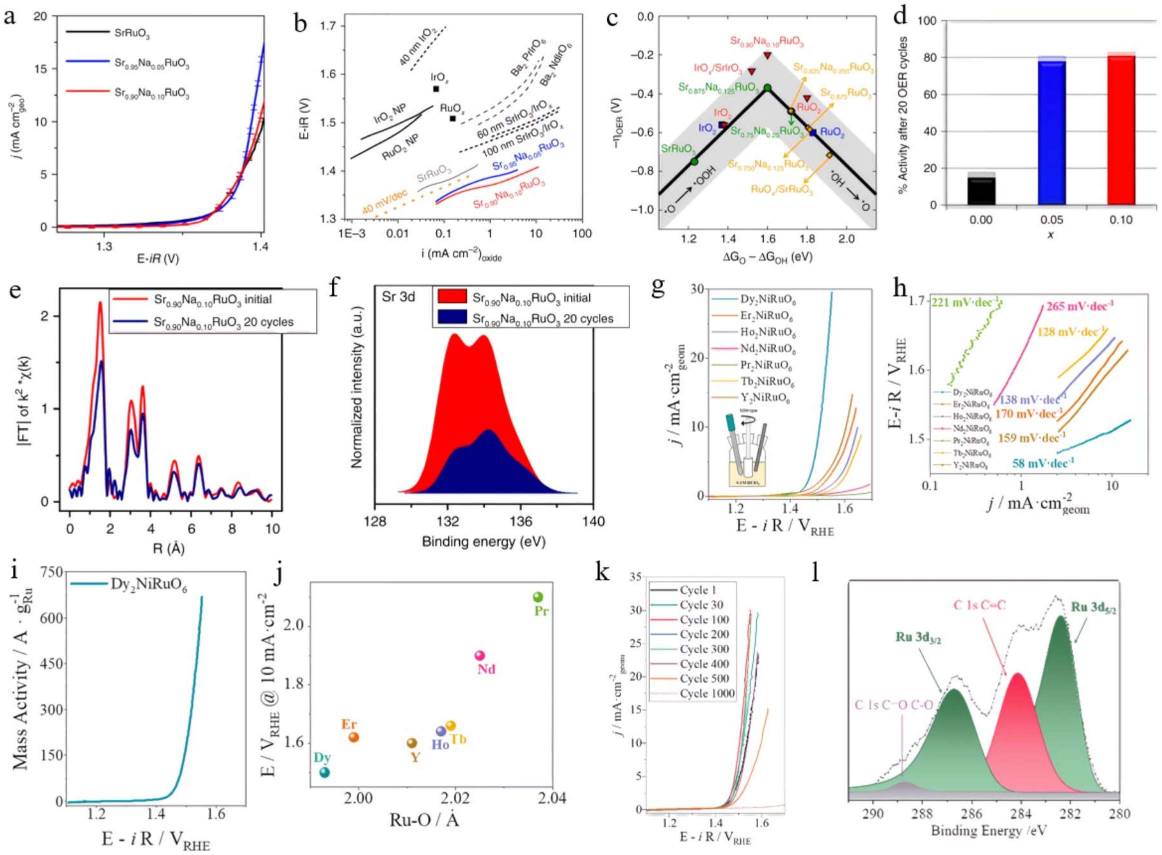

Fig. 11 (a) LSV curves of $Sr_{1-x}Na_xRuO_3$. (b) Tafel diagram. (c) OER volcanic activity map. (d) Retention rate of $Sr_{1-x}Na_xRuO_3$ relative to initial activity after 20 OER cycles. (e) Fourier transform of the Ru K-edge EXAFS signal for $Sr_{0.90}Na_{0.10}RuO_3$. (f) XPS spectra of Sr 3d before and after OER cycles for $Sr_{0.90}Na_{0.10}RuO_3$.[118] Copyright 2019 Springer Nature. (g) Polarization curve of R_2NiRuO_6 after 30 OER cycles. (h) Tafel diagram of R_2NiRuO_6 after 30 OER cycles. (i) Ru mass activity plot of Dy_2NiRuO_6. (j) Relationship between the potential of R_2NiRuO_6 and the Ru–O bond distance. (k) Polarization curve of Dy_2NiRuO_6 after 1000 consecutive cycles. (l) XPS spectrum of Ru 3d + C 1s for Dy_2NiRuO_6.[119] Copyright 2024 Royal Society of Chemistry.

simulations revealed the atomic-scale mixing behaviour of the alloy and corroborated the experimentally observed fcc-dominated characteristics. The optimized $Ru_{0.20}(Ir, Fe, Co, Ni)_{0.80}$ catalyst demonstrates outstanding activity and stability in 0.1 M $HClO_4$, achieving an overpotential of approximately 237 mV with a low degradation rate of about 1.1 mV h^{-1} over 24 hours. Under acidic OER conditions, a RuIr-enriched oxide shell forms on the catalyst surface, where Ru species become stabilized at the nanoparticle surface. Moreover, Lv's team leveraged machine learning to break the activity–stability trade-off.[121] By constructing a back-propagation neural network for high-throughput calculation and cross-validation of Ru/Ti/Mn ternary compositions, they accurately predicted the optimal ratio that balances low overpotential with a low deactivation rate. This approach significantly shortened the research and development, eliminating the blindness inherent in traditional trial-and-error methods for multicomponent catalyst design. Building on this, they pioneered a chemical vapor deposition (CVD) strategy. Using strong oxidants, reactants from precursor solutions were oxidized into a gaseous state, allowing them to react at the atomic/molecular scale and directly construct an integrated $Ru/TiMnO_x$ electrode with intrinsic metal–support interactions. This structure effectively suppresses Ru dissolution and aggregation, resulting in a significantly enhanced mass activity across a wide pH range and enabling stable operation under acidic conditions for up to 3000 hours. In summary, machine learning-accelerated computational screening can effectively narrow down the search space for high-performance acidic OER catalysts, thereby enabling a transition from pure theoretical prediction to actionable experimental guidance.

3.1.3. Other noble metal catalysts.

Besides the conventional use of iridium and ruthenium, other noble metals including platinum, palladium, and rhodium represent additional candidate materials for acidic OER, but their intrinsic activity is relatively poor and they are usually not used as the main active centers. However, their performance can be improved to some extent through modification by combining with other metals. For example, Chen and coworkers supported RuFe nanoparticles on carbon felt (RuFe@CF) *via* an ultrafast Joule heating method.[122] This catalyst exhibits excellent OER activity and stability under acidic conditions, achieving an overpotential of only 188 mV and maintaining high stability for 620 hours during continuous operation. When employed as the anode in a PEMWE, the device operates stably for over 250 hours at 200 mA cm^{-2}. Experimental characterizations reveal that an *in situ* generated ruthenium-based oxide nanosheet forms on the catalyst surface during the OER process, playing a crucial role in boosting its performance. Moreover, Yu *et al.* successfully synthesized $Rh_{22}Ir_{78}$ alloy nanoparticles with a size less than 10 nm and compositionally adjustable ratios *via* a microwave-assisted approach on Vulcan XC-72R carbon (Fig. 12a).[123] This catalyst demonstrated exceptional catalytic activity, showing a threefold enhancement in mass activity over pure Ir nanoparticles at 300 mV, reaching up to 1.17 A mg^{-1}. Xia *et al.* successfully developed a ternary metal catalyst based on cubic $Pt_{39}Ir_{10}Pd_{11}$ nanocage structure (Fig. 12e).[124] This catalyst exhibited an overpotential of 372 mV (Fig. 12f). After 10 000 cycles, its mass activity loss is only 11%, demonstrating superior electrocatalytic performance (Fig. 12h).

3.2. Non-noble metal catalysts

A central issue in catalyst research is to circumvent the reliance on precious metals, which motivates the exploration of non-noble metal alternatives. Although current non-noble metal catalysts still show certain performance gaps compared to noble metals, significant progress has been made through precise electronic modulation and morphology design.[125,126] The non-noble metal catalysts mainly include transition metal oxides, nitrides, sulfides, carbides, and others.

3.2.1. Transition metal oxides. Dong's team successfully prepared trace manganese-doped cobalt spinel oxides using a specific Co-MOF precursor (CoBDC) *via* a facile room-temperature ion-exchange method.[127] Although the introduction of trace Mn increased the number of pores, it did not disrupt the crystal structure or the intrinsic activity of the cobalt spinel oxides. Benefiting from the Mn-induced enhancement of Co–O bond hybridization, the stability of $Mn_{0.08}$-Co_3O_4-400 in strongly acidic environments was improved by 4–5 times compared to Co_3O_4-400. Krishnan *et al.* proposed a method to prepare manganese oxide-modified carbon (MnO@C) *via* a one-step pyrolysis strategy using beech leaves as the carbon source.[128] The resulting MnO@C electrocatalyst exhibits excellent OER performance, and a lab-scale water electrolyzer assembled with this catalyst requires a cell voltage of only 1.65 V to drive water splitting. Xu *et al.* found that doping Co_3O_4 with single-atom W spinel crystal lattice constructed a W-Co_3O_4 catalyst with superior OER catalytic performance.[129] This material demonstrated an overpotential of only 251 mV and showed almost no performance degradation during prolonged operation. Studies indicated that W exhibits higher OER activity

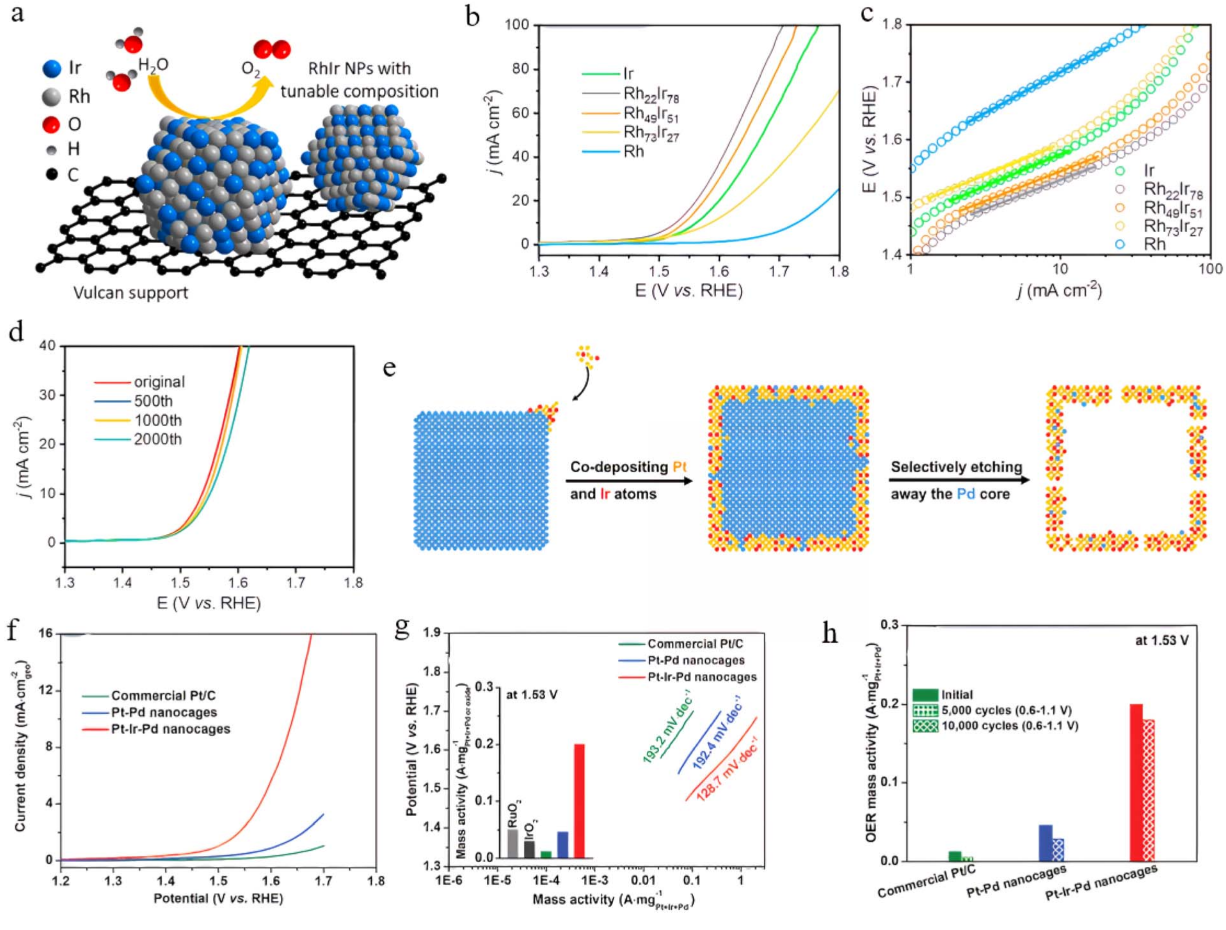

Fig. 12 (a) Schematic diagram of $Rh_xIr_{(100-x)}$ nanoparticles loaded on carrier. (b) OER polarization curves. (c) Tafel plot. (d) Polarization curves of $Rh_{22}Ir_{78}$/VXC after different numbers of OER cycles.[123] Copyright 2019 American Chemical Society. (e) Schematic of the synthesis of Pt-Ir-Pd nanocages. (f) OER polarization curves. (g) Tafel curve. (h) Change in mass activity.[124] Copyright 2020 Wiley-VCH Verlag.

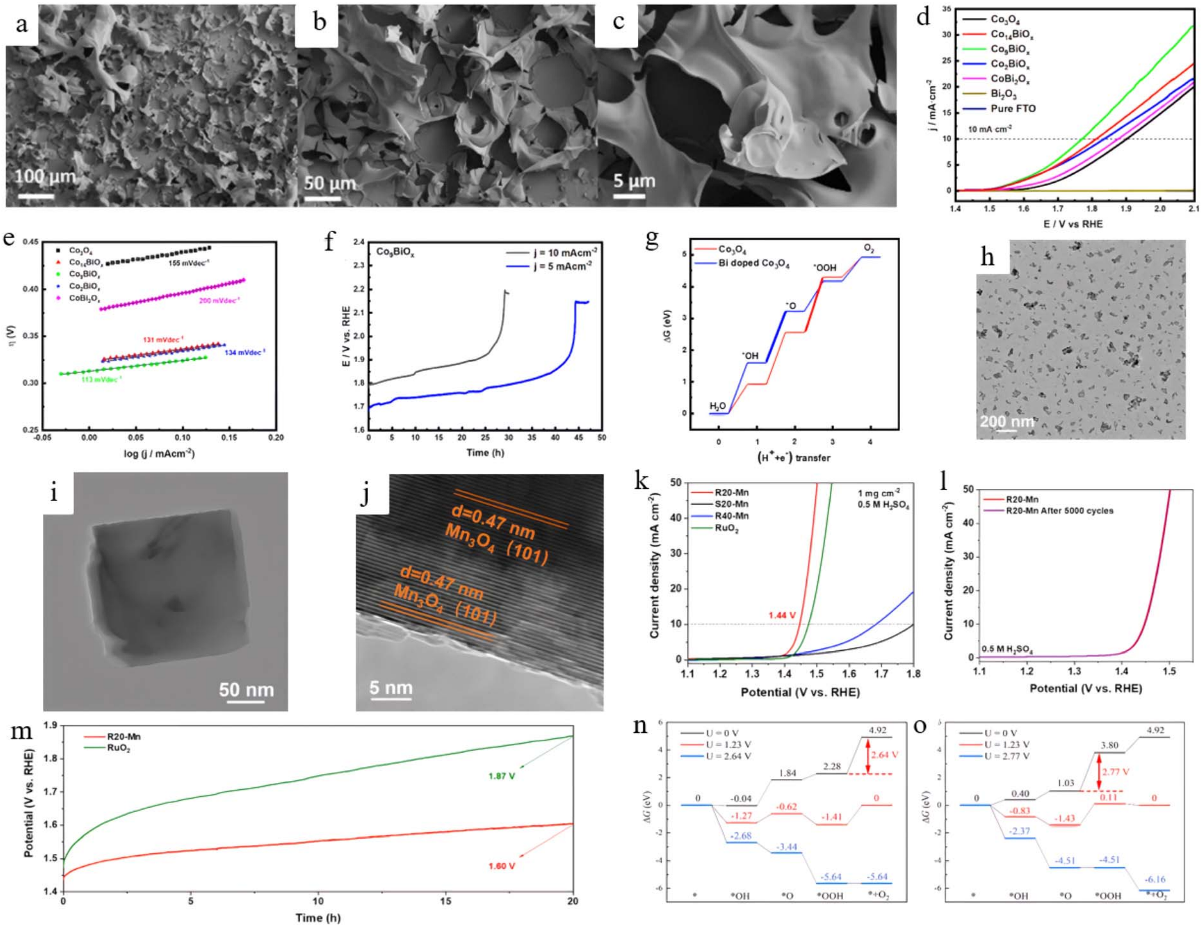

Fig. 13 (a–c) Scanning electron microscope (SEM) images of Co_9BiO_x on FTO. (d) LSV curves. (e) Tafel diagram. (f) *V*–*t* curves of Co_9BiO_x. (g) Free energy change of OER on Co_3O_4(100) surface and Bi-doped Co_3O_4 surface.[130] Copyright 2024 Royal Society of Chemistry. (h) TEM and (i and j) HRTEM images of sample. (k) LSV curves. (l) LSV curves of R20-Mn before and after 5000 accelerated durability tests. (m) *V*–*t* curves of R20-Mn nanosheets and RuO_2. (n) Δ*G* of OER on R20-Mn surface. (o) Δ*G* of OER on RuO_2 surface.[131] Copyright 2022 Academic Press Inc.

than Co. Importantly, it effectively mitigates the degradation of surface Co and O atoms, thus improving the overall activity and robustness. Asefa's group incorporated Bi into a Co_3O_4 lattice, which significantly enhanced its acidic OER performance while maintaining material stability.[130] When Co : Bi = 3 : 1, the prepared Co_3BiO_x catalyst exhibited optimal performance, which has an overpotential of 540 mV in 0.1 M $HClO_4$ (Fig. 13d). Meanwhile, this catalyst demonstrated good stability, maintaining operation for approximately 45 hours (Fig. 13f). Lei *et al.* successfully prepared single-phase manganese dioxide nanosheets (R20-Mn) *via* rapid annealing method (Fig. 13i and j), which demonstrated exceptional overall performance.[131] It achieves an ultralow overpotential of 210 mV (Fig. 13k), and its performance remains almost unchanged after 5000 cycles (Fig. 13l). Both its activity and durability surpass those of RuO_2, and its excellent intrinsic activity has been verified through theoretical calculations (Fig. 13n and o).

3.2.2. Transition metal nitrides.

Zhou *et al.* transformed $CuInP_2S_6$ into novel noble-metal-free, atomically thin $CuInP_2N_x$ nanosheets *via* a facile nitridation process for electrochemical water splitting.[132] Leveraging the dual advantages of metal nitrides and a 2D morphology, the material exhibits an overpotential of only 356 mV for the acidic OER and maintains stable operation for up to 60 hours. The study revealed that the incorporation of nitrogen effectively modulates the electronic structure of $CuInP_2N_x$, significantly lowering the energy barriers of reaction intermediates, thereby making the OER thermodynamically more favourable. Jiang *et al.* combined carbon nitride matrix with acetate-based graphene and successfully developed a high-performance functional material through heteroatom doping strategy.[133] It displayed an overpotential of 211 mV in acidic OER. Meanwhile, its faradaic efficiency reached 92.7%, and it retained 92% of its initial performance after 150 hours of operation, demonstrating excellent durability.

3.2.3. Transition metal carbides.

Sheng's team proposed an electrochemical reconstruction strategy to construct a nitrogen-doped, multi-hybrid biomass carbon electrode featuring two-coordinate copper single atoms.[134] This was achieved using copper single-atom-embedded carbonized wood as the substrate, through the electrochemical reconstruction of alkynyl polymers coupled with anode-to-cathode metal ion transfer and deposition. The voltage-driven lattice strain

Table 1 Summary of representative OER electrocatalysts and their catalytic performance

Catalyst	η_{10} (mV)	Mass activity	Tafel slope (mV dec^{-1})	Dominant mechanism
Ir_H-$NiCo_2O_4$	240	377.05 mA mg_{Ir}^{-1}	53.05	AEM
Ir_{SA}-Co_3O_4	199	—	56.5	AEM
$IrMoO_x$ nanofibers	267	46.63 A g_{Ir}^{-1}	46.09	—
$IrTiO_x$-350	296	—	64.0	—
IrY alloy	255	—	54.8	AEM
np-$Pd_{50}Ir_{50}$	217	2.50 A mg_{Ir+Pd}^{-1}	58	—
6H-$SrIrO_3$	248	—	—	AEM
$SrRu_{0.5}Ir_{0.5}O_3$	185	144.6 A g_{Ru}^{-1}	35	AEM
Ru-$(FeCoNiCrMn)_3O_4$	204	5235.42 A g_{Ru}^{-1}	—	LOM
$Ru_{8\%}$-Co_3O_4	138	—	60.6	AEM
Ru-UiO-67-bpydc	200	—	78.3	LOM
Porous RuO_2 (GB-rich)	145	332 mA mg_{Ru}^{-1}	40.9	AEM
RuCo@C/CC	200	—	48	AEM
RuCd-0.5 alloy	155	—	60.8	AEM
Dy_2NiRuO_6	277 (0.1 M $HClO_4$)	—	58	AEM
$Rh_{22}Ir_{78}$ alloy	292	1.17 A mg_{Ir}^{-1}	—	AEM
Pt-Ir-Pd nanocage	408	0.22 A $mg_{Pt+Ir+Pd}^{-1}$	128.7	—
$Mn_{0.08}$-Co_3O_4-400	430	—	73.7	—
$CuInP_2N_x$-300	356	—	159	AEM
PDEB/NCW-1.4	178	—	183	—
Co_3S_4@MoS_2@20TiPCP	247	—	91.1	AEM

induces the formation of grain boundaries and compacts the carbon skeleton, which significantly enhances electron transfer kinetics and optimizes the intrinsic reactivity of the active sites. Consequently, the resulting electrode exhibited an overpotential of 178 mV for the acidic OER. Huang and colleagues synthesized bimetallic carbide $TiTaC_2$ *via* a hydrothermal treatment followed by an annealing process.[135] Subsequent fluorine doping yielded $TiTaF_xC_2$, which effectively boosted the catalytic activity. The resulting reduced graphene oxide-supported $TiTaF_xC_2$ nanoparticles ($TiTaF_xC_2$ NP/rGO) exhibited outstanding OER performance, surpassing even the benchmark Ir/C catalyst, and demonstrating rapid reaction kinetics and excellent durability.

3.2.4. Transition metal sulphides. Li *et al.* prepared Co_3S_4@MoS_2@20TiPCP, which exhibits an overpotential of only 247 mV for the acidic OER.[136] More remarkably, an electrolyzer constructed using this material as both the cathode and anode achieves a low cell voltage of only 1.41 V at 10 mA cm^{-2} in acidic conditions, demonstrating excellent long-term stability and outperforming most reported electrocatalysts. Jin's team reported a facile and cost-effective synthesis method for preparing spinel-structured, carbon-supported cobalt-based electrocatalysts (Co_3S_4@rGO).[137] The study revealed that the formation of Co–S bonds within the Co_3S_4 loaded on the reduced graphene oxide surface effectively modulates the electronic structure of the electrocatalyst. The resulting nanostructured catalyst exhibited outstanding catalytic activity, achieving an OER overpotential of only 350 mV (Table 1).

4. Structural regulation strategies

Currently, research on catalysts has made certain progress, but the performance of most catalysts remains suboptimal compared to the ideal scenario. Therefore, adopting appropriate strategies to modulate the electronic configuration and geometric morphology of catalytic materials can improve their performance to some extent.

4.1. Electronic structure regulation

Regulating the d-band center and electron occupation of active sites *via* doping or defect engineering optimizes intermediate adsorption, thus markedly lowering the reaction energy barrier.[138] Moreover, tuning the electronic structure strengthens the covalent character of the M–O bonds, stabilizes high-valent active species, thereby synergistically improving both catalytic activity and stability.[139]

4.1.1. Doping engineering. Doping engineering represents an essential approach for the precise performance modulation of catalysts. By doping other atoms into the catalyst matrix, it enables effective control over the material's electronic configuration and coordination environment at the atomic scale, thereby synergistically improving catalytic performance and durability.[140] Liu *et al.* strategically doped Mn atoms into the CoO lattice and confined the resulting bimetallic oxide within hollow mesoporous carbon spheres.[141] The as-prepared catalyst exhibited significantly enhanced electrocatalytic activity. This approach modifies the electronic configuration of the material, adjusts the d-band center position of active sites, and modulates the binding energy of intermediates, significantly reducing the reaction overpotential. Meanwhile, by incorporating dopant elements with strong binding affinity to oxygen, the M–O bond strength is enhanced, effectively suppressing the dissolution and phase transformation of active components in harsh acidic environments, thus extending the catalyst's service life.[142–145] Furthermore, specific dopants can improve the covalency of M–O bonds, inducing an alteration of the reaction pathway from the AEM framework to more efficient LOM or OPM, fundamentally breaking through the bottleneck of catalytic performance.[146] For instance, Fu *et al.* achieved synergistic regulation of the electronic structure and surface defects in RuO_x catalysts through Fe/Co doping strategies (Fig. 14a and b).[147] This strategy not only reduced the oxidation state of Ru but also decreased the oxygen vacancies, significantly improving the catalytic performance. The optimized Fe-RuO_x and Co-RuO_x exhibited overpotentials of 191 mV and 203 mV in OER, respectively, and both could stably operate for over 500 hours (Fig. 14c and d). Moreover, in PEMWE applications, both catalysts could sustain operation for 250 hours (Fig. 14e). Theoretical calculations indicate that Fe/Co doping cuts down the adsorption energy of the OOH*, effectively lowering the reaction energy barrier (Fig. 14g), while abundant oxygen vacancies suppress Ru dissolution by increasing surface reconstruction energy, collectively enhancing catalytic activity and durability. Gao and coworkers successfully constructed an oxygen-vacancy-rich catalytic system by doping Ce into IrO_2.[148] It demonstrated only 240 mV overpotential in acidic OER (Fig. 14f), with operation lasting over 50 hours (Fig. 14g). In a water electrolytic cell, this catalyst achieves 1.54 V at 10 mA cm^{-2}, along with stable operation exceeding 20 hours (Fig. 14h and i). Research showed that the cooperative interaction of the Ce-doping induced nanoparticle structure and abundant oxygen vacancies optimizes the catalyst's reaction pathway and improves electron transport efficiency.

Additionally, Liu's group attained exact modulation of the electronic structure by doping Mn into RuO_2/CeO_2 heterostructure.[149] Studies showed that the introduction of Mn not only enhances interfacial coupling but also effectively stabilizes Ru in higher oxidation states. This electronic structure optimization effectively fine-tunes the Ru d-band center, significantly decreasing the reaction energy barrier. Meanwhile, the preferential oxidation property of Mn synergizes with the electron transfer, markedly mitigating the over-involvement of lattice oxygen and the leaching of Ru. Based on these advantages, the Mn-RuO_2/CeO_2 catalyst demonstrates merely 227 mV overpotential in 0.1 M $HClO_4$, maintaining excellent stability even after 300 hours of operation. The team of Liang demonstrated that Hf-doped $ReSe_2$ monolayers exhibited significant catalytic potential for acidic OER, with a Gibbs free energy barrier as low as 0.805 eV.[150] This outstanding performance arises from the dual modulation effect of Hf doping: the induced lattice strain and substantial charge transfer jointly modulate the electronic properties of the material, positioning the d-band center optimally for moderate adsorption of reaction intermediates. By introducing non-noble metal tungsten (W) into IrRu oxide, Fan *et al.* successfully achieved a breakthrough improvement in catalyst performance.[151] It was found that W-doped $IrRu_3O_x$ (W-$IrRu_3O_x$) undergoes dynamic restructuring during the OER process, where partial leaching of W promotes uniform distribution of active components. Moreover, its unique electronegativity effectively regulates the electronic structures of Ir and Ru. On one hand, this doping strategy promotes the formation of highly active Ir^{5+} species, while on the other hand, significantly inhibits the generation of soluble Ru^{4+}, achieving dual improvement in catalyst performance and long-term stability. In electrolytic cells, W-$IrRu_3O_x$ exhibits

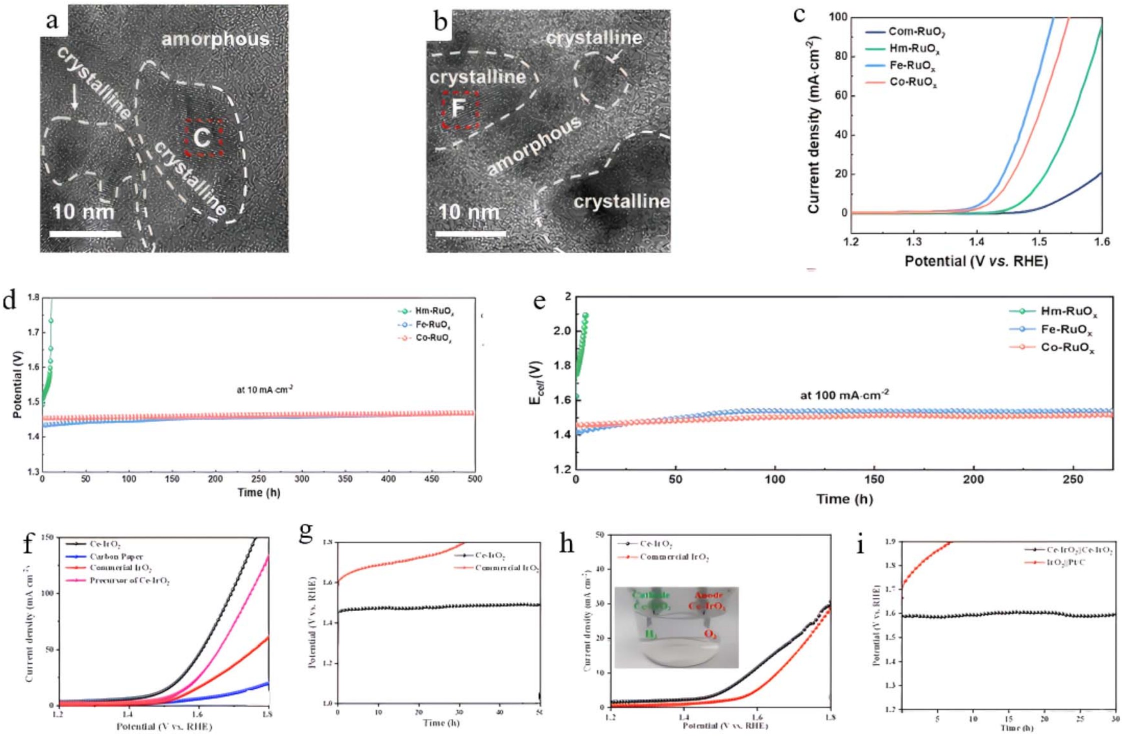

Fig. 14 TEM images of (a) Fe-RuO_x and (b) Co-RuO_x. (c) LSV curves. Stability test at (d) 10 mA cm^{-2} and (e) 100 mA cm^{-2}.[147] Copyright 2025 American Chemical Society. (f) LSV curves. (g) $V-t$ stability test curves. (h) LSV curves under different electrode configurations. (i) Stability testing for PEMWE.[148] Copyright 2024 Elsevier.

exceptional catalytic performance, featuring not only superior OER activity but also stable operation exceeding 500 hours. However, doping also brings adverse effects to catalysts. For instance, under acidic conditions and high anodic potentials, most transition metal dopants undergo dynamic reconstruction, thereby losing the regulatory effect of doping.[152] Moreover, the impact of doping on performance exhibits a strict volcano-type relationship.[153] While low-dose doping can precisely optimize the electronic structure, excessive doping disrupts the long-range ordered lattice of rutile-type RuO_2/IrO_2. This leads to the formation of abundant amorphous phases and lattice defects, which in turn provide more channels for acidic electrolyte attack, accelerating the corrosion and collapse of the host lattice. Therefore, it is preferable to select oxide systems with rigid lattice frameworks, such as rutile-type RuO_2 and IrO_2, and to incorporate dopants with high dissolution potentials and high acid stability (*e.g.*, Sb, Sn, Ce, Ti). Meanwhile, the dopant concentration should be strictly controlled to prevent the disruption of long-range lattice ordering caused by excessive doping.

4.1.2. Defect engineering. Defect engineering is a prevalent strategy for modulating the catalytic efficacy of materials in acidic oxygen evolution, achieving synergistic optimization of the material's electronic structure and surface environment by precisely constructing structural defects such as oxygen vacancies and grain boundaries.[154,155] Introducing point defects such as oxygen vacancies or cation vacancies at the atomic scale can effectively fine-tune the electronic density and d-band center alignment at the reaction sites, enhance the covalency of M–O bonds, thereby modulating the adsorption strength of oxygen intermediates and significantly downing the reaction overpotential.[156–158] The defective sites not only serve as highly active centers participating in catalytic reactions but also stabilize high-valent metal species to suppress excessive oxidation and dissolution of active components. More importantly, certain types of defects can induce new reaction pathways, breaking through the limitations of AEM.[159] Moreover, constructing extended defects including grain boundaries can effectively tune the electronic conductivity and ionic diffusion rate of the catalyst, enhancing mass transfer efficiency during the reaction process.[160] It is worth noting that controlling defect density is crucial: an appropriate defect density can provide abundant active sites and optimize reaction pathways, whereas excessive defects may destabilize the crystal structure and instead accelerate catalyst corrosion and degradation.[161,162] Through a synergistic strategy of electrodeposition and acid etching, Zhang *et al.* successfully constructed $RuO_2/D\text{-}Co_3O_4/CC$ composites with dual defect structure (Fig. 15a and b).[163] With

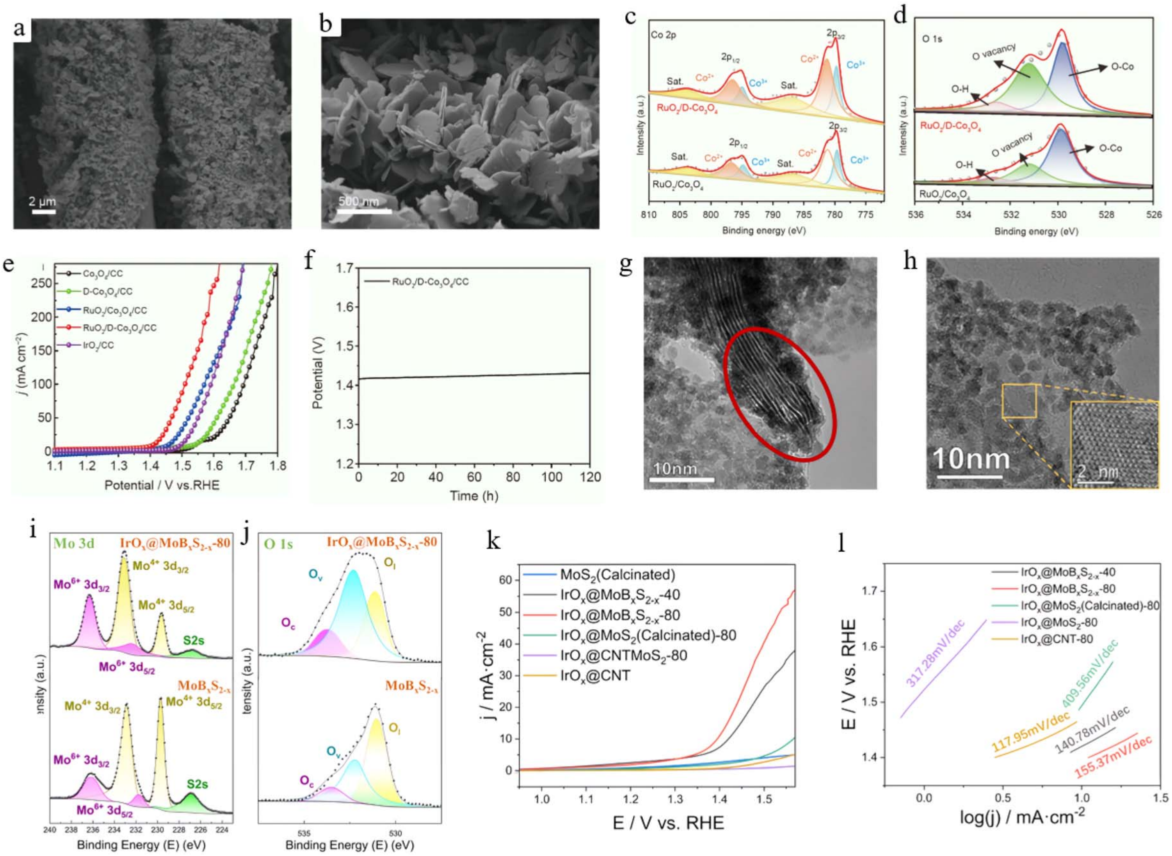

Fig. 15 (a) Low-resolution and (b) high-resolution SEM images of $RuO_2/D\text{-}Co_3O_4/CC$. (c) XPS spectra of Co 2p for $RuO_2/D\text{-}Co_3O_4$ and RuO_2/Co_3O_4. (d) O 1s XPS spectra. (e) OER polarization curves. (f) $V{-}t$ curve of $RuO_2/D\text{-}Co_3O_4/CC$.[163] Copyright 2024 Science China Press. (g and h) TEM image of $IrO_x@MoB_xS_{2-x}$-80. (i) Mo 3d XPS spectra of MoB_xS_{2-x} and $IrO_x@MoB_xS_{2-x}$-80. (j) O 1s XPS spectra. (k) LSV curves. (l) Tafel diagram.[164] Copyright 2024 American Chemical Society.

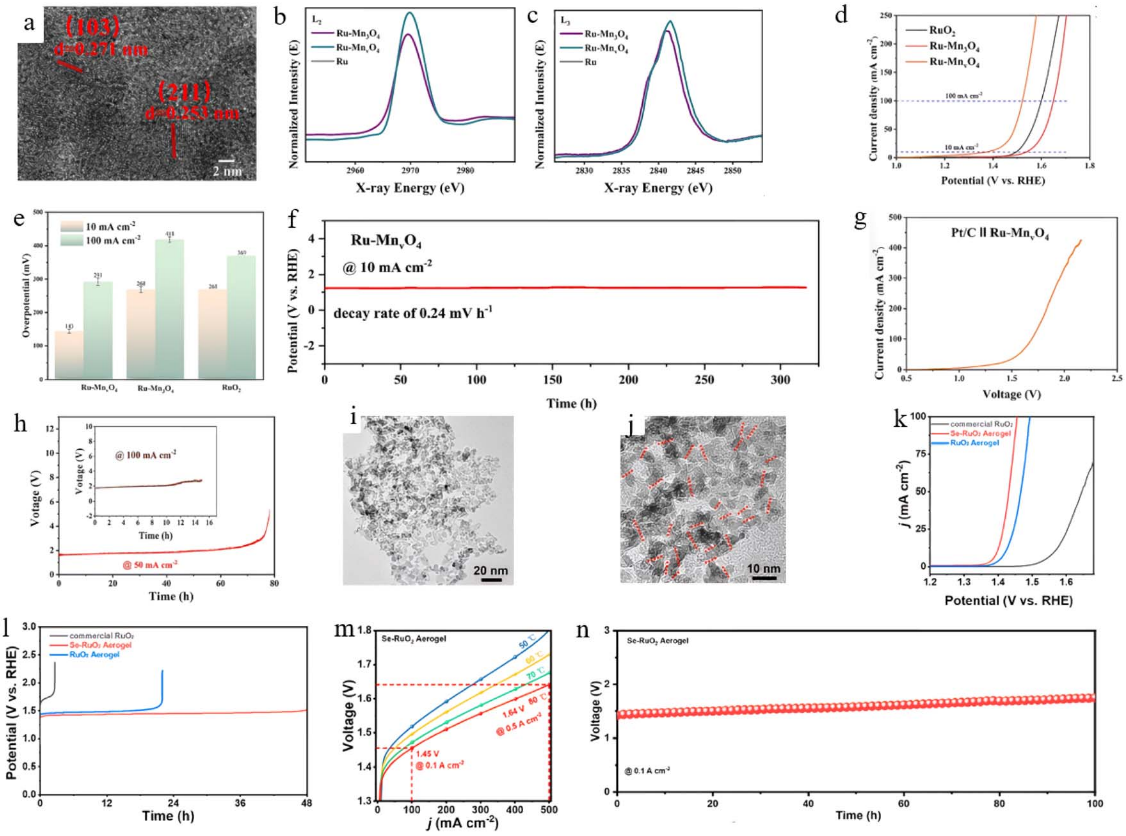

Fig. 16 (a) HRTEM image of Ru-Mn_VO_4. (b and c) Ru L_2-edge and L_3-edge XAS spectra of Ru-Mn_3O_4 and Ru-Mn_VO_4. (d) LSV curves. (e) Overpotential comparison. (f) $V-t$ stability curve of Ru-Mn_VO_4. (g) LSV curve of PEMWE. (h) $V-t$ stability curves of PEMWE.[165] Copyright 2025 Academic Press Inc. (i and j) TEM images of Se-RuO_2 aerogel. (k) OER polarization curves. (l) $V-t$ stability test curves. (m) PEMWE polarization curve with Se-RuO_2 aerogel as anode. (n) $V-t$ stability test curve of Se-RuO_2 aerogel-based PEMWE.[166] Copyright 2024 American Chemical Society.

only 2.42 wt% of low ruthenium loading, the introduction of anion and cation defects modulated the electronic structure of the material while concurrently increased the density of reaction sites (Fig. 15c and d). The optimized catalyst achieves 181 mV overpotential in acidic OER, and can maintain stable operation at 120 hours (Fig. 15e and f). Cheng *et al.* successfully constructed a B-intercalated 1T-phase-rich defective structure in MoS_2 *via* molten salt annealing, synthesizing the IrO_x@-MoB_5S_{2-x} catalyst (Fig. 15g and h).[164] The introduced defects optimized the material's electronic structure and simultaneously provided abundant active sites for anchoring IrO_x clusters (Fig. 15i and j), enabling it to exhibit an excellent overpotential of 168 mV in acidic OER (Fig. 15k).

Zhang and colleagues constructed single-atom Ru sites stabilized on a manganese-deficient Mn_VO_4 substrate (Ru-Mn_VO_4) *via* defect engineering strategy (Fig. 16a), which exhibited excellent catalytic performance in acidic OER.[165] It was found that the presence of manganese vacancies not only reduced the electron occupancy of the Ru antibonding orbitals but also shifted the d-band center further from the Fermi level, thereby weakening the interaction between the Ru site and the O–O* intermediate, promoting efficient O_2 desorption (Fig. 16b and c). In addition, this catalyst follows a lower-energy OPM pathway during the reaction, enabling an overpotential of 143 mV and stability for to 300 h (Fig. 16e and f). Furthermore, it showed superior performance in PEMWE testing, requiring 1.84 V to achieve 200 mA cm^{-2} (Fig. 16g), and maintaining stable operation for 60 hours without appreciable loss in performance (Fig. 16h). Jin *et al.* developed a Se-RuO_2 aerogel through defect engineering, achieving superior acidic OER performance.[166] The rich defect structure optimized the material's electronic properties, resulting in an overpotential of 166 mV while operating stability for 48 h (Fig. 16k and l). When integrated as the anode in a PEM electrolytic cell, it required 1.45 V to reach 0.1 A cm^{-2} (Fig. 16m), demonstrating excellent electrolysis performance. Moreover, it could stably operate for 100 hours (Fig. 16n).

Zhang's group successfully synthesized ultra-small IrO_2 nanoparticles rich in grain boundary defects.[167] Studies show that these controllable grain boundary defects effectively modulated the surface electronic configuration of Ir, resulting in moderate adsorption energy toward intermediates and significantly optimizing reaction kinetics. Theoretical calculations further confirmed that grain boundaries serve as active defect sites, improving the intrinsic activity of the material while simultaneously improving structural stability. Benefiting from this, the prepared 350-IrO_2 catalyst achieved 246 mV overpotential in acidic OER and could stably work for 200 hours.

When employed in a water electrolysis device, it exhibited highly efficient and stable hydrogen production performance even at 1 A cm^{-2}, exhibiting the crucial role of defect engineering in enhancing the overall performance. However, defect sites serve as preferential targets for acidic corrosion, exhibiting dissolution rates far exceeding those of perfect lattice sites. High concentrations of defects not only disrupt the crystal structure and create corrosion channels, leading to the overall pulverization of the catalyst, but also excessively elevate the O 2p energy level *via* oxygen vacancies, thereby accelerating lattice oxygen loss. Furthermore, defects undergo irreversible filling and evolution during the reaction, causing a rapid decay in their regulatory effects.

4.1.3. Strain engineering. Strain engineering is one of the key approaches to modulate catalytic performance, can effectively regulate the intrinsic electronic and interfacial properties of materials by applying tensile or compressive strain at the atomic scale.[168] In acidic OER environments, strain engineering mainly adjusts the d-band center of metal atoms through modifying the bond length and coordination environment, thereby modulating the binding energy of key intermediates.[169] Specifically, compressive strain typically induces lattice contraction, shortening the interatomic distance and increasing the d-orbital overlap. Conversely, tensile strain leads to lattice expansion, increasing the interatomic distance, reducing d-orbital overlap, and reducing the adsorption strength.[170,171] Such strain effects improve the intrinsic activity of catalysts and affect structural stability by altering the coordination environment of surface atoms.[172] By precisely controlling the type and degree of strain, it is possible to maintain catalyst stability while achieving precise electronic control at active sites, significantly improving catalytic performance.[173] It should be noted that strain engineering often works synergistically with other strategies such as defect engineering and doping to construct highly efficient catalytic systems. For example, Chang *et al.* successfully constructed IrBa-Co_3O_4 catalyst using electrodeposition technique.[174] The synergistic effect between the low iridium loading of 1.5 at% and Ba-doping induced compressive strain led to excellent catalytic performance. In electrolytic cell, the catalyst achieved an overpotential of 249 mV (Fig. 17a), and it could stably operate for 100 hours at 1.5 V (Fig. 17b). Through research, it was found that the superior performance mainly originated from the introduction of Ba, which not only effectively inhibited the aggregation of Ir atoms but also induced compressive strain in the lattice, manifested as lattice contraction and shortening of Co–O bonds (Fig. 17d). Electronic structure analysis further revealed that this strain facilitated electron transfer from Ir to Co/Ba, enhancing the valence state of Ir and optimizing its d-band center position (Fig. 17c). Xia *et al.* successfully synthesized a Ru/RuS_2/RuO_2 catalyst featuring a large surface area and a porous structure with controllable lattice strain *via in situ* combustion synthesis (Fig. 17e).[175] Research has shown that the strain effect generated by abundant multiphase interfaces

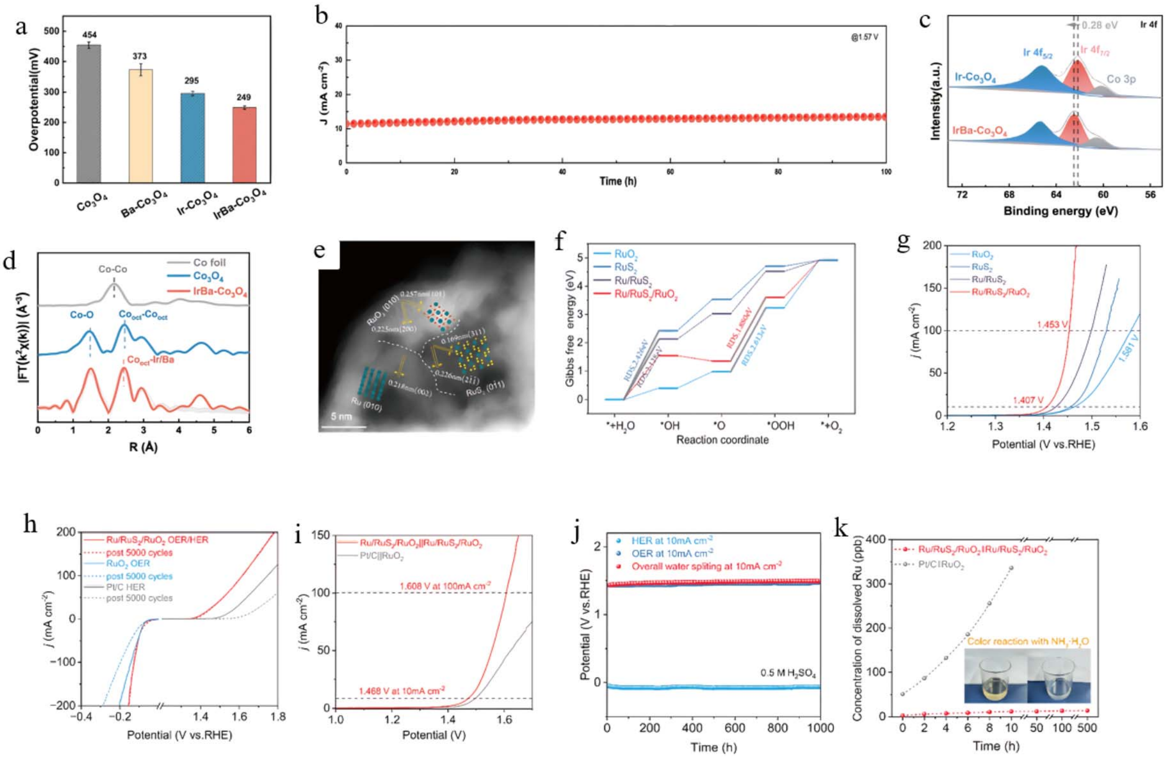

Fig. 17 (a) Overpotential histogram. (b) *I*–*t* stability test curve of IrBa-Co_3O_4‖Pt/C system. (c) XPS spectra of Ir 4f for IrBa-Co_3O_4 and Ir-Co_3O_4. (d) Fourier transform spectra of Co K-edge EXAFS.[174] Copyright 2025 Elsevier. (e) HAADF-STEM image of Ru/RuS_2/RuO_2. (f) ΔG of OER. (g) LSV curves. (h) OER and HER polarization curves after accelerated degradation test. (i) LSV curves. (j) *V*–*t* stability curves. (k) Ru dissolution concentration *versus* electrolysis time curve.[175] Copyright 2025 American Chemical Society.

effectively modulates the electronic structure of materials and markedly enhances the hydrophilicity and charge transport efficiency of the catalyst. Theoretical calculations further indicated that strain-induced shortening of Ru–O/Ru–S bonds and reduction in band gap energy are key factors in enhancing activity and durability, as they lower the activation energy barrier while increasing the desorption energy of Ru species (Fig. 17f). This catalyst exhibited an overpotential of a mere 177 mV (Fig. 17g), and maintained stable performance after 5000 cycles (Fig. 17h). Moreover, it demonstrated good catalytic performance and stability in full water-splitting devices, delivering a voltage of 1.468 V at 10 mA cm^{-2} (Fig. 17j), and stable operation for 1000 hours (Fig. 17n). After continuous operation for 500 hours, only 14 ppb of Ru dissolution was detected (Fig. 17k).

Li and coworkers constructed an atomically dispersed Ru single-atom catalyst (Ru$_1$-Pt$_3$Cu) on a PtCu alloy support *via* strain engineering strategies.[176] They found that the compressive strain in the Pt$_{skin}$ layer modulated the electronic configuration of the Ru active sites, modifying their adsorption strength toward intermediates. This strain effect exhibits a volcano-type relationship between lattice constant and OER activity, where the optimal Ru$_1$-Pt$_3$Cu catalyst shows 220 mV overpotential in 0.1 M HClO$_4$, with a service life one order of magnitude longer than RuO$_2$. Theoretical calculations indicated that compressive strain improves the activity of Ru sites while markedly enhancing their resistance to oxidation and dissolution, resulting in excellent activity and good stability. Su's group constructed a Ni-doped IrO$_2$ catalyst by constructing a synergistic system of compressive strain and oxygen vacancies, which demonstrated outstanding performance in acidic OER.[177] The catalyst achieved stable operation for 500 hours in PEMWE tests. Ni doping not only induced lattice compressive strain to enhance Ir–O covalency, but also generated oxygen vacancies that optimized water molecule adsorption and activation. The synergy between these two effects broke through the limitations of traditional reaction pathways, leading to notable enhancement of catalytic activity. Zhou and colleagues successfully introduced tensile strain into the RuO$_2$ lattice using oxidized graphene confinement method, significantly enhancing its OER performance.[178] Theoretical calculations revealed that tensile strain modulated the binding energy of intermediates and enhanced the material stability. The catalyst demonstrated an overpotential of 136 mV in acidic media and maintained stable operation for 160 hours. In PEMWE testing, it achieved stable operation for 120 hours under 0.2 A cm^{-2} conditions, demonstrating great potential for electrocatalytic applications. Strain is inherently a metastable lattice deformation that undergoes rapid relaxation under high-temperature and high-potential operating conditions, leading to an irreversible decay of its regulatory effect.[179] Excessive compressive strain can induce lattice distortion, while tensile strain lowers the dissolution potential of active metals, both scenarios exacerbate structural instability.[180] Furthermore, the strain effect is often coupled with doping and interfacial effects, which make it difficult to precisely decouple the structure–activity relationship.[181] Therefore, this strategy is only applicable to core–shell or epitaxial single-crystal systems capable of locking in the strain, and the strain magnitude must be strictly confined within an appropriate range. In industrial operating conditions, it should serve merely as an auxiliary optimization tool.

4.1.4. Interface engineering. As a pivotal methodology in catalyst design, interface engineering is an effective strategy to achieve dual improvement in catalyst activity and stability by constructing heterogeneous structures to induce electronic interactions and interfacial effects.[182] In acidic OER, this strategy primarily improves catalytic activity and stability through promoting charge transfer, optimizing intermediate adsorption energy, and enhancing structural stability. Wang *et al.* reported a controllable synthesis method to introduce metallic Ru into RuO$_2$, constructing a Ru^{4+}–O–Ru^0 interfacial structure.[183] This structure not only reduces the oxidation state of Ru^{4+} but also promotes deprotonation kinetics. Acting as an electron donor, metallic Ru lowers the oxidation state of the *Vo-RuO$_4$$^{2-}$ species and stabilizes the *Vo-RuO$_4$$^{2-}$-Ru/RuO$_2$ configuration, thereby enhancing the stability of acidic OER. Meanwhile, the interfacial oxygen sites between Ru^{4+} and Ru^0 significantly boost deprotonation kinetics, improving acidic OER activity. When two different materials form a heterojunction, spontaneous charge rearrangement and electron transfer occur at the interface, effectively modulating the electronic configuration of metal centers and optimizing their adsorption energy for the key intermediates.[184,185] Moreover, stable chemical bonding can be formed at the interface, avoiding the dissolution and aggregation of active components.[186] Therefore, rationally designed interface structures can optimize reaction pathways, diminish the activation energy, and boost catalyst performance. Xu *et al.* successfully improved the OER performance by constructing an IrO$_x$/WO$_3$ heterostructure.[187] Studies showed that the interfacial interaction between IrO$_x$ and WO$_3$ induced electron redistribution, optimized the immediate atomic environment around Ir centers, and simultaneously promoted the electronic synergy between metal and support. This interfacial modulation enabled the catalyst to achieve 260 mV overpotential (Fig. 18c), exhibiting mass activity of 176.8 A g^{-1} (Fig. 18b) and stable operation exceeding 100 hours (Fig. 18d), demonstrating its excellent activity and durability. The team of Wang developed a Co/CoO@PNC composite catalyst *via* interface engineering, which exhibited good overall performance in acidic OER, achieving an overpotential of 232 mV (Fig. 18f) while maintaining excellent stability over 100 hours (Fig. 18g).[188] The exceptional performance originates from the synergistic effect of Co/CoO heterojunction and P, N co-doped carbon substrate. The heterojunction enhances the charge transfer efficiency of the material, while heteroatom doping further optimizes the electronic configuration of the interface (Fig. 18h). The combined effects of these two factors promote the activity and durability of the catalyst.

Liu and coworkers successfully constructed a Mn-RuO$_2$/CeO$_2$ heterojunction catalyst *via* interfacial engineering, achieving the co-enhancement of activity and durability.[149] It demonstrates 227 mV overpotential in 0.1 M HClO$_4$ and can operate for 300 h. Studies showed that the electronic coupling effect formed

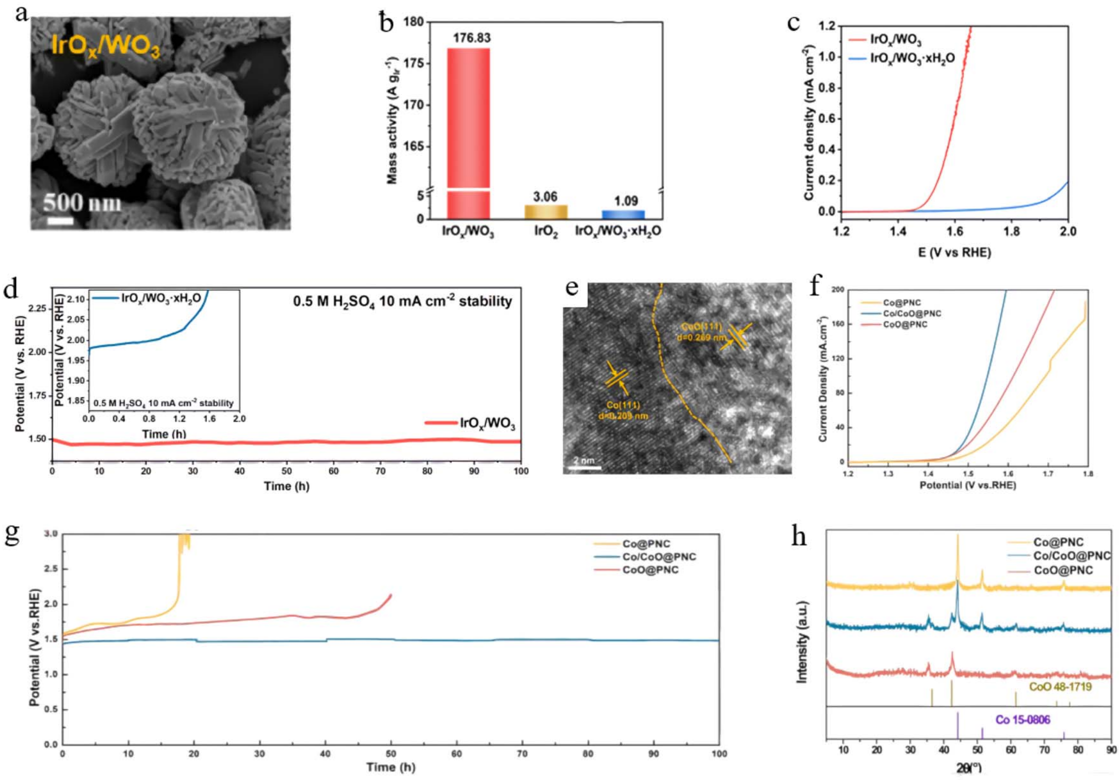

Fig. 18 (a) SEM images of IrO_x/WO_3. (b) Comparison chart of mass activity. (c) LSV curves. (d) V–t curve of IrO_x/WO_3.[187] Copyright 2024 Royal Society of Chemistry. (e) HRTEM image of Co/CoO@PNC. (f) LSV curves. (g) V–t stability curves. (h) X-ray diffraction (XRD) patterns.[188] Copyright 2025 Elsevier BV.

at the interface promotes electron transfer from CeO_2 to RuO_2, effectively enhancing the proportion of high-valence Ru species and optimizing their d-band center positions. Meanwhile, Mn species at the interface suppress the dissolution of Ru active sites and consumption of lattice oxygen through preferential oxidation and electronic modulation, thereby enhancing stability. Dai *et al.* innovatively employed molten salt-mediated interfacial engineering to construct a N-doped Ti–Ru rutile-type solid solution (M-TiRu4) (Fig. 19a and b).[189] It was found that the molten $NaNO_3$ medium not only promoted the low-temperature transformation of TiN into rutile-type TiO_2, but more importantly, utilized the lattice templating effect of RuO_2 nanoparticles to enable interfacial ion migration, forming a uniform solid solution with rich lattice heterogeneity (Fig. 19c–e). This unique interfacial engineering design enabled stable lattice doping of nitrogen and precise regulation of the electronic structure (Fig. 19f), significantly enhancing the material's conductivity. The optimized M-$TiRu_4$ catalyst achieves 194 mV overpotential and exceptional stability exceeding 600 hours in acidic OER (Fig. 19g and h), with Ru mass activity reaching 13.8 times that of commercial RuO_2 (Fig. 19i). In PEMWE testing, it achieves 2 A cm^{-2} at 1.64 V and operates stably for 200 hours under a constant load of 500 mA cm^{-2} (Fig. 19j and k).

Song and coworkers constructed a $RuO_2/CoFe_2O_4$ catalyst based on interface engineering strategies, which shows exceptional performance in the acidic OER.[190] This catalyst achieved 10 mA cm^{-2} with only 191 mV overpotential and demonstrated stability exceeding 100 hours. Studies showed that the closely integrated interface structure between RuO_2 and $CoFe_2O_4$ effectively promotes directional charge transfer, significantly enhancing catalytic reaction kinetics. Meanwhile, it enables the catalyst to maintain an intact crystal structure and morphology under harsh acidic conditions, providing a crucial guarantee for achieving highly efficient and stable electrocatalytic performance. However, chemical bond cleavage and phase segregation tend to occur readily at heterogeneous interfaces, leading to a complete structural collapse. Therefore, this strategy prioritizes dual-oxide systems to stabilize heterojunctions and strictly prohibits the use of carbon-based supports.

4.2. Geometric structure regulation

By employing strategies such as morphology regulation and carrier design to control the geometric structure of catalytic materials, not only can the mass transfer efficiency of reactions be significantly optimized and the timely detachment of oxygen bubbles be promoted, but also the dissolution of active components in catalytic materials can be inhibited, ultimately achieving synergistic improvement in catalyst activity and durability.[32]

4.2.1. Morphology control. Morphology control is crucial for enhancing the performance of acidic OER catalysts, as it can optimize mass transport pathways and interfacial reaction

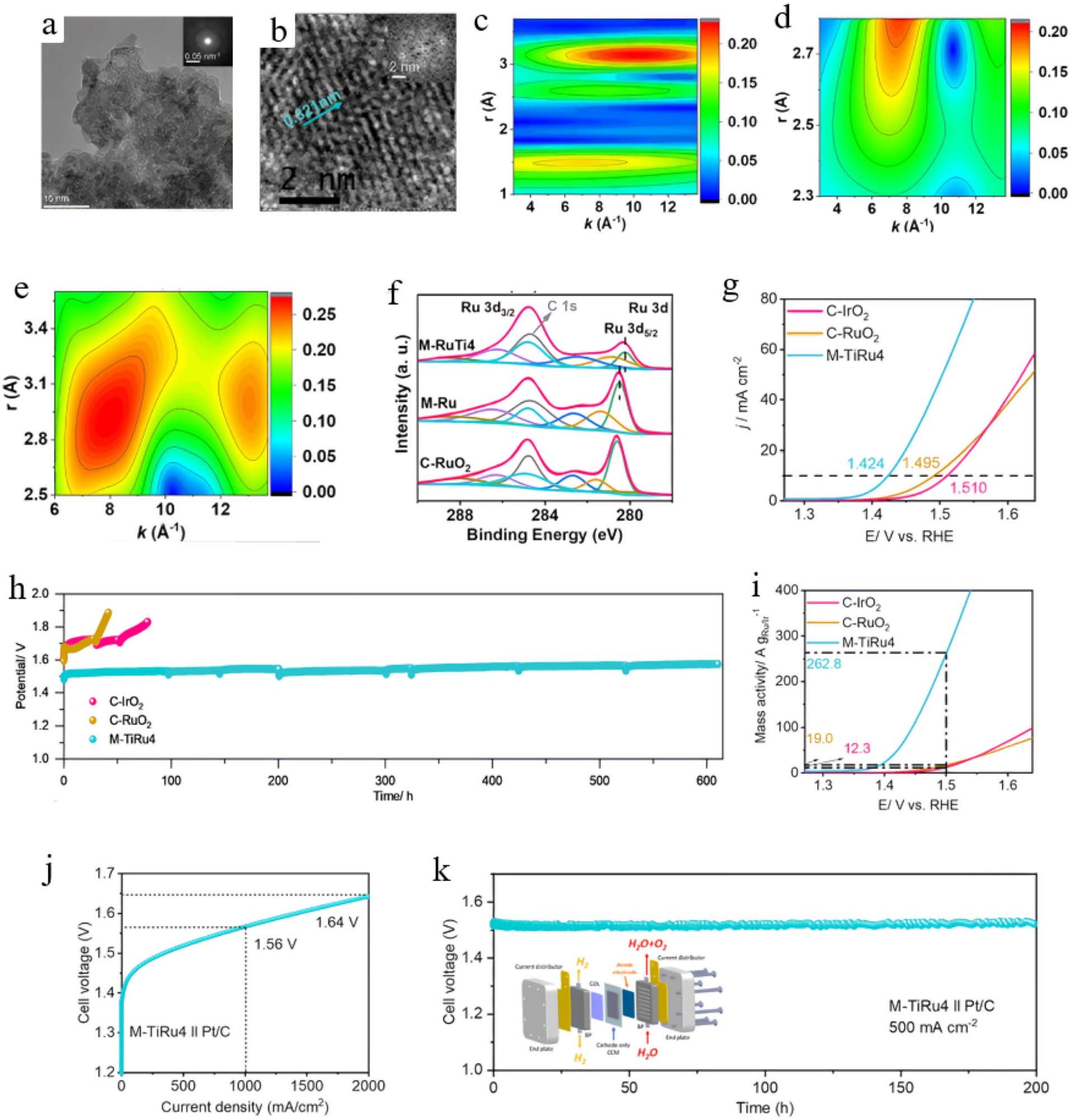

Fig. 19 (a) TEM image and (b) HRTEM image of M-TiRu$_4$. (c–e) WT-EXAFS spectra of M-TiRu$_4$. (f) Ru 3d XPS spectra. (g) LSV curves. (h) V–t stability test curves. (i) Mass activity plots. (j) PEMWE polarization curve with M-TiRu4 as anode. (k) Durability test curve of PEMWE at 500 mA cm^{-2}.[189] Copyright 2025 John Wiley and Sons Ltd.

environments. When catalysts are designed with specific nanostructures such as nanowires, nanorods, nanoclusters, and core–shell structures, they both enrich the population of active sites and create efficient mass transport channels alongside stable reaction interfaces.[191] Specifically, core–shell structures or hollow porous frameworks can effectively alleviate the volume changes of catalytic materials during cycling, providing physical barriers for active components, reducing direct corrosion by acidic electrolytes, and thus significantly extending their service life.[192] It should be noted that the selective exposure of different crystal facets can alter the arrangement and coordination environment of surface atoms, thereby affecting the selectivity of active sites. Through precise morphology control, materials can achieve both high catalytic activity and significantly improved durability, providing important technical support for developing high-performance acidic OER catalysts suitable for practical electrolytic cell systems.[193] Luo *et al.* successfully transformed an unstable Ir single-atom/$LiCoO_2$ system into a stable structure consisting of IrO_x nanoparticles supported on Co_3O_4 *via* a precise morphological reconstruction strategy (Fig. 20a).[194] During this transformation, unique geometric configurations formed between

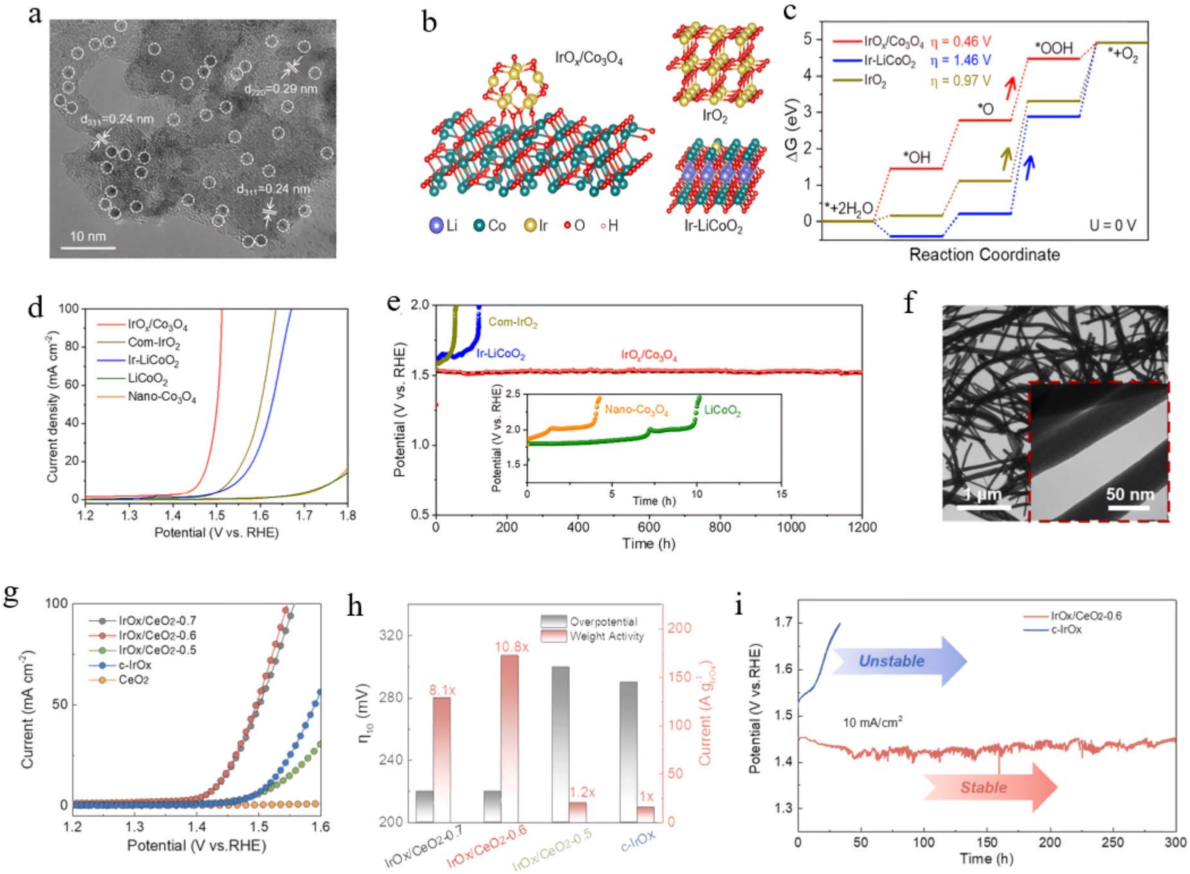

Fig. 20 (a) HRTEM image of IrO_x/Co_3O_4. (b) Atom structure models of catalyst surfaces. (c) ΔG for the OER process. (d) LSV curves. (e) *V–t* curves.[194] Copyright 2026 Wiley-VCH Verlag. (f) TEM image of IrO_x/CeO_2-0.6 nanowires. (g) LSV curves. (h) Mass activity comparison of Ir. (i) *V–t* curves.[195] Copyright 2022 Elsevier BV.

IrO_x nanoparticles and the Co_3O_4 support significantly improved charge transfer efficiency while effectively suppressed leaching of the Ir active component through spatial confinement effects (Fig. 20b). The synergistic effect induced by morphological reconstruction notably enhanced the overall performance of the catalyst, enabling it to exhibit 233 mV overpotential and ultra-long-term stability operation for 1200 hours in acidic OER (Fig. 20d and e). Qu's team successfully developed an amorphous IrO_x/CeO_2 nanowire catalyst with a unique nanowire morphology (Fig. 20f).[195] The rich interface formed by its special morphology synergizes with the electron buffering effect of CeO_2, which modulates the reaction pathway and effectively enhances the material's stability. This catalyst achieves breakthrough performance in acidic OER, with an overpotential of merely 220 mV, a mass activity of up to 167 A g^{-1} (Fig. 20h), and continuous stable operation for 300 hours (Fig. 20i).

Qin's group successfully constructed K-IrO_x/Ir catalyst with a unique core–shell structure by introducing the alkali metal K.[196] It shows an overpotential of 199 mV and an exceptional stability of up to 3000 hours in acidic OER. Studies have shown that the core–shell morphology of this catalyst markedly modulates the electronic properties of the Ir–O bonds, optimizing the adsorption strength of key intermediates. Meanwhile, the geometric confinement effect and electronic synergy arising from the core–shell structure jointly suppress the over-oxidation and dissolution of the Ir. This design allows the catalyst to maintain stability during prolonged operation, achieving a dual breakthrough in its activity and stability. Tan and colleagues prepared a nano-mesoporous structured $Pd_{50}Ir_{50}$ bifunctional catalyst.[103] Its unique nanoporous structure significantly increases active sites and effectively improves mass transport pathways. In acidic OER, this catalyst achieves an overpotential of 217 mV. For overall water splitting, it also exhibits outstanding performance. Feng *et al.* successfully fabricated vertically aligned graphene nanosheets arrays.[197] This unique array structure demonstrates an overpotential of 334 mV, outperforming commercial Ir/C catalysts. Studies have found that the vertically aligned nanosheet configuration significantly enhances the exposure of active sites while forms an efficient three-dimensional electron transport network. While high-specific-surface-area nanostructures can enhance initial activity, they significantly increase the contact area with acidic electrolytes, thereby accelerating metal dissolution and structural fragmentation. At high current densities, vigorous oxygen evolution tends to induce the detachment of nanostructures and the clogging of porous channels, leading to active site deactivation and severe concentration polarization.

This strategy of precisely controlling the spatial arrangement of nanoscale structures combined with surface chemistry opens new avenues for designing high-performance catalysts.

4.2.2. Carrier design. Carriers not only provide physical support in catalysts but also achieve synergistic optimization through multiple interactions with active components. Ideal carriers need to have efficient electron transport efficiency, stable chemical properties, and controllable surface states to ensure the stable operation of catalysts in harsh acidic media.[198] Carriers can stabilize active components through geometric effects, and their surface defects and specific crystal planes can provide precise anchoring sites for active substances, effectively inhibiting the migration, agglomeration, or dissolution of nanoparticles.[199] Current carrier design has evolved from traditional single-functional support materials to sophisticated systems with hierarchical pore structures, controllable surface chemistry, and specific crystal orientations. These new carriers effectively improve the utilization efficiency of active components and significantly enhance reaction kinetics by optimizing mass transport pathways and reducing interfacial resistance.[200,201] Therefore, reasonable carrier design can comprehensively improve catalyst activity, stability, and electrical conductivity. The team of Liu successfully constructed a high-performance Ir single-atom catalyst by anchoring Ir on the surface of a polyimide support (Fig. 21a).[202] The interaction between the active and support sites enhanced the mass activity of the catalyst in acidic OER by up to 49.7 times, exhibiting an overpotential of 254 mV (Fig. 21b), while maintaining stable operation for 360 hours with almost no performance degradation. Studies indicated that the distinctive architecture of the polyimide support effectively decreases the kinetic barrier of the rate-determining step and enhances the density of states of the Ir 5d orbitals through electronic modulation (Fig. 21c), thereby promoting the concerted transfer of protons and electrons, optimizing the binding energy of intermediates, and effectively promoting the overall reaction kinetics. The Andersen team successfully developed high-performance Ir-based OER catalysts by designing ATO2 carriers with high electrical conductivity (Fig. 21d).[203] Studies have shown that the lower oxygen content on the surface of ATO2 carriers enables high electrical conductivity, and the formed "Ir core–oxide shell" structure significantly enhances OER activity. The Ir single-atom catalyst supported on highly conductive ATO2 carrier exhibits excellent acidic OER activity with a mass activity of 777 A g^{-1}, surpassing commercial catalysts by a factor of 2.5 (Fig. 21f).

Park and colleagues markedly enhanced the acidic OER performance of IrO_x catalysts by constructing a SnO_2–rGO composite support.[204] Studies have found that when SnO_2 and rGO in the support are composited at a mass ratio of 80 : 20 ($IrO_x/S_{80}G_{20}$), the catalyst exhibits top-tier performance. Its mass activity reaches a value ten times that of commercial IrO_2. The outstanding performance of this catalyst stems from two key factors: on one hand, the abundant nanoparticle anchoring sites provided by SnO_2, and on the other hand, the highly efficient electron conduction network constructed by rGO. The synergistic effect of these components increases the active surface area of the catalyst while facilitates the formation of Ir^{3+} and oxygen vacancies. These structural traits are key drivers behind the observed enhancement in catalyst performance. Han *et al.* designed a nanostructured β-MnO_2 support, significantly boosting the performance of the catalyst.[205] The unique nanorod morphology (30–60 nm) of this support effectively dispersed noble metals, enabling the catalyst to exhibit an overpotential of 215 mV in 0.1 M $HClO_4$. They further

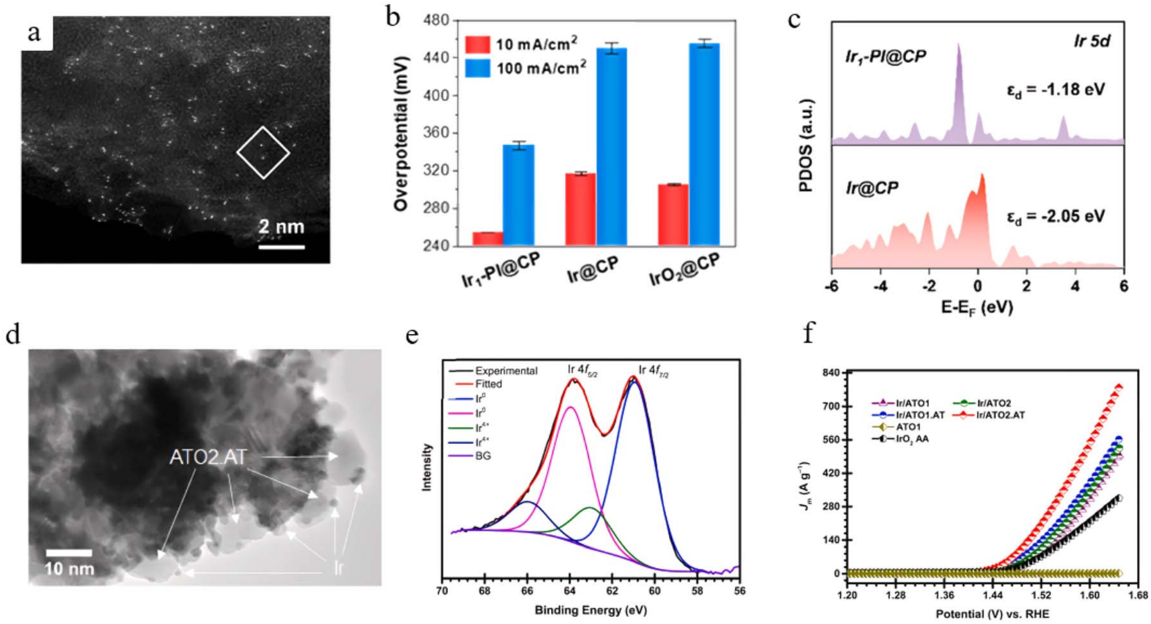

Fig. 21 (a) HAADF-STEM image of Ir_1-PI@CP. (b) Overpotential comparison. (c) Projected density of states (PDOS) of Ir atoms in the Ir_1/PI@CP and Ir@CP models.[202] Copyright 2024 American Chemical Society. (d) TEM image of Ir NPs loaded on ATO2.AT. (e) Ir 4f XPS spectrum of Ir/ATO2.AT. (f) Mass activity plot.[203] Copyright 2023 Elsevier BV.

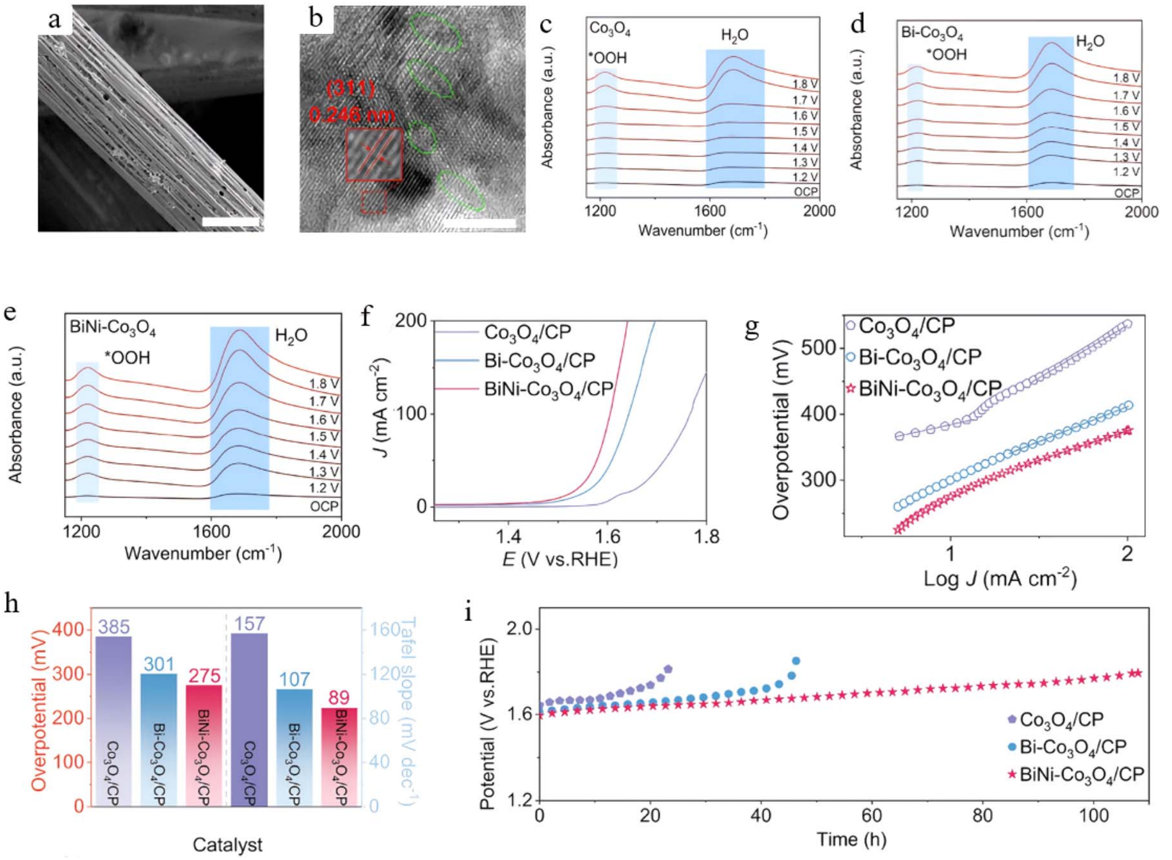

Fig. 22 (a) SEM image of BiNi-Co_3O_4/CP. (b) HRTEM image of BiNi-Co_3O_4/CP. *In situ* diffuse reflectance infrared Fourier transform spectroscopy (DRIFTS) spectra of (c) Co_3O_4/CP, (d) Bi-Co_3O_4/CP and (e) BiNi-Co_3O_4/CP. (f) LSV curves. (g) Tafel diagram. (h) Overpotentials and Tafel slopes. (i) Stability test curves.[208] Copyright 2025 American Chemical Society.

introduced Ti into β-MnO_2 to form a $Mn_{1-x}Ti_xO_2$ support, which significantly enhanced material stability under acidic conditions, allowing stable operation for 12 hours. Cho's group successfully constructed the IrO_x/Zr_2ON_2 electrocatalyst based on a Zr_2ON_2 support.[206] This support exhibits excellent conductivity and good stability, forming a strong interaction with the IrO_x active component, resulting in an overpotential of 255 mV in acidic OER, maintaining stable operation for 50 h. Mechanistic studies reveal that the Zr_2ON_2 support induces a reduction in the valence state of Ir and an elongation of the Ir–O bond distance. This structural modulation promotes a shift in the reaction pathway from AEM to LOM, thus achieving a dual enhancement in both activity and durability. Carbon-based supports suffer from severe electrochemical oxidation corrosion under high anodic potentials, leading to structural collapse and the detachment of active components. Meanwhile, oxide supports such as TiO_2 and SnO_2 suffer from inherently poor electrical conductivity. Therefore, priority should be given to highly conductive doped-oxide composite supports, and anti-passivation modification strategies must be incorporated for industrial operating conditions.[207]

It is particularly worth emphasizing that in the design of catalysts, a single tuning strategy often struggles to simultaneously meet the dual demands of activity and stability, while the synergistic effects of multiple strategies are becoming essential in addressing the limitations in catalyst stability and activity. By synergistically applying strategies including doping engineering, interface engineering, and morphology design in catalyst development, it is expected to achieve the transition of catalysts from laboratory research to industrial-scale production. Liu *et al.* successfully constructed a Bi/Ni co-doped Co_3O_4 catalyst using a one-step molten salt method (Fig. 22a).[208] They found that Bi doping could generate abundant lattice defects on the Co_3O_4 surface (Fig. 22b), appropriately regulating the electronic configuration of Co, while the introduction of Ni synergized with Bi to jointly promote the construction of a porous carbon-supported architecture. The dual-strategy synergy not only boosted active site density and facilitated bubble detachment, but also optimized the reaction pathway by lowering the OOH* intermediate formation energy and the interfacial water adsorption energy (Fig. 22e). Ultimately, the BiNi-Co_3O_4/CP catalyst designed through the synergistic integration of lattice defects and support modification achieved a small overpotential of 275 mV and stable operation for 110 hours during acidic OER processes (Fig. 22h and i).

Fu's group successfully constructed an amorphous/crystalline heterostructured FePb-doped RuO_2 catalyst, achieving synergistic enhancement through co-doping and

Table 2 Summary of representative OER electrocatalysts and their catalytic performance

Catalyst	η_{10} (mV)	Mass activity	Stable decay rate	Tafel slope (mV dec^{-1})	Dominant mechanism
Fe-RuO$_x$	191	—	0.07 mV h^{-1}	—	AEM
Ce-IrO$_2$	240	—	50 h stability	57	—
RuO$_2$/D-Co$_3$O$_4$/CC	181	—	120 h stability	76.5	—
IrO$_x$@MoB$_x$S$_{2-x}$-80	168	148.8 A mg$_{\mathrm{Ir}}$$^{-1}$	140 min stability	117.98	LOM
Ru-Mn$_4$O$_4$	143	3450 A g^{-1}	0.24 mV h^{-1}	57.22	OPM
350-IrO$_2$	246	0.61 A mg$_{\mathrm{Ir}}$$^{-1}$	0.059 mV h^{-1}	49.51	AEM
IrBa-Co$_3$O$_4$	249	—	100 h stability	65.28	AEM
Ru/RuS$_2$/RuO$_2$	177	—	1000 h stability	—	AEM
s-RuO$_2$	136	—	160 h stability	—	AEM
M-TiRu$_4$	194	262.8 A g$_{\mathrm{Ru}}$$^{-1}$	0.02 mV h^{-1}	69.5	—
RFC (RuO$_2$/CoFe$_2$O$_4$)	191	—	100 h stability	74.8	—
IrO$_2$/CeO$_2$-0.6	220	167 A g$_{\mathrm{Ir}}$$^{-1}$	300 h stability	63	AEM
K-IrO$_x$/Ir	199	—	0.0117 mV h^{-1}	—	AEM

interface engineering.[209] Studies show that Fe doping is able to modulate the electronic configuration of Ru sites, weakening the binding energy of the OOH* intermediate, while Pb doping can elevate the activation energy required for Ru reconstruction, collectively enhancing the OER activity and stability. Due to dual-doping with heteroatoms and heterogeneous structures, the synthesized FePb-RuO$_2$ exhibited an overpotential of 194 mV. In PEMWE measurement, an electrolyzer based on FePb-RuO$_2$ needed just 1.59 V to reach 500 mA cm^{-2}. This multi-strategy synergistic design concept promotes simultaneous improvement of catalyst performance and durability in severe acidic environments, while it paves the way for industrial applications (Table 2).

5. Application in PEMWE

5.1. Factors affecting the performance of PEMWE

PEMWE technology represents a cornerstone of the modern hydrogen energy sector owing to its green characteristics and high efficiency. The core component of this system is the membrane electrode assembly (MEA), composed of a PEM plus catalytic layers on both sides, forming a solid–liquid–gas three-phase reaction interface.[210] Currently, widely employed PEMs include perfluorosulfonic acid membranes and short-side-chain perfluorosulfonic acid resin membranes, which can effectively isolate anode and cathode gases while conducting protons.[211] Presently, the anode typically uses IrO$_2$-based catalysts for OER catalysis, while the cathode uses Pt/C materials for HER catalysis. The two materials can simultaneously maintain high activity and stability in acidic environments.

PEMWE technology faces multiple performance degradation problems during practical application, and these challenges are found across multiple dimensions, including materials, components and systems, which seriously affect its large-scale application. In terms of operation parameter regulation, although increasing the temperature can optimize the reaction kinetics and material transfer efficiency, exceeding 80 °C will trigger PEM dehydration and accelerated degradation of the material. Increasing the system pressure, although it helps bubble management and facilitates the direct storage of hydrogen, will exacerbate the risk of gas cross-penetration and even the formation of explosive mixtures.[212–215] At the material level, catalyst stability is the core issue. Dissolution of precious metals, active site reconfiguration, and nanoparticle agglomeration all lead to continuous degradation of performance, and the degradation of anode catalysts is particularly prominent in acidic environments.[216] In the MEA, the ionomer content needs to be precisely balanced, with too low a level restricting proton conduction and too high a level hindering gas transport, while bubble blockage and mechanical damage within the catalyst layer significantly cut down the utilization efficiency of the active interface.[217,218] System contamination should not be overlooked, as metal cationic impurities can occupy the sulfonic acid groups in the proton exchange membrane, dramatically increasing the resistance to proton transport, and dissolved metal species can redeposit and poison the cathodic active sites.[219] With respect to substrate materials, titanium-based porous transport layers are corrosion-resistant but susceptible to passivation, leading to increased contact resistance, while carbon-based materials are thermodynamically unstable and susceptible to corrosion at anodic potentials.[220] In addition, the interfacial stability between components is also a weak point, and adhesion failure between the membrane and catalytic layer, aging of the sealing structure, and hydrogen embrittlement of titanium will all affect the system lifetime.[221] These multi-dimensional and cross-scale decay mechanisms are coupled with each other, and together they constrain the commercialization of PEMWE technology. Therefore, a breakthrough needs to be achieved through the synergistic development of material innovation, structure optimization and system control.

5.2. Utilization of acidic OER catalysts under high current densities

Investigating the stable operation of acid OER catalysts at high-current-density is one of the core links in promoting the industrialization of PEMWE technology. Industrial-grade electrolytic cells typically need to operate continuously at current densities exceeding 1 A cm^{-2}, which poses extremely high requirements for catalyst durability. Moreover, the high potential and strong acidic environment accelerate the dissolution of active components and the corrosion of carrier materials, and the violently evolving oxygen bubbles also pose a threat to the electrode structure.[222] In addition, insufficient mass transport efficiency at high current densities will worsen the local reaction environment deterioration, further exacerbating catalyst performance degradation.[223] To overcome these bottlenecks, synergistic optimization must be achieved in catalyst electronic structure, interfacial stability, and macrostructural design, posing new challenges to both material design theory and preparation processes.

After continuous research, significant breakthroughs have been made in designing catalysts capable of stable operation within PEMWE systems. As an illustration, Wu *et al.* successfully constructed a La-doped RuO_2 nanorod composite catalyst on a titanium mesh using low-temperature thermal decomposition technology (Fig. 23a).[224] This catalyst displays strong catalytic performance under high-current-density operating conditions, with an overpotential of just 162 mV (Fig. 23b), and can operate stably for 450 hours in this operational environment at 100 mA cm^{-2} (Fig. 23c). The creation of the localized La–O–Ru structure effectively modulates the adsorption behavior of reaction intermediates while inhibiting Ru leaching and lattice oxygen depletion. In PEMWE testing, this catalyst required only 1.815 V under an industrial-grade current density of 1.0 A cm^{-2} and can continuously operate for over 120 h at 60 °C (Fig. 23e and f), indicating its great viability for practical implementation. Kang *et al.* developed IrRu ultrathin nanowires, which showed excellent comprehensive performance in acidic OER and actual PEMWE devices.[225] This catalyst necessitated merely 243 mV overpotential when operating, markedly outperforming IrO_2 (Fig. 23g). Electrolytic cell based on IrRu nanowires exhibited a 17.6% higher current density than commercial IrO_2 and Pt/C systems at 2 V (Fig. 23h). Notably, this electrolytic cell can stably operate for over 500 hours at 1.0 and 1.5 A cm^{-2}, featuring an ultra-low decay rate of merely 28 μV h^{-1} (Fig. 23i), demonstrating excellent prospects for industrial application.

Lu and coworkers engineered a catalyst containing Ru–B–Cr structural units in RuO_2 nanofibers through a synergistic Cr and B co-doping strategy.[226] Theoretical calculations indicated that this structural unit simultaneously regulates the adsorption energy of H* and the formation energy of OOH*, effectively prevents lattice oxygen involvement through the AEM pathway, and averting over-oxidation of Ru catalytic sites. This enables the catalyst to demonstrate excellent catalytic performance at industrial-level current densities, needing just 379 mV of overpotential to achieve 1 A cm^{-2} in acidic OER while realizing stable operation for 188 hours at this current density with an extremely low decay rate. Kwon's team successfully prepared iridium nanodendrites (IrNDs) catalysts with mass transport enhanced (MTE) using the solvothermal method.[227] In PEMWE testing, the MTE IrND/ATO catalyst exhibited excellent high-current-density performance, showing a 10% reduction in transport overpotential compared to Conv. IrND/ATO at 3 A cm^{-2}, and sustained steady operation for 12 days at 2 A cm^{-2}, exhibiting just 24 mV of voltage degradation. The $IrRuO_x$ alloy catalyst developed by Wang *et al.* achieved breakthrough progress under industrial-level operating conditions.[228] This

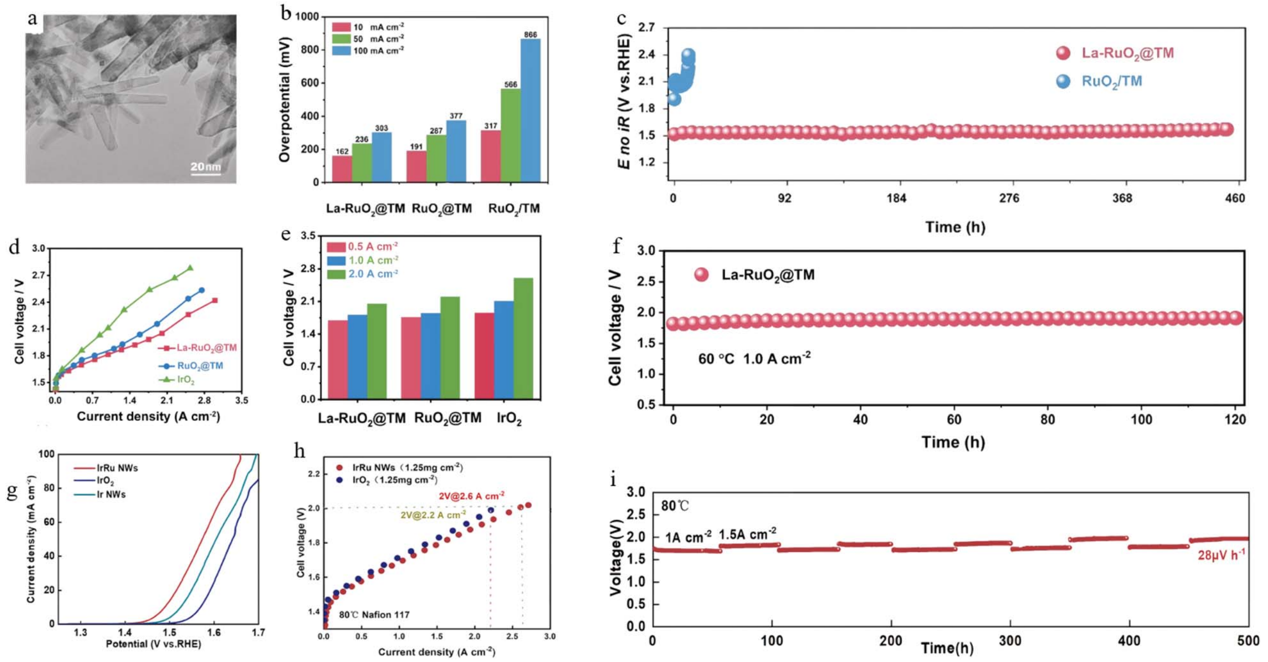

Fig. 23 (a) TEM image of La-RuO_2@TM. (b) Comparison of overpotentials. (c) Long-term operational stability curve. (d) *I*–*V* curves of PEM electrolyzer using of La-RuO_2@TM and IrO_2 as anodic catalyst without IR correction. (e) Cell voltage comparison across varied current densities. (f) *V*–*t* curve of La-RuO_2@TM in a PEM electrolytic cell at 60 °C and 1.0 A cm^{-2}.[224] Copyright 2025 John Wiley and Sons Ltd. (g) LSV curves of IrRu NWs and comparative catalysts. (h) Polarization curve of PEMWE device. (i) Stress stability test curve of PEMWE device.[225] Copyright 2024 Wiley-VCH Verlag.

material demonstrated ultra-long stable operation capability of up to 1600 hours at 2 A cm^{-2}, surpassing all similar catalysts in durability. Analysis showed that the atomic-level synergistic effect between Ir and Ru enhanced the stability of Ru–O bonds, effectively inhibiting the leaching of active components and structural damage of the catalytic layer, providing an effective solution to address the durability challenges of PEMWE technology in practical applications. Sohn *et al.* successfully fabricated CoFeNiMoWTe high-entropy catalysts featuring an amorphous porous architecture through a hierarchical hybrid method combining electrochemical deposition and tellurization processes.[14] The unique nanosheet array structure of this material provides abundant active sites, while the doping of Te raises the metal valence state, thus substantially tuning the material's electronic configuration. It demonstrates an overpotential of 373 mV and stable operation capability of 100 hours in acidic OER. In PEMWE testing, this catalyst necessitated merely 1.81 V of voltage at 1 A cm^{-2} (70 °C), while exhibiting a mere 30 mV voltage decay after 100 hours of continuous operation.

6. Challenges and prospects

Through a systematic analysis of acidic OER catalysts from reaction mechanisms to performance optimization strategies, a relatively complete theoretical framework has been established in this field, especially in PEMWE technology oriented towards practical applications. Researchers have developed a series of catalysts that perform excellently at high current densities through multi-element synergistic strategies. However, when comparing laboratory performance indicators with industrial requirements, significant technological gaps are found. Issues such as long-term operational stability of catalysts, effective reduction of precious metal loading, and performance degradation under actual operating conditions have not been fundamentally resolved. This paper conducts a thorough examination of the present major research bottlenecks and provides systematic prospects for future development directions.

(1) The trade-off dilemma of activity *versus* structural robustness. Achieving synergistic improvement in both activity and stability of OER catalysts in acidic condition has been a core challenge in this field. Catalytic materials usually undergo dynamic restructuring in the course of the reaction, a process that can trigger the formation of active sites and cause structural collapse.[229] Studies have shown that enhancing metal–oxygen bonds can improve catalyst stability to a certain degree, yet this is often achieved at the expense of compromising their inherent activity, while optimizing intermediate adsorption energy can enhance activity but may also accelerate catalyst deactivation.[230] To break through this bottleneck, it is essential to construct catalytic sites with both stability and activity through precise regulation of electronic structure.

(2) The rarity and cost-related challenges of noble metals. Ir and other elements, despite being the most potential noble metals for acidic OER catalysis, have extremely low natural abundances that restrict the large-scale advancement of PEMWE. Designing single-atom catalysts to achieve atomic-level dispersion and maximize atom utilization efficiency has become a pivotal strategy to mitigate the shortage of noble metals. However, under acidic condition and high potential, single atoms are prone to agglomeration and dissolution. Therefore, constructing functional supports with anchoring sites or rationally modulating the metal–support interaction could boost the stability of these catalysts.

(3) The gap between laboratory and industrialization. From laboratory research to industrial application is a long-term technological challenge. At the material preparation level, common laboratory synthesis techniques such as hydrothermal method and electrodeposition struggle to satisfy the demands of large-scale production and cost control in industrial settings. In terms of performance evaluation, traditional testing methods based on rotating disk electrodes cannot accurately reflect the mass transfer conditions and current distribution characteristics in actual devices. More importantly, in device environments, catalytic performance is influenced by a variety of parameters including ionomer coverage and interface contact, which cannot be fully simulated in conventional three-electrode systems. In addition, dynamic operating conditions in actual operation, such as temperature fluctuations and pressure changes, can have decisive impacts on catalyst lifespan. Therefore, establishing testing standards and evaluation systems that closely resemble actual operating conditions has become the key to catalyst transition from laboratory to industrial applications.

(4) Development of novel catalyst systems. Future catalyst development should break through the limitations of traditional material systems and explore novel material systems including high-entropy alloys (HEA) and metal–organic frameworks. HEA, endowed with their synergistic effects of multiple components and unique local environments, are expected to significantly enhance structural stability while maintaining high activity. Moreover, developing molecular catalysts with well-defined structures, combined with support stabilization strategies, opens up new pathways for precise design and regulation of active sites.

(5) Multi-dimensional synergistic design. The future catalyst design should establish a multilevel synergistic framework from atomic scale to macroscopic devices. At the atomic level, the inherent activity of active sites can be enhanced *via* the accurate modulation of their coordination configurations and electronic architectures. On the nanoscale, both the active site density and mass transport efficiency are amenable to optimization through morphological regulation and interface engineering. At the macroscale level, the efficient transport of reactants and products can be achieved through electrode structure design and device optimization. This cross-scale synergistic design requires the deep integration of multiple disciplines to establish an accurate mapping from microstructure to macroscopic performance.

(6) Applications of artificial intelligence (AI) and ML. AI and ML technologies are gradually becoming the key driving force for catalyst development. By constructing large-scale material genome databases and applying deep learning algorithms, the

relationship between material composition, structure and performance can be effectively analysed, thus realizing efficient screening and rational design of new catalysts. ML can also be used to analyse complex *in situ* characterization data, revealing the dynamic evolution mechanism of catalysts in the working state. Meanwhile, AI techniques can optimize synthesis path parameters and predict the long-term evolutionary behaviour of materials under different test states, accelerating the research and development process. The successful application of these technologies relies on the accumulation of high-quality data and synergistic innovation in multiple fields, and is expected to bring breakthrough changes to catalyst research.

Author contributions

All of the authors contributed to the literature search, writing and editing of this review.

Conflicts of interest

There are no conflicts to declare.

Data availability

No primary research results, software or code has been included and no new data were generated or analysed as part of this review.

Acknowledgements

This work was supported by the National Natural Science Foundation of China (No. 92580106), and the Education Department of Jilin Province (No. JJKH20261306KJ).

Notes and references

1 X. Xu and J. Guan, *Adv. Funct. Mater.*, 2025, **35**, 2505823.

2 Z. Shang, X. Feng, G. Chen, R. Qin and Y. Han, *Small*, 2023, **19**, 2304975.

3 Q. Lu, Z. Wang and J. Guan, *Adv. Funct. Mater.*, 2026, **36**, e13188.

4 N. Du, C. Roy, R. Peach, M. Turnbull, S. Thiele and C. Bock, *Chem. Rev.*, 2022, **122**, 11830–11895.

5 M. Faizan, H. Bibi, E. Aamir, R. Saeed, T. S. Kiong and H. Song, *Renew. Sustain. Energy Rev.*, 2025, **212**, 115385.

6 Y. Lin, Y. Dong, X. Wang and L. Chen, *Adv. Mater.*, 2023, **35**, 2210565.

7 S. Zhang, W. Ruan and J. Guan, *Adv. Energy Mater.*, 2025, **15**, 2404057.

8 J. Kibsgaard and I. Chorkendorff, *Nat. Energy*, 2019, **4**, 430–433.

9 H. Li, R. Jia, W. Chen, C. Wei, Q. Ji, X. Long, B. Wang, K. Zhang, J. Feng and L. Tan, *Adv. Funct. Mater.*, 2025, **35**, e12051.

10 Y. Meng, Q. Sun, T. Zhang, J. Zhang, Z. Dong, Y. Ma, Z. Wu, H. Wang, X. Bao, Q. Sun and J. Yu, *J. Am. Chem. Soc.*, 2023, **145**, 5486–5495.

11 Z. Jiang, S. Song, X. Zheng, X. Liang, Z. Li, H. Gu, Z. Li, Y. Wang, S. Liu, W. Chen, D. Wang and Y. Li, *J. Am. Chem. Soc.*, 2022, **144**, 19619–19626.

12 M. Vanags, G. Kulikovskis, J. Kostjukovs, L. Jekabsons, A. Sarakovskis, K. Smits, L. Bikse and A. Šutka, *Energy Environ. Sci.*, 2022, **15**, 2021–2028.

13 L. Chong, G. Gao, J. Wen, H. Li, H. Xu, Z. Green, J. D. Sugar, A. J. Kropf, W. Xu, X.-M. Lin, H. Xu, L.-W. Wang and D.-J. Liu, *Science*, 2023, **380**, 609–616.

14 S. Jo, M.-C. Kim, K. B. Lee, H. Choi, L. Zhang and J. I. Sohn, *Adv. Energy Mater.*, 2023, **13**, 2301420.

15 R. Ram, L. Xia, H. Benzidi, A. Guha, V. Golovanova, A. Garzón Manjón, D. Llorens Rauret, P. Sanz Berman, M. Dimitropoulos, B. Mundet, E. Pastor, V. Celorrio, C. A. Mesa, A. M. Das, A. Pinilla-Sánchez, S. Giménez, J. Arbiol, N. López and F. P. García de Arquer, *Science*, 2024, **384**, 1373–1380.

16 N. Zeng, C. Hu, C. Lv, A. Liu, L. Hu, Y. An, P. Li, M. Chen, X. Zhang, M. Wen, K. Chen, Y. Yao, J. Cai and T. Tang, *Sep. Purif. Technol.*, 2023, **310**, 123148.

17 J. Du, D. Xiang, K. Zhou, L. Wang, J. Yu, H. Xia, L. Zhao, H. Liu and W. Zhou, *Nano Energy*, 2022, **104**, 107875.

18 L. Li, P. Wang, Q. Shao and X. Huang, *Adv. Mater.*, 2021, **33**, 2004243.

19 Y. Duan, Z.-Y. Yu, S.-J. Hu, X.-S. Zheng, C.-T. Zhang, H.-H. Ding, B.-C. Hu, Q.-Q. Fu, Z.-L. Yu, X. Zheng, J.-F. Zhu, M.-R. Gao and S.-H. Yu, *Angew. Chem., Int. Ed.*, 2019, **58**, 15772–15777.

20 R. Qin, G. Chen, X. Feng, J. Weng and Y. Han, *Adv. Sci.*, 2024, **11**, 2309364.

21 H. Yoon, B. Ju and D.-W. Kim, *Battery Energy*, 2023, **2**, 20230017.

22 H. Li, Y. Lin, J. Duan, Q. Wen, Y. Liu and T. Zhai, *Chem. Soc. Rev.*, 2024, **53**, 10709–10740.

23 S. Lyu, C. Guo, J. Wang, Z. Li, B. Yang, L. Lei, L. Wang, J. Xiao, T. Zhang and Y. Hou, *Nat. Commun.*, 2022, **13**, 6171.

24 L. Wang, L. Shi, Q. Liu, Y. Huang, W. Yan, X. Liang, X. Zhao, H. Chen and X. Zou, *ACS Catal.*, 2023, **13**, 7322–7330.

25 Y. Wen, P. Chen, L. Wang, S. Li, Z. Wang, J. Abed, X. Mao, Y. Min, C. T. Dinh, P. D. Luna, R. Huang, L. Zhang, L. Wang, L. Wang, R. J. Nielsen, H. Li, T. Zhuang, C. Ke, O. Voznyy, Y. Hu, Y. Li, W. A. Goddard Iii, B. Zhang, H. Peng and E. H. Sargent, *J. Am. Chem. Soc.*, 2021, **143**, 6482–6490.

26 F. Yang, Y. Luo, Q. Yu, Z. Zhang, S. Zhang, Z. Liu, W. Ren, H.-M. Cheng, J. Li and B. Liu, *Adv. Funct. Mater.*, 2021, **31**, 2010367.

27 Y. Cheng, H. Guo, L. Zhang, M. Wang, J. Zhou, T. Qian and C. Yan, *Adv. Funct. Mater.*, 2023, **33**, 2208718.

28 P. Zhai, Y. Zhang, Y. Wu, J. Gao, B. Zhang, S. Cao, Y. Zhang, Z. Li, L. Sun and J. Hou, *Nat. Commun.*, 2020, **11**, 5462.

29 J. Han, J. Sun, S. Chen, S. Zhang, L. Qi, A. Husile and J. Guan, *Adv. Mater.*, 2024, **36**, 2408139.

30 Z. Liu, X. Wang, G. Xie and J. Ge, *Chem. Eng. J.*, 2024, **499**, 155901.

31 Q. Ma and S. Mu, *Interdiscip. Mater.*, 2023, **2**, 53–90.

32 C. Rong, K. Dastafkan, Y. Wang and C. Zhao, *Adv. Mater.*, 2023, **35**, 2211884.

33 Z. Zhang, P. Ma, C. Jia, W. Gao, M. Liu, K. N. Hui, M. Zuo, S. Zhou and J. Zeng, *eScience*, 2025, **5**, 100402.

34 C. Hu, Y. Hu, B. Zhang, H. Zhang, X. Bao, J. Zhang and P. Yuan, *Electrochem. Energy Rev.*, 2024, **7**, 19.

35 C. Rong, X. Huang, H. Arandiyan, Z. Shao, Y. Wang and Y. Chen, *Adv. Mater.*, 2025, **37**, 2416362.

36 L. Wu, Z. Guan, D. Guo, L. Yang, X. A. Chen and S. Wang, *Small*, 2023, **19**, 2304007.

37 J. Ying, J.-B. Chen, Y.-X. Xiao, S. I. Cordoba de Torresi, K. I. Ozoemena and X.-Y. Yang, *J. Mater. Chem. A*, 2023, **11**, 1634–1650.

38 Y. Wen, C. Liu, R. Huang, H. Zhang, X. Li, F. P. García de Arquer, Z. Liu, Y. Li and B. Zhang, *Nat. Commun.*, 2022, **13**, 4871.

39 C. Zhang, S. Qin, B. Li and P. Jin, *J. Mater. Chem. A*, 2022, **10**, 8309–8323.

40 S. Sen and T. K. Mandal, *ChemCatChem*, 2025, **17**, e00535.

41 J. Song, C. Wei, Z.-F. Huang, C. Liu, L. Zeng, X. Wang and Z. J. Xu, *Chem. Soc. Rev.*, 2020, **49**, 2196–2214.

42 H. Dau, C. Limberg, T. Reier, M. Risch, S. Roggan and P. Strasser, *ChemCatChem*, 2010, **2**, 724–761.

43 P. Ding, Y. Xue, Z. Chai, Q. Hu, C. Tong, G. Teobaldi and L.-M. Liu, *J. Phys. Chem. Lett.*, 2024, **15**, 2859–2866.

44 I. C. Man, H.-Y. Su, F. Calle-Vallejo, H. A. Hansen, J. I. Martínez, N. G. Inoglu, J. Kitchin, T. F. Jaramillo, J. K. Nørskov and J. Rossmeisl, *ChemCatChem*, 2011, **3**, 1159–1165.

45 Q. Liang, G. Brocks and A. Bieberle-Hütter, *J. Phys. Energy*, 2021, **3**, 026001.

46 J. Rossmeisl, A. Logadottir and J. K. Nørskov, *Chem. Phys.*, 2005, **319**, 178–184.

47 C. Sun, S. Zhang, P. Wang, M. Wei, S. Wang and X.-R. Shi, *J. Catal.*, 2024, **439**, 115773.

48 E. Fabbri, A. Habereder, K. Waltar, R. Kötz and T. J. Schmidt, *Catal. Sci. Technol.*, 2014, **4**, 3800–3821.

49 J. Wang, J. Bai, Y. Cang, Q. Li, X. Fan and H. Lin, *Catalysts*, 2023, **13**, 1378.

50 Y. Yue, X. Zhong, M. Sun, J. Du, W. Gao, W. Hu, C. Zhao, J. Li, B. Huang, Z. Li and C. Li, *Adv. Mater.*, 2025, **37**, 2418058.

51 H. Wu, Z. Fu, J. Chang, Z. Hu, J. Li, S. Wang, J. Yu, X. Yong, G. I. N. Waterhouse, Z. Tang, J. Chang and S. Lu, *Nat. Commun.*, 2025, **16**, 4482.

52 A. Grimaud, A. Demortière, M. Saubanère, W. Dachraoui, M. Duchamp, M.-L. Doublet and J.-M. Tarascon, *Nat. Energy*, 2016, **2**, 16189.

53 Q. Qi, S. Zhu, Z. Liu, C. Zhang and J. Hu, *J. Colloid Interface Sci.*, 2026, **701**, 138669.

54 K. A. Stoerzinger, R. R. Rao, X. R. Wang, W. T. Hong, C. M. Rouleau and Y. Shao-Horn, *Chem*, 2017, **2**, 668–675.

55 D. A. Kuznetsov, M. A. Naeem, P. V. Kumar, P. M. Abdala, A. Fedorov and C. R. Müller, *J. Am. Chem. Soc.*, 2020, **142**, 7883–7888.

56 N. Zhang and Y. Chai, *Energy Environ. Sci.*, 2021, **14**, 4647–4671.

57 P. Zhang, J. Wang, T. Yang, R. Wang, R. Shen, Z. Peng, Y. Liu, X. Wu, J. Jiang and B. Li, *Chin. J. Catal.*, 2025, **72**, 48–83.

58 J. Liu, T. Yang, L. Yang, G. Huang, E. Wang, K. Wang, H. Wang and X. Hou, *Surf. Interfaces*, 2025, **72**, 107169.

59 X. Tan, M. Zhang, D. Chen, W. Li, W. Gou, Y. Qu and Y. Ma, *Small*, 2023, **19**, 2303249.

60 S. Xin, Y. Tang, B. Jia, Z. Zhang, C. Li, R. Bao, C. Li, J. Yi, J. Wang and T. Ma, *Adv. Funct. Mater.*, 2023, **33**, 2305243.

61 K. Xiao, Y. Wang, P. Wu, L. Hou and Z.-Q. Liu, *Angew. Chem.*, 2023, **135**, e202301408.

62 Q. Deng, H. Li, K. Pei, L. W. Wong, X. Zheng, C. S. Tsang, H. Chen, W. Shen, T. H. Ly, J. Zhao and Q. Fu, *ACS Nano*, 2024, **18**, 33718–33728.

63 C.-J. Huang, H.-M. Xu, T.-Y. Shuai, Q.-N. Zhan, Z.-J. Zhang and G.-R. Li, *Appl. Catal. B Environ.*, 2023, **325**, 122313.

64 Z.-F. Huang, S. Xi, J. Song, S. Dou, X. Li, Y. Du, C. Diao, Z. J. Xu and X. Wang, *Nat. Commun.*, 2021, **12**, 3992.

65 G. Su, J. Yang and J. Yin, *Chemelectrochem*, 2025, **12**, e202400559.

66 J. S. Yoo, X. Rong, Y. Liu and A. M. Kolpak, *ACS Catal.*, 2018, **8**, 4628–4636.

67 X. Zhao, Y. Shao, J. Cai, X. Yue and S. Huang, *ACS Appl. Mater. Interfaces*, 2025, **17**, 36698–36705.

68 Q. Wu, K. Jiang, J. Han, D. Chen, M. Luo, J. Lan, M. Peng and Y. Tan, *Sci. China Mater.*, 2022, **65**, 1262–1268.

69 X. Zheng, J. Yang, X. Xu, S. Dou, W. Sun, D. Wang and G. Wang, *Adv. Energy Mater.*, 2024, **14**, 2401227.

70 X. Luo, H. Zhao, X. Tan, S. Lin, K. Yu, X. Mu, Z. Tao, P. Ji and S. Mu, *Nat. Commun.*, 2024, **15**, 8293.

71 H. Liu, Y. Zhang, Z. Liu, S. Wang, X. Mu, Q. Zhang, W. Cao, S. Liu, D. Wang and Z. Dai, *J. Am. Chem. Soc.*, 2025, **147**, 44141–44151.

72 J. Yang, S. Sang and M. Wang, *J. Energy Chem.*, 2026, **113**, 464–483.

73 J. Chang, Y. Shi, H. Wu, J. Yu, W. Jing, S. Wang, G. I. N. Waterhouse, Z. Tang and S. Lu, *J. Am. Chem. Soc.*, 2024, **146**, 12958–12968.

74 C. Lin, J.-L. Li, X. Li, S. Yang, W. Luo, Y. Zhang, S.-H. Kim, D.-H. Kim, S. S. Shinde, Y.-F. Li, Z.-P. Liu, Z. Jiang and J.-H. Lee, *Nat. Catal.*, 2021, **4**, 1012–1023.

75 Z.-H. Yin, H. Liu, J.-S. Hu and J.-J. Wang, *Natl. Sci. Rev.*, 2024, **11**, nwae362.

76 N. A. R. Che Mohamad, H. Lee, M. Gong, C. Ye, Y. Bu, Z. Lin, D.-i. Won, J. Kim, F. Marques Mota and D. H. Kim, *Small*, 2025, **21**, e08259.

77 C. Han, Y. Liu and T. Wang, *ACS Energy Lett.*, 2025, **10**, 4511–4517.

78 C. Hou, L. Xue, L. Zhou, C. Chen, X. Lv and J. Dang, *Acta Mater.*, 2025, **297**, 121361.

79 L. Liu, G. Wang, G. Wang, Y. Liu, K. Wang, X. Chen, L. Zhang, Q. Cai, S. Li, D. Liang, H. Cui, M. Li and X. Lv, *Coord. Chem. Rev.*, 2026, **548**, 217178.

80 Y. Mu, J. Fan, T. Gao, L. Wang, L. Zhang, X. Zou, W. Zheng, Y.-W. Zhang, Z. G. Yu and X. Cui, *Angew. Chem., Int. Ed.*, 2025, **64**, e202504876.

81 S. Liu, S. Wang, S. Liu, Z. Lin, J. Liu, F. Zeng, J. Hu, P. Zhang, Z. Cai, Y. Huang, T. Wang and Q. Li, *Angew. Chem., Int. Ed.*, 2026, **65**, e8854134.

82 J. Wan, F. Qian, W. Jiang, J. Huang, Y. Xin, C. Hu, C. Liu, R. Li, G. Wang, L. Yi, S. Chen, L. Song, Q. Chen and Y. Liu, *Appl. Catal. B Environ. Energy*, 2026, **392**, 126716.

83 K. Zhou, Y. Wang, Z. Jiang, B. Dai and Z.-J. Jiang, *Adv. Mater.*, 2025, **37**, 2420159.

84 Q. Ji, B. Tang, X. Zhang, C. Wang, H. Tan, J. Zhao, R. Liu, M. Sun, H. Liu, C. Jiang, J. Zeng, X. Cai and W. Yan, *Nat. Commun.*, 2024, **15**, 8089.

85 W. Gou, S. Zhang, Y. Wang, X. Tan, L. Liao, Z. Qi, M. Xie, Y. Ma, Y. Su and Y. Qu, *Energy Environ. Sci.*, 2024, **17**, 6755–6765.

86 W. Ko, J. Shim, H. Ahn, H. J. Kwon, K. Lee, Y. Jung, W. H. Antink, C. W. Lee, S. Heo, S. Lee, J. Jang, J. Kim, H. S. Lee, S.-P. Cho, B.-H. Lee, M. Kim, Y.-E. Sung and T. Hyeon, *J. Am. Chem. Soc.*, 2025, **147**, 2369–2379.

87 L. Qi, X. Bai, Y. Wang, Z. Duan, L. Li and J. Guan, *CCS Chem.*, 2025, **7**, 2508–2519.

88 P. Zhang, K. Chen, J. Li, M. Wang, M. Li, Y. Liu and Y. Pan, *Adv. Mater.*, 2023, **35**, 2303243.

89 L. Qi and J. Guan, *Adv. Funct. Mater.*, 2026, **36**, e27230.

90 Y. Liu, Y. Chen, X. Mu, Z. Wu, X. Jin, J. Li, Y. Xu, L. Yang, X. Xi, H. Jang, Z. Lei, Q. Liu, S. Jiao, P. Yan, X. Li and R. Cao, *ACS Catal.*, 2023, **13**, 3757–3767.

91 J. Rouger, S. Cavaliere and F. Jaouen, *Curr. Opin. Electrochem.*, 2025, **49**, 101606.

92 M.-Q. Yang, K.-L. Zhou, C. Wang, M.-C. Zhang, C.-H. Wang, X. Ke, G. Chen, H. Wang and R.-Z. Wang, *J. Mater. Chem. A*, 2022, **10**, 25692–25700.

93 B. Zaman, Q. Su, D. Jiao, M. Gong, M. Wang, M. Faizan and X. Cui, *Inorg. Chem. Front.*, 2025, **12**, 6792–6802.

94 Y. Xiang, H. Wang, S. Li, L. Li, J. Ren, G. Xing, L. Deng and S. Peng, *Inorg. Chem. Front.*, 2026, **13**, 1479–1487.

95 A. Kumar, M. Gil-Sepulcre, J. Lee, V. Q. Bui, Y. Wang, O. Rüdiger, M. G. Kim, S. DeBeer and H. Tüysüz, *Adv. Mater.*, 2024, **36**, 2401648.

96 L. Lin, Q. Fu, R. Wang, T. Yao, X. Wang and B. Song, *Adv. Energy Sustainability Res.*, 2023, **4**, 2300075.

97 D. Böhm, M. Beetz, M. Schuster, K. Peters, A. G. Hufnagel, M. Döblinger, B. Böller, T. Bein and D. Fattakhova-Rohlfing, *Adv. Funct. Mater.*, 2020, **30**, 1906670.

98 X. Chen, W. Li, N. Song, M. Zhong, S. Yan, J. Xu, W. Zhu, C. Wang and X. Lu, *Chem. Eng. J.*, 2022, **440**, 135851.

99 Y. Lin, B. Wu, A. Chen, J. Su and L. Chen, *Int. J. Hydrogen Energy*, 2023, **48**, 10368–10376.

100 X. Pan, S. Yu, J. Zhang, L. Zhang, L. Wang, H. Song, L. Du, S. Liao and Z. Cui, *Chem. Mater.*, 2023, **35**, 2559–2568.

101 Y. Yang, D. Chen, S. Hu, P. Pei and X. Xu, *Small*, 2025, **21**, 2410372.

102 X. Xiong, J. Tang, Y. Ji, W. Xue, H. Wang, C. Liu, H. Zeng, Y. Dai, H.-J. Peng, T. Zheng, C. Xia, X. Liu and Q. Jiang, *Adv. Energy Mater.*, 2024, **14**, 2304479.

103 J. Shi, C.-W. Kao, J. Lan, K. Jiang, M. Peng, M. Luo, Y.-R. Lu, S. Zhang and Y. Tan, *J. Mater. Chem. A*, 2023, **11**, 11526–11533.

104 F. Lv, J. Feng, K. Wang, Z. Dou, W. Zhang, J. Zhou, C. Yang, M. Luo, Y. Yang, Y. Li, P. Gao and S. Guo, *ACS Cent. Sci.*, 2018, **4**, 1244–1252.

105 N. Yu, Z.-J. Zhang, Y.-M. Chai and B. Dong, *Mater. Chem. Front.*, 2023, **7**, 4236–4258.

106 J.-W. Zhao, Z.-X. Shi, C.-F. Li, Q. Ren and G.-R. Li, *ACS Mater. Lett.*, 2021, **3**, 721–737.

107 L. Yang, G. Yu, X. Ai, W. Yan, H. Duan, W. Chen, X. Li, T. Wang, C. Zhang, X. Huang, J.-S. Chen and X. Zou, *Nat. Commun.*, 2018, **9**, 5236.

108 T. Xia, C. Liu, Y. Lu, W. Jiang, H. Li, Y. Ma, Y. Wu and G. Che, *Appl. Surf. Sci.*, 2022, **605**, 154727.

109 L. Wang, Y. Hao, S. Bi, S.-F. Hung, K.-S. Peng, H.-Y. Chen, T.-Y. Chen, Y. Zhang, G. Xing, L. Li, F. Hu, Y. Wu and S. Peng, *J. Am. Chem. Soc.*, 2026, **148**(20), 20731–20741.

110 Y. Zhou, Y. Mao, C. Ye, Z. Wang, S. Wei, J. V. Kennedy, Y. Zhao, H. Yang, B. C. C. Cowie and G. I. N. Waterhouse, *Adv. Energy Mater.*, 2025, **15**, 2500700.

111 L. Cao, Q. Luo, J. Chen, L. Wang, Y. Lin, H. Wang, X. Liu, X. Shen, W. Zhang, W. Liu, Z. Qi, Z. Jiang, J. Yang and T. Yao, *Nat. Commun.*, 2019, **10**, 4849.

112 N. Yao, H. Jia, J. Zhu, Z. Shi, H. Cong, J. Ge and W. Luo, *Chem*, 2023, **9**, 1882–1896.

113 T. Zhao, R. Du, Q. Fang, G. Hao, G. Liu, D. Zhong, J. Li and Q. Zhao, *Small*, 2025, **21**, 2410311.

114 Y. Yu, F. Liu, X. Liu, L. Li, B. Zhou, H. Liao, P. Tan and J. Pan, *Chem. Eng. J.*, 2025, **514**, 163295.

115 H. Cai, N. Jiang, L. Xiong, F. Shang, J. Hou, Y. Lin, C. Li, X. Zhang, D. Su and S. Yang, *Int. J. Hydrogen Energy*, 2024, **84**, 840–847.

116 T.-T. Yang, M. Wang, F.-F. Zhang, C. Xi, L. Xiao, X. Zhao, J. Wang, W. Hua, C.-K. Dong, H. Liu and X.-W. Du, *ACS Energy Lett.*, 2024, **9**, 3955–3961.

117 Z. Jiang, L. Shao, Y. Sun, Y. Dong, X. Zheng, T. Wang, J. Li, H. Shao, L. Jiao and Y. Deng, *Adv. Funct. Mater.*, 2025, **35**, e09656.

118 M. Retuerto, L. Pascual, F. Calle-Vallejo, P. Ferrer, D. Gianolio, A. G. Pereira, Á. García, J. Torrero, M. T. Fernández-Díaz, P. Bencok, M. A. Peña, J. L. G. Fierro and S. Rojas, *Nat. Commun.*, 2019, **10**, 2041.

119 I. Rodríguez-García, J. L. Gómez de la Fuente, D. Galyamin, Á. Tolosana-Moranchel, P. Kayser, M. A. Salam, J. A. Alonso, F. Calle-Vallejo, S. Rojas and M. Retuerto, *J. Mater. Chem. A*, 2024, **12**, 16854–16862.

120 A. L. Maulana, S. Han, Y. Shan, P.-C. Chen, C. Lizandara-Pueyo, S. De, K. Schierle-Arndt and P. Yang, *J. Am. Chem. Soc.*, 2025, **147**, 10268–10278.

121 L. Zhou, M. Yang, Y. Liu, F. Kang and R. Lv, *Nat. Commun.*, 2025, **16**, 8739.

122 J. Chen, Y. Ma, T. Huang, T. Jiang, S. Park, J. Xu, X. Wang, Q. Peng, S. Liu, G. Wang and W. Chen, *Adv. Mater.*, 2024, **36**, 2312369.

123 H. Guo, Z. Fang, H. Li, D. Fernandez, G. Henkelman, S. M. Humphrey and G. Yu, *ACS Nano*, 2019, **13**, 13225–13234.

124 J. Zhu, M. Xie, Z. Chen, Z. Lyu, M. Chi, W. Jin and Y. Xia, *Adv. Energy Mater.*, 2020, **10**, 1904114.

125 Z. Li, X. Wen, Y. Liu, X. Qi, Z. Wang and D. Wang, *J. Alloys Compd.*, 2025, **1039**, 183127.

126 B. Tamilarasi, K. P. Jithul and J. Pandey, *Int. J. Hydrogen Energy*, 2024, **58**, 556–582.

127 R.-Y. Fan, H.-Y. Zhao, Y.-N. Zhen, F.-G. Wang, H. Hu, Y.-M. Chai and B. Dong, *Fuel*, 2023, **333**, 126361.

128 V. Krishnan, P. Pazhamalai, V. Mohan, J. Chennakrishnan and S.-J. Kim, *Int. J. Hydrogen Energy*, 2025, **105**, 882–887.

129 J. Cao, D. Zhang, B. Ren, P. Song and W. Xu, *Energy Environ. Sci.*, 2024, **17**, 5911–5921.

130 B. Thomas, B. Peng, X. Huang and T. Asefa, *J. Mater. Chem. A*, 2024, **12**, 22528–22538.

131 Z. Zhao, B. Zhang, D. Fan, Y. Wang, H. Yang, K. Huang, X. Pan, R. Zhang, H. Tang and M. Lei, *J. Catal.*, 2022, **405**, 265–272.

132 W. Hou, X. Zhou, T. Cheng, H. Chi, Y. Zhang, C. Zhuang, Y. Zheng, X. Zhong, Z. Zou and Y. Zhou, *Nanoscale*, 2026, **18**, 5799–5804.

133 R. Su, R. Wang, H. Wang, Y. Liu, Y. Yan, H. Yin, Y. Kong, F. Shaik and B. Jiang, *Int. J. Hydrogen Energy*, 2025, **117**, 24–38.

134 M. Xu, S. Yang, L. Wang, H. Xu, W. Liu, Y. Su, Y. Huang, Z. Wang, L. Wang, X. Zheng, Y. Qin, F. Huo and X. Sheng, *Chem. Eng. J.*, 2025, **519**, 164994.

135 M. Feng, J. Huang, Y. Peng, C. Huang, X. Yue and S. Huang, *ACS Nano*, 2022, **16**, 13834–13844.

136 A. Wang, Q. Wang, Y. Dou, M. S. Sudi, W. Zhu, D. Shang and L. Li, *Dyes Pigm.*, 2022, **206**, 110620.

137 R. Santhosh Kumar, S. C. Karthikeyan, S. Ramakrishnan, S. Vijayapradeep, A. Rhan Kim, J.-S. Kim and D. Jin Yoo, *Chem. Eng. J.*, 2023, **451**, 138471.

138 S. R. Ede and Z. Luo, *J. Mater. Chem. A*, 2021, **9**, 20131–20163.

139 Y. Zheng, T. Zhou, Q. Zhang, H. Guo, J. Yang, B. Ding, H. Shao and X. Yang, *Sci. Technol. Adv. Mater.*, 2025, **26**, 2520159.

140 A. Maheen, S. A. Alsalhi, K. Tahir, A. Kumar, R. S. K. Sharma, P. K. Pathak, S. Saini, V. K. Pandey and R. Haldhar, *J. Sol. Gel Sci. Technol.*, 2025, **114**, 496–507.

141 Z.-Q. Chen, W.-J. Cai, H.-J. Zhang, K. Xiao, B. Huang and Z.-Q. Liu, *Chem. Sci.*, 2025, **16**, 14750–14759.

142 X. Li, G. Zhang, J. Nie, H. Chen, Z. Feng, F. Zheng, G. Wei, S. Shen, J. Cheng and J. Zhang, *Mater. Today Energy*, 2025, **48**, 101772.

143 K. Sathiyan, T. Mondal, P. Mukherjee, S. G. Patra, I. Pitussi, H. Kornweitz, R. Bar-Ziv and T. Zidki, *Nanoscale*, 2022, **14**, 16148–16155.

144 H. Sun and W. Jung, *J. Mater. Chem. A*, 2021, **9**, 15506–15521.

145 L. Xiao, X. Bai, J. Han, Z. Wang and J. Guan, *Chin. J. Catal.*, 2025, **71**, 340–352.

146 L. Kampermann, J. Klein, T. Wagner, A. Kotova, C. Placke-Yan, A. Yasar, L. Jacobse, S. Lasagna, C. Leppin, S. Schulz, J. Linnemann, A. Bergmann, B. R. Cuenya and G. Bacher, *ACS Catal.*, 2025, **15**, 18391–18403.

147 Y. Zhao, L. Li, Z. Wang, W. Li, Z. Han, Y. Cui, Z. Duan, W. Wang and X. Fu, *ACS Appl. Mater. Interfaces*, 2025, **17**, 49461–49471.

148 Z. Majie, W. Guoxiang, M. Qingwang, W. Hao, A. Boyan and G. Shuya, *J. Electroanal. Chem.*, 2024, **975**, 118650.

149 J. Li, Y. Liu, M. Yao, S. Geng and F. Liu, *Chem. Eng. J.*, 2025, **521**, 167203.

150 X. Ke, B. Dou, Y. Hua, J. Huang, Q. Dong and P. Liang, *Mater. Chem. Phys.*, 2026, **347**, 131443.

151 S. Wang, J. Zang, W. Shi, D. Zhou, Y. Jia, J. Wu, W. Yan, B. Zhang, L. Sun and K. Fan, *ACS Appl. Mater. Interfaces*, 2023, **15**, 59432–59443.

152 L. An, X. Cai, F. Yang, J. You, S. Yuan, L. Zhao, C. Zhao, L. Luo, X. Yan, S. Shen and J. Zhang, *Appl. Surf. Sci.*, 2024, **652**, 159251.

153 G. A. C. Ribeiro, S. L. S. de Lima, K. E. R. Santos, J. P. Mendonça, P. Macena, E. C. Pessanha, T. C. Cordeiro, J. Gardener, G. Solórzano, J. E. S. Fonsaca, S. H. Domingues, C. C. dos Santos, A. H. B. Dourado, A. A. Tanaka, A. G. M. da Silva and M. A. S. Garcia, *Discover Nano*, 2023, **18**, 147.

154 J. Zheng and Z. Wang, *Chem Catal.*, 2024, **4**, 101091.

155 X. Zheng, Y. Chen, W. Lai, P. Li, C. Ye, N. Liu, S. X. Dou, H. Pan and W. Sun, *Adv. Funct. Mater.*, 2022, **32**, 2200663.

156 J. Sun, Z. Wang and J. Guan, *Chem. Res. Chin. Univ.*, 2025, **41**, 666–686.

157 J. Sun, H. Xue, N. Guo, T. Song, Y.-R. Hao, J. Sun, J. Zhang and Q. Wang, *Angew. Chem., Int. Ed.*, 2021, **60**, 19435–19441.

158 D. Yan, C. Xia, W. Zhang, Q. Hu, C. He, B. Y. Xia and S. Wang, *Adv. Energy Mater.*, 2022, **12**, 2202317.

159 Q. He, L. Han, C. Lin and K. Tao, *Nanoscale*, 2024, **16**, 12368–12379.

160 R. Zhang, L. Wang, Y.-H. Ma, L. Pan, R. Gao, K. Li, X. Zhang and J.-J. Zou, *J. Mater. Chem. A*, 2019, **7**, 10010–10018.

161 S.-F. Li, J. Zheng and D. Yan, *Inorg. Chem.*, 2023, **62**, 11009–11015.

162 J. Zheng, D. Meng, J. Guo, A. Zhang and Z. Wang, *Small*, 2024, **20**, 2407177.

163 Y. Liu, Z. Yuan, Q. Song, T. Xu, G. He, H. Sun, Q. Qiao, X. Guan, T. Xu, X. Dai and X. Zhang, *Sci. China Mater.*, 2024, **67**, 771–779.

164 J. Huang, J. Nie, X. Li, L. Zou, Y. Wang, H. Chen, G. Wei and J. Cheng, *Langmuir*, 2024, **40**, 23951–23961.

165 L. Wang, D. Yang, Z. Yang and J. Zhang, *J. Colloid Interface Sci.*, 2025, **699**, 138233.

166 X. Han, M. Jin, T. Chen, T. Chou, J. Chen, S. Wang, Y. Yang, J. Wang and H. Jin, *ACS Mater. Lett.*, 2024, **6**, 748–755.

167 N. Zhang, Y. Fan, D. Wang, H. Yang, Y. Yu, J. Liu, J. Zeng, D. Bao, H. Zhong and X. Zhang, *Chem. – Eur. J.*, 2024, **30**, e202400651.

168 X. Yang, Y. Wang, X. Tong and N. Yang, *Adv. Energy Mater.*, 2022, **12**, 2102261.

169 H. Yu, G. Zhang, D. Zhang, R. Yang, X. Li, X. Zhang, G. Lian, H. Hou, Z. Guo, C. Hou, X. Yang and F. Dang, *Adv. Energy Mater.*, 2024, **14**, 2401509.

170 S. Maiti, K. Maiti, M. T. Curnan, K. Kim, K.-J. Noh and J. W. Han, *Energy Environ. Sci.*, 2021, **14**, 3717–3756.

171 D. Zhou, S. Wang, Y. Jia, X. Xiong, H. Yang, S. Liu, J. Tang, J. Zhang, D. Liu, L. Zheng, Y. Kuang, X. Sun and B. Liu, *Angew. Chem., Int. Ed.*, 2019, **58**, 736–740.

172 W. Sun, Z. Wang, W. Q. Zaman, Z. Zhou, L. Cao, X.-Q. Gong and J. Yang, *Chem. Commun.*, 2018, **54**, 996–999.

173 J. Qi, K. Zhu, W. Ma, H. Zhang, M. Feng and X. Zong, *Appl. Surf. Sci.*, 2026, **716**, 164700.

174 M. Huo, Q. Li, Y. Liang, W. Liu, H. Wang, K. Qin, X. Sun, Y. Ma, Z. Xing and J. Chang, *Chem. Eng. J.*, 2025, **519**, 165555.

175 X. Duan, N. Wen, S. Liu, H. Li, X. Jiao, D. Chen and Y. Xia, *ACS Catal.*, 2025, **15**, 10119–10129.

176 Y. Yao, S. Hu, W. Chen, Z.-Q. Huang, W. Wei, T. Yao, R. Liu, K. Zang, X. Wang, G. Wu, W. Yuan, T. Yuan, B. Zhu, W. Liu, Z. Li, D. He, Z. Xue, Y. Wang, X. Zheng, J. Dong, C.-R. Chang, Y. Chen, X. Hong, J. Luo, S. Wei, W.-X. Li, P. Strasser, Y. Wu and Y. Li, *Nat. Catal.*, 2019, **2**, 304–313.

177 M. Liu, X. Zhong, X. Chen, D. Wu, C. Yang, S. Li, C. Ni, Y. Chen, Q. Liu and H. Su, *Adv. Mater.*, 2025, **37**, 2501179.

178 S. Zhao, L. Wu, X. Miao, Y. Di, L. Shi and S. Zhou, *Nano Lett.*, 2025, **25**, 11142–11148.

179 P. Adiga, W. Nunn, C. Wong, A. K. Manjeshwar, S. Nair, B. Jalan and K. A. Stoerzinger, *Mater. Today Energy*, 2022, **28**, 101087.

180 J. Som, A. J. Reese, L. Mitrovic, R. S. Kim, S. McBride, S. S. Nalawade, S. Aravamudhan, G. Hautier, J. Yano, D. G. Schlom and J. Suntivich, *J. Am. Chem. Soc.*, 2025, **147**, 37115–37122.

181 X. Cao, L. Miao, W. Jia, H. Qin, G. Lin, R. Ma, T. Jin and L. Jiao, *Nat. Commun.*, 2025, **16**, 6217.

182 J. Jia, Y. Wang, Y. Cha, Z. Wang, J. Huang, D. Wang, H. Li, K. Guo, J. Li, J. Huang, Y. Tang and C. Xu, *Adv. Funct. Mater.*, 2025, **35**, 2500568.

183 Q. Lu, J. Liu, X. Zou, B. Huang, W. Wu, J. Yin, Z.-Q. Liu and Y. Wang, *Angew. Chem., Int. Ed.*, 2025, **64**, e202503733.

184 X. Dai, Y. Qian, Z. Xu, A. Xiong, X. Zhang, L. Chen and W. Li, *Nanoscale*, 2025, **17**, 23854–23882.

185 J. Li, Y. Wei, L. Zou, Y. Liu, S. Li and Y. Luo, *New J. Chem.*, 2025, **49**, 17577–17587.

186 G. Zhao, K. Rui, S. X. Dou and W. Sun, *J. Mater. Chem. A*, 2020, **8**, 6393–6405.

187 Z. Guan, Y. Weng, J. Li, S. Li, K. Wang, L. Lei, Y. Wang, L. Zhuang and Z. Xu, *New J. Chem.*, 2024, **48**, 2505–2514.

188 X. Li, S. Zhou, Y. Wu, K. Hu, F. Liu, X. Wang, J. Li, F. Pei, X. Chen and M. Wang, *J. Alloys Compd.*, 2025, **1020**, 179550.

189 F. Wang, W. Wang, T. Wang, X. Wang, K. M. Siniard, J. Fan, B. Bashir, A. S. Ivanov, X. Li, J. Li, G. Hu, F. Y. Zhang, G. Wang and S. Dai, *Angew. Chem., Int. Ed.*, 2025, **64**, e202514922.

190 M. Wei, L. Mu, Z. Liu, F. Gao, G. Song, Q. Si, M. Zhang, F. Dai, M. Zhang, R. Ding, L. Yang, Z. Gao and S. Song, *Catal. Sci. Technol.*, 2024, **14**, 6824–6832.

191 H. Chen, L. Shi, X. Liang, L. Wang, T. Asefa and X. Zou, *Angew. Chem., Int. Ed.*, 2020, **59**, 19654–19658.

192 Y. Lv, S. Duan, Y. Zhu, P. Yin and R. Wang, *Nanomaterials*, 2020, **10**, 611.

193 S. K. Ray and B. P. Bastakoti, *Int. J. Hydrogen Energy*, 2024, **51**, 1109–1118.

194 Y. Liu, H. Jang, X. Xi, Y. Zhong, R. Cao, S. Jiao, X. Li, Z. Lei and J.-L. Luo, *Adv. Funct. Mater.*, 2025, **36**, e15920.

195 W. Gou, Z. Xia, X. Tan, Q. Xue, F. Ye, S. Dai, M. Zhang, R. Si, Y. Zou, Y. Ma, J. C. Ho and Y. Qu, *Nano Energy*, 2022, **104**, 107960.

196 L. Wang, Z. Li, H. Jang, M. G. Kim, S. Liu, X. Wang, M. Zeng, J. Cho, X. Liu and Q. Qin, *Adv. Funct. Mater.*, 2025, **35**, 2421615.

197 C. Lei, Q. Zheng, F. Cheng, Y. Hou, B. Yang, Z. Li, Z. Wen, L. Lei, G. Chai and X. Feng, *Adv. Funct. Mater.*, 2020, **30**, 2003000.

198 L. Moriau, M. Bele, Ž. Marinko, F. Ruiz-Zepeda, G. Koderman Podboršek, M. Šala, A. K. Šurca, J. Kovač, I. Arčon, P. Jovanovič, N. Hodnik and L. Suhadolnik, *ACS Catal.*, 2021, **11**, 670–681.

199 B. R. Anne, J. Kundu, M. K. Kabiraz, J. Kim, D. Cho and S.-I. Choi, *Adv. Funct. Mater.*, 2023, **33**, 2306100.

200 L. Deng, S. Liu, D. Liu, Y.-M. Chang, L. Li, C. Li, Y. Sun, F. Hu, H.-Y. Chen, H. Pan and S. Peng, *Small*, 2023, **19**, 2302238.

201 T. Reier, H. N. Nong, D. Teschner, R. Schlögl and P. Strasser, *Adv. Energy Mater.*, 2017, **7**, 1601275.

202 L. Zhang, J. Bai, S. Zhang, Y. Liu, J. Ye, W. Fan, E. Debroye and T. Liu, *ACS Nano*, 2024, **18**, 22095–22103.

203 I. A. Khan, P. Morgen, S. Gyergyek, R. Sharma and S. M. Andersen, *Mater. Chem. Phys.*, 2023, **308**, 128192.

204 S. Lim, J. Cho and S. Park, *J. Electroanal. Chem.*, 2023, **928**, 116992.

205 N. Tursina, A. Gaur, M. S. Cho, M. Kim, K. Y. Chung, S. Mhin and H. Han, *Int. J. Hydrogen Energy*, 2024, **92**, 136–146.

206 C. Lee, K. Shin, Y. Park, Y. H. Yun, G. Doo, G. H. Jung, M. Kim, W.-C. Cho, C.-H. Kim, H. M. Lee, H. Y. Kim, S. Lee, G. Henkelman and H.-S. Cho, *Adv. Funct. Mater.*, 2023, **33**, 2301557.

207 Q. Wu, D. Ma, Y. Jia, J. Zhang, X. Feng, Y. Gao, J. Li, Y. Chen and J.-W. Shi, *Coord. Chem. Rev.*, 2026, **563**, 218036.

208 X. Ge, K. Xu, Z. Liu, X. Liang, J. Liang, Y. Li, X. Mu and J. Liu, *ACS Appl. Mater. Interfaces*, 2025, **17**, 58279–58287.

209 Y. Zhao, Y. Long, W. Liu, Z. Han, Y. Cui, Z. Li, W. Wang, Z. Duan and X. Fu, *J. Mater. Chem. A*, 2025, **13**, 8474–8483.

210 Q. Xu, L. Zhang, J. Zhang, J. Wang, Y. Hu, H. Jiang and C. Li, *EnergyChem*, 2022, **4**, 100087.

211 P. Shirvanian and F. van Berkel, *Electrochem. Commun.*, 2020, **114**, 106704.

212 U. Babic, M. Suermann, F. N. Büchi, L. Gubler and T. J. Schmidt, *J. Electrochem. Soc.*, 2017, **164**, F387.

213 S. A. Grigoriev, P. Millet, S. V. Korobtsev, V. I. Porembskiy, M. Pepic, C. Etievant, C. Puyenchet and V. N. Fateev, *Int. J. Hydrogen Energy*, 2009, **34**, 5986–5991.

214 B.-S. Lee, H.-Y. Park, I. Choi, M. K. Cho, H.-J. Kim, S. J. Yoo, D. Henkensmeier, J. Y. Kim, S. W. Nam, S. Park, K.-Y. Lee and J. H. Jang, *J. Power Sources*, 2016, **309**, 127–134.

215 R.-T. Liu, Z.-L. Xu, F.-M. Li, F.-Y. Chen, J.-Y. Yu, Y. Yan, Y. Chen and B. Y. Xia, *Chem. Soc. Rev.*, 2023, **52**, 5652–5683.
216 J. Knöppel, M. Möckl, D. Escalera-López, K. Stojanovski, M. Bierling, T. Böhm, S. Thiele, M. Rzepka and S. Cherevko, *Nat. Commun.*, 2021, **12**, 2231.
217 C. Kim, S. Seo, S. Yoon, J. Kim, Y. Park, P. Lee and D. You, *Renewable Energy*, 2026, **256**, 124194.
218 C. Zhao, S. Yuan, X. Cheng, L. An, J. Li, S. Shen, J. Yin, X. Yan and J. Zhang, *J. Power Sources*, 2023, **580**, 233413.
219 A. Weiß, A. Siebel, M. Bernt, T. H. Shen, V. Tileli and H. A. Gasteiger, *J. Electrochem. Soc.*, 2019, **166**, F487.
220 B. Liu, B. Ma, Y. Chen and C. Wang, *Corros. Sci.*, 2020, **170**, 108662.
221 C. L. Briant, Z. F. Wang and N. Chollocoop, *Corros. Sci.*, 2002, **44**, 1875–1888.
222 S. Hu, S. Ge, H. Liu, X. Kang, Q. Yu and B. Liu, *Adv. Funct. Mater.*, 2022, **32**, 2201726.
223 C. Wang, Z. Fei, Y. Wang, F. Ren and Y. Du, *Dalton Trans.*, 2024, **53**, 851–861.
224 X.-Y. Zhang, H. Yin, C.-C. Dang, H. Nie, Z.-X. Huang, S.-H. Zheng, M. Du, Z.-Y. Gu, J.-M. Cao and X.-L. Wu, *Angew. Chem., Int. Ed.*, 2025, **64**, e202425569.
225 B. Pang, S. Feng, Y. Xu, H. Chen, J. Li, Y. Yuan, X. Zou, X. Tian and Z. Kang, *Adv. Funct. Mater.*, 2024, **34**, 2411062.
226 W. Li, L. Zhang, L. Ma, J. Wang, R. Qi, Y. Pang, M. Xu, C. Zhao, C. Wang, M. Gao and X. Lu, *Nano Lett.*, 2025, **25**, 443–452.
227 J. Lim, M. Kim, S. S. Jeon, J. W. Lee, H.-E. Kim, G. Kim, Y. Kim and J. Kwon, *Energy*, 2025, **333**, 137439.
228 T. Huang, Z.-N. Bian, C. Wei, T. Huang, Y.-F. Wang, Z.-H. Liu, X.-Y. Du, Y.-M. Lv, Y.-Y. Fang, M. Fang and G.-M. Wang, *Rare Met.*, 2025, **44**, 1139–1146.
229 L. Hou, X. Gu, X. Cui, J. Tang, Z. Li, X. Liu and J. Cho, *EES Catal.*, 2023, **1**, 619–644.
230 Z. Lin, T. Wang and Q. Li, *Ind. Chem. Mater.*, 2023, **1**, 299–311.